Assessing Graphite Precipitation Mechanisms of the Albany Graphite Deposit

by

Sevgi Gökşen Suluova

A thesis submitted to the Faculty of Science and Environmental Studies

in partial fulfillment of requirements

For the degree of Master of Science

Department of Geology

Lakehead University

Thunder Bay, Ontario

April 2024

Abstract

Graphite is recognized as a 'critical raw material' due to its strategic importance for diverse industries (e.g., steel, automobile, clean technologies). The Albany graphite deposit, located west of Hearst in Thunder Bay, is a fluid-derived, igneous-hosted deposit. The morphology of the Albany deposit is unique because of fine-grained graphite occurring within two large breccia pipes. Albany graphite deposit is located in the south of the Nagagami Alkali Complex, north of the Gravel River fault. The objective of this study is to determine the mineralogy and alteration assemblages (non-weathering) using mineral compositions and textural associations and evaluate the alteration assemblages to determine whether they play any role in graphite precipitation.

In the Albany deposit, graphite typically occurs as elongated, lath-shaped, and plate-like crystals (<0.05 mm in width and ranges from 0.1 to 1.5 mm in length). Crystals are typically characterized as randomly oriented and showing both intergranular and intragranular textures. Graphite is mainly distributed along grain boundaries in clast components (intragranular), whereas it shows intergranular texture in the matrix. The abundance of graphite in the matrix (<15%) is higher than that in the clast (<10%). Three sub-groups of graphite, namely clast, matrix, and alteration assemblages were examined. The matrix assemblage is comprised of lithic fragments derived from the clasts. Clasts are mainly comprising varying proportions of graphite, plagioclase, potassium feldspar, quartz, biotite, amphibole, and chlorite, while the matrix is mainly comprised of equigranular graphite, plagioclase, potassium feldspar, quartz, and biotite. Hydrothermal alteration phases present biotite, sericite, calcite, and chlorite. Biotite and sericite are determined as pre-graphitization alterations due to their textural relationship with graphite. Calcite forms partial and rim replacement of plagioclase in the matrix, while chlorite replaces biotite and alters plagioclase along grain boundaries. Petrographic observations reveal that both calcite and chlorite alterations are directly associated with graphite in the Albany deposit. Calcite and chlorite, which constitute at the propylitic alteration assemblage, developed coevally with graphite.

The temperature of typical propylitic alteration is recorded up to 350°C. However, the temperature of graphite precipitation, considering the stability of the propylitic assemblage related to graphitization, is noted around 500°C (e.g. Borrowdale, UK). The graphite crystallization temperature of the Albany deposit is reported to be on the order of 550 to 600°C, which aligns with the graphitization temperatures mentioned in the literature, which are roughly 500 °C. Based on the temperature to precipitate graphite and propylitic alteration, and their textural relationships with each other, it is likely that graphitization may have occurred during propylitic alteration.

Graphite precipitation was probably triggered by hydration (chloritization) and carbonation (calcite precipitation) reactions. To precipitat**e** calcite, CO_2 will be removed from the fluid, resulting in the mole fraction of H_2O and the $CH_4:CO_2$ ratio being increased in the remaining fluid. Following this, the reduction of CO_2, through the reaction $CO_2 \rightarrow C + O_2$ could lead to the formation of graphite. The formation of chlorite formation involves the removal of the H_2O from the fluid phase. As a result, the residual fluid would become enriched in C, potentially leading to the precipitation of graphite. As dehydration of the fluid continues, the molecular percentage of CO_2 and CH_4 in the fluid will evolve to higher or lower values. Although the exact content of liquids is unknown, it can be evaluated by considering the fluid is rich in CO_2 and contains minor amount of CH_4, or vice versa. Chlorite may have developed from hydrothermal fluids, containing CO_2 and CH_4, following the possible reaction $CO_2 + CH_4 \rightarrow C + 2H_2O$, thus leading to the formation of graphite.

Acknowledgments

I would like to express my gratitude to my supervisor, Dr. Andrew Conly, for his guidance and support throughout my Master's degree. Many thanks to Dr. Guosheng Wu at the Lakehead University Instrumentation Laboratory for teaching the SEM-EDS system and helping me during my analyses. I would also like to thank the Ministry of National Education of the Republic of Turkey for financially supporting my studies. I express deep appreciation to my good friends Dilara Özyazıcı Topal and Farnia Dastoorian for their invaluable support throughout this process. Lastly, I want to thank my spouse and my family, who always supported me, despite the distance, through my journey.

Table of Contents

Abstract ii

Acknowledgments iv

List of Figures vii

List of Tables x

List of Appendices xi

List of Abbreviations xii

Chapter 1. INTRODUCTION 1

1.1 Objectives 1
1.2 Location and Access 2
1.3 Previous Work 3
1.4 Importance and Characteristics of Graphite 3
1.5 Classification of Natural Graphite 5
1.6 Characteristics of Fluid-Derived Graphite Deposits 8
  1.6.1 The Source of Carbon 10
1.7 Regional and Deposit Geology 11
  1.7.1 Regional Geology 11
  1.7.2 Geology of the Albany Graphite Deposit 16

Chapter 2. METHODS 18

2.1 Optical Microscopy 21
2.2 Secondary Electron Microscopy - Energy Dispersive X-ray Spectrometry 21

Chapter 3. RESULTS 22

3.1 Petrography 22
  3.1.1 Characteristic of Graphite in the Albany Deposit 22

3.1.2 Clast Petrography 26

3.1.3 Matrix Petrography 35

3.1.4 Carbonates.. 38

3.1.5 Alteration 41

3.2 Mineral Chemistry 47

3.2.1 Biotite... 47

3.2.2 Carbonates.. 54

3.2.3 Chlorite 58

Chapter 4. DISCUSSION... 63

4.1. Paragenesis.. 63

4.2. Precipitation Mechanism of the Albany Graphite Deposit 68

4.2.1. The C-O-H System 68

4.2.2. The Mobilization and Mechanisms of Precipitation of Graphite................ 70

4.3. The Role of Hydrothermal Alteration for Precipitation of Graphite at the Albany Deposit......... 74

Chapter 5. CONCLUSION AND FUTURE WORK 81

REFERENCES.. 87

APPENDICES 95

List of Figures

Figure 1.1 The location of the Albany graphite deposit. 3

Figure 1.2 Arrangement of carbon atoms in the (a) hexagonal and (b) rhombohedral graphite. 5

Figure 1.3 Traditional (commercial) classification of natural graphite. 6

Figure 1.4 Genetic classification of graphite. 8

Figure 1.5 Carbon isotope ranges of some selected fluid-derived graphite deposits. 11

Figure 1.6 Terrane boundary map of the Superior Province. 12

Figure 1.7 Regional geology interpreted from aeromagnetic data. 15

Figure 1.8 The location of the Albany graphite deposit. 16

Figure 1.9 3-D block model of the Albany graphite deposit. 17

Figure 2.1 Results of ground TDEM survey and locations of drill holes. 18

Figure 2.2 Lithologies of selected drill holes from the East pipe and the locations of selected samples for petrographic observations. 19

Figure 2.3 Lithologies of selected drill holes from the West pipe and the locations of selected samples for petrographic observations. 20

Figure 3.1 Images of drill core showing the two types of textures that graphite develops in. 23

Figure 3.2 Reflected light photomicrographs of intergranular texture of graphite from both pipes. 23

Figure 3.3 Reflected light photomicrographs of intragranular texture of graphite from both pipes. 24

Figure 3.4 Photomicrographs of the occurrence of graphite in the matrix and along the boundaries of silicate fragments. 25

Figure 3.5 Photomicrographs of both fragments and matrix components of the breccias. 27

Figure 3.6 Photomicrographs of components of the clast. 28

Figure 3.7 Photomicrographs and BSE images of igneous annite. 30

Figure 3.8 Photomicrographs and BSE images of metamorphic annite. 31

Figure 3.9 Photomicrographs and BSE images of igneous amphibole. 32

Figure 3.10 Representative photomicrographs of chlorite, sulphide, and accessory mineral in clasts. 34

Figure 3.11 Representative photomicrographs of matrix components. 36

Figure 3.12 Representative photomicrographs and BSE images of matrix components. 37

Figure 3.13 Photomicrographs of calcite veining. 39

Figure 3.14 Photomicrographs and BSE images of isolated calcite grains and dolomite veining. 40

Figure 3.15 Representative photomicrographs of annite alteration. 42

Figure 3.16 Photomicrographs and BSE images of key alteration assemblages. 43

Figure 3.17 Photomicrographs and BSE images of chlorite alteration after plagioclase. 44

Figure 3.18 Photomicrographs and BSE images of replacive chlorite after annite. 45

Figure 3.19 Photomicrographs and BSE images of replacive chlorite after annite. 46

Figure 3.20 The ASPE (Annite-Siderophyllite-Phlogopite-Eastonite) quadrilateral diagram showing the biotite composition from the Albany graphite deposit. 49

Figure 3.21 Albany Graphite deposit biotite compositions plotted in the 10*TiO_2-FeO-MgO ternary diagram. 50

Figure 3.22 Bivariate plots of Fe vs. Mg and Ti vs. Mg of biotite. 52

Figure 3.23 Ternary diagram (10*TiO_2-FeO-MgO) and photomicrographs show varying degrees of biotite-graphite contact. 53

Figure 3.24 Ternary diagram Ca – Mg – (Fe + Mn) with calcite and dolomite. 57

Figure 3.25 Bivariate plots of the calcite compositions from the Albany graphite deposit; Fe + Mn + Mg versus Ca. 57

Figure 3.26 Bivariate plot illustrates the inverse relationship between the Ca content and the Fe+Mn content in calcite. 58

Figure 3.27 Maximum, minimum, and average oxide content of all chlorites and different occurrences of chlorite in the Albany graphite deposit. 60

Figure 3.28 Ternary diagram (Al – Fe – Mg) indicating the compositions of chlorite photomicrographs show varying degrees of chlorite-graphite contact. 62

Figure 4.1 Paragenetic sequence of the Albany graphite deposit, divided into the stages: pre-mineralization, mineralization, and post-mineralization. 64

Figure 4.2 HR-TEM-EDS elemental map showing the nano-scale chlorite within graphite. 66

Figure 4.3 C–O–H fluid system showing graphite stability field. 69

Figure 4.4 Ternary C-O-H diagram showing the effect of temperature and pressure variations on graphite precipitation. 71

Figure 4.5 The C-O-H ternary diagram shows the effect of fluid mixing on graphite precipitation. 73

Figure 4.6 Representative image of chloritization of biotite. 75

Figure 4.7 C–O–H fluid system displays the CO_2 reduction. 78

Figure 4.8 The C–O–H diagram illustrates the molecular percent of the fluid composition. 79

List of Tables

Table 1.1 Selected occurrences of fluid-deposited graphite. 9

Table 3.1 Clast mineral compositions. 35

Table 3.2 Matrix mineral compositions. 37

Table 3.3 Representative compositions of biotite from the Albany graphite deposit. 48

Table 3.4. Representative composition of calcite from the Albany graphite deposit. 55

Table 3.5 Representative composition of dolomite from the Albany graphite deposit. 56

Table 3.6 Representative compositions of chlorite from the Albany graphite deposit. 61

Table 5.1 Characteristic of four stages: host rock, pre-graphitization alterations, graphitization, and late to post-graphitization alterations. 83

List of Appendices

1. **Feldspars** 92
2. **Carbonates** 109
3. **Biotite** 117
4. **Chlorite** 132
5. **Amphiboles** 135
6. **Pyroxenes** 140
7. **Fe-Ti Oxides** 143
8. **Accessory Minerals** 146

List of Abbreviations

The abbreviation of minerals is after Whitney & Evans (2010).

Symbol	**Minerals**
Act	Actinolite
Ab	Albite
Amp	Amphibole
Ann	Annite
Ap	Apatite
Bt	Biotite
Cal	Calcite
Ccp	Chalcopyrite
Chm	Chamosite
Chl	Chlorite
Chr	Chromite
Dol	Dolomite
Ed	Edenite
Gr	Graphite
Ilm	Ilmenite
Kfs	K-Feldspar
Mag	Magnetite
Or	Orthoclase
Phl	Phlogopite
Pl	Plagioclase
Px	Pyroxene
Py	Pyrite
Qz	Quartz
Sp	Sphalerite
Ttn	Titanite

Symbol	**Others**
a.p.f.u.	Atomic per formula unit
BSE	Back-Scattered Electron
xpl	Cross-polarized light
EDS	Energy Dispersive Spectroscopy
FMQ	Fayalite–magnetite–quartz buffer
HR-TEM	High-Resolution Transmission Electron Microscopy
NRAC	Nagagami River Alkali Complex
fO_2	Oxygen fugacity
ppl	Plane-polarized light
SEM	Scanning Electron Microscope

Chapter 1. INTRODUCTION

1.1 Objectives

Albany Graphite Corp (a subsidiary of Zentek Ltd., formerly Zenyatta Ventures Ltd.) discovered the Albany graphite deposit in late 2010 in response to drilling geophysical anomalies identified during a regional exploration program for magmatic Ni-Cu sulphide deposits. Conly and Moore (2015) provide the first documented description and petrogenetic model for the Albany graphite deposit. Albany is noticeably different in terms of deposit morphology from other fluid-derived, igneous-hosted deposits (e.g., Borrowdale, UK; Ortega et. al., 2010). The primary distinction is in the occurrence of crystalline, fine-grained graphite hosted within two large breccia pipes.

Conly and Moore (2015) interpreted Albany to be a fluid-derived, igneous-hosted deposit. Owing to the occurrence of two breccia pipes situated along the margin of a large alkalic igneous complex. Conly and Moore (2015) provide various evidence that supports the formation of the Albany graphite deposit having been fluid-derived, based on:

- The high purity of the graphite, which indicates precipitation from a carbonaceous bearing aqueous (H_2O-CO_2-CH_4) fluid with a high concentration of dissolved carbon;
- Considering it as an epigenetic deposit formed through fluid-rock interaction;
- The presence of breccia pipes that provided a pathway for the carbon-bearing fluids to flow, leading to widespread graphite deposition; and,
- Evidence of hydrous and related alteration assemblages (sericitization, pyrite-pyrrhotite, and, less commonly, phlogopite, hematite, and supergene alterations) were observed.

There are several manners by which graphite can be precipitated from a carbonaceous fluid including (1) reducing temperature or increasing pressure, (2) mixing of fluids with different CO_2/CH_4 ratios, (3) hydration reactions between the fluid and anhydrous minerals in the host rock and (4) fluid reduction (Barrenechea et al., 1997; Luque et al., 1998; Ortega et al., 2010; Rumble, 2014; Rosing-Schow et al., 2017; Touret et al., 2019). Hydrous alteration has been suggested to be a key mechanism in graphite precipitation (e.g. Barrenechea et al., 1997; Duke & Rumble, 1986; Huizenga, 2011; Ortega et al., 2010; Pasteris & Chou, 1998; Rosing-Schow et al., 2017), as hydrothermal fluids can dissolve carbon and transport it as CO_2 and CH_4 (Luque et al., 1998). Conly and Moore (2015) observed various forms of hydrous alteration, but its role in graphite precipitation at Albany has not been fully evaluated. Changes in pressure and temperature conditions are effective mechanisms that lead to graphite precipitation (Luque et al., 1998b; Ortega et al., 2010; Simandl et al.) but these neither are considered as being critical at the Albany deposit. In general, an increase in pressure normally favors graphite precipitation but as the Albany deposit is a vent breccia/diapir-hosted system that extends to the paleosurface. It would have been subject to a sudden depressurization. *In-situ* Raman graphite geothermometry has yielded inconsistent results (A. Conly, personal communication, 2022), therefore the role of temperature has not been fully evaluated. This study will not evaluate the effects of temperature.

Rather, the general objective of this study is to conduct a detailed mineralogical investigation into the nature of non-weathering-related alteration and its relationship to the graphite formation at the Albany deposit. Optical microscopy is used to assess the mineralogical, textural, and alteration characteristics of the Albany deposit. However, scanning electron microscopy-energy dispersive spectroscopy (SEM-EDS) was also used, to provide a comprehensive and detailed analysis of the alteration minerals, as these are fine-grained and/or form as finely intergrown assemblages. Through the integration of optical mineralogy and SEM-EDS analysis, the various alteration assemblages will be characterized and assessed paragenetically to see if any play a role in graphite precipitation.

1.2 Location and Access

The Albany graphite deposit is located about 70 km to the west of Hearst and about 400 km to the northeast of Thunder Bay, Ontario (Fig. 1.1). The Albany graphite deposit, 100% owned by Zentek (previously known as Zenyatta Ventures Ltd.), is situated at the coordinate system UTM Zone 16 NAD 83 coordinates 681,700 m E, 5,544,750 m N (RPA Inc., 2014, 2015). There is no direct road access to the property; off-road vehicles (ATVs) and helicopters are the only means to currently access the property.

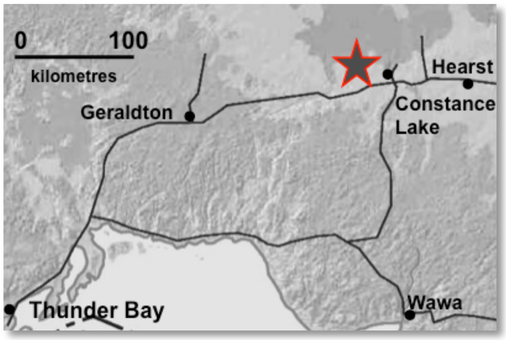

Figure 1.1 The location of the Albany graphite deposit within northern Ontario (deposit is marked with a red star)

1.3 Previous Work

There are few on the Albany graphite deposit. Since there is no outcrop exposure due to extensive covering by Paleozoic carbonate rocks and glacial sediments, the studies regarding this area are limited. Previous exploration work has been focused on the Nagagami River, Hudson Bay and James Bay Lowlands area. Between 1959 and 2008, eight different exploration companies explored the region and focused on geophysical surveys (Airborne magmatic and Electromagnetic (EM)) and diamond drill projects (RPA Inc., 2014, 2015). Based on airborne magnetic maps from the Ontario Geological Survey (OGS) and geological interpretation (Stott, 2008), Zentek conducted an exploration program targeting nickel (Ni), copper (Cu), and platinum group metals (PGMs) in 2010. It was through the latter that deposits of graphite in two large breccia pipes were discovered. A total of 63 holes were drilled throughout the Albany graphite deposit in 2014 (RPA Inc., 2014, 2015). Conly and Moore (2015) investigated the geology, ore characteristics, and origin of the Albany graphite deposit, representing the first and only published paper on the Albany deposit. To constrain the genesis of the deposit, they unified field, mineralogical, and isotopic data concluding that the Albany was an epigenetic, igneous-hosted, fluid-derived graphite deposit.

1.4 Importance and Characteristics of Graphite

Canada is one of the world's largest graphite producers (Brown et al., 2019), and graphite is considered as a 'critical raw material' by the Canadian Critical Minerals Strategy, (2022). The European Commission and the US Geological Survey have also added graphite to their critical mineral list in the past few years. Critical minerals are essential to strategic industries such as agriculture, manufacturing, artificial intelligence, clean technologies, electric vehicles, energy, and much more.

Graphite is a significant industrial mineral due to its properties of both metals and nonmetals. While the metallic properties include electrical and thermal conductivity, the non-metallic properties include high thermal resistance, chemical inertness, and lubricity (Luque et al., 2013).

The advantage of graphite compared to other minerals is its physical and thermal features, allowing it to be used in various applications. Graphite is primarily used in refractory applications such as lubricants, steelmaking, brake linings and foundry facings, and the synthesis of other carbon allotropes. Other industrial uses include zinc-carbon, zinc-chloride, alkaline batteries, electric motor brushes, and pencil leads (Olson, 2011). Based on the United States Geological Survey (2012), developments in thermal technology will lead to the development of new applications for graphite in high-tech areas. The new applications include lithium-ion batteries, the usage areas of which are increasing day by day, nuclear, wind and solar power, fuel cells, and semiconductors or graphene (Crossley, 2000; Balan et al., 2010; Luque et al., 2013).

Graphite is opaque, gray-black, and soft (1-2 on the Mohs hardness scale). One of graphite's well-known physical features is its simple carbon composition and simple layered structure. The structure of graphite crystals is their size on both the microscopic and macroscopic levels (Luque et al., 1998). Graphite consists of a 6-layered ring of covalently bonded carbon atoms perfectly repeating and extending infinitely in the basal plane. This single layer comprises graphene (Yaya et al., 2012). Differences in the stacking arrangement of the graphene sheets generate the two polytypes of graphite hexagonal (a-graphite), which is the most natural formation of graphite, and rhombohedral graphite (b-graphite; Fig. 1.1). Rhombohedral graphite can be generated by mechanical (e.g. grinding), chemical or thermal treatment of natural graphite (Qing et al., 2017). While hexagonal graphite is thermodynamically stable and characterized by an ABAB stacking sequence of the graphene layers, rhombohedral graphite is metastable and shows ABCABC stacking. In all known natural cases, the hexagonal phase is strongly dominant over the rhombohedral phase (Luque et al., 1998). Previous studies show that, as a variant of hexagonal graphite, turbostratic graphite is formed due to various changes, involving the rotation, translation, curvature, and variation of interlayer spacing of graphene layers in the graphite structure which arise through mechanical modifications (Li et al., 2007).

The structure of crystalline is most commonly characterized by the interplane distance, the dimensions of the structural components La (measured along the a-axis) and Lc (measured along the a-axis), and the degree of order (Popova, 2017). The interplanar d (002) spacing defines the distance between successive, parallel planes of atoms. Fully ordered graphite has a (002) spacing of ~3.35 Å (Landis, 1971) and is on the order of at least several hundred to a thousand Angstroms each for La and Lc (a = 0.246 nm and c = 0.6708 nm) (Luque et al., 1998). Solid carbon phases with d (002) >3.35 Å and smaller crystallite sizes are referred to as "disordered graphite." The size of the ordered graphite domains is referred to as the crystallite size (Luque et al., 1998). X-ray diffraction (XRD) is the standard method for investigating the structure of bulk graphite and enables the determination of the structure's degree of order and the size of the crystallites (Popova, 2017).

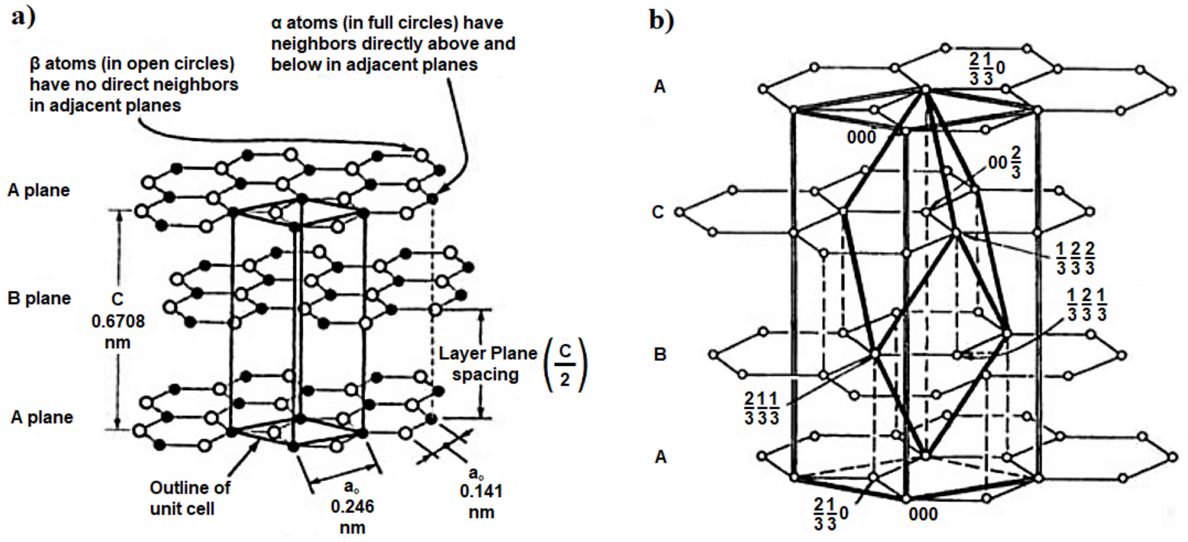

Figure 1.2 Arrangement of carbon atoms in the (a) hexagonal and (b) rhombohedral graphite (Yaya et al., 2012).

1.5 Classification of Natural Graphite

Graphite deposits are classified into two categories: traditional (commercial; Fig 1.2) and genetic (Fig. 1.3). For the traditional classification, graphite deposits are divided into three groups according to grain size with certain inferences to the degree of and graphite morphology being made (Spence, 1920; Mitchell, 1993; Luque et al., 2013). Also inferred from this classification is the economic valuation of the graphite, with a general increase in the refined product going from amorphous to flake, and to vein (lump and chip) graphite. Based on the crystallinity of graphite is grouped as crypto to microcrystalline (amorphous) and crystalline (flake and lump or chip). The grain size ranges of microcrystalline, flake, and lump-chip graphite are <4 µm, 40 µm to 4 cm and powders to 10 cm pieces (Simandl et al., 2015). It is generally thought that microcrystalline and flake graphite deposits arise from the metamorphism of carbonaceous sedimentary rocks, with lump-chip graphite being epigenetic, it precipitating from fluids often associated with high-grade metamorphic rocks (Robinson et al., 2017). However, deposits such as Albany do provide evidence for fluid-deposited microcrystalline graphite (Conly & Moore, 2015).

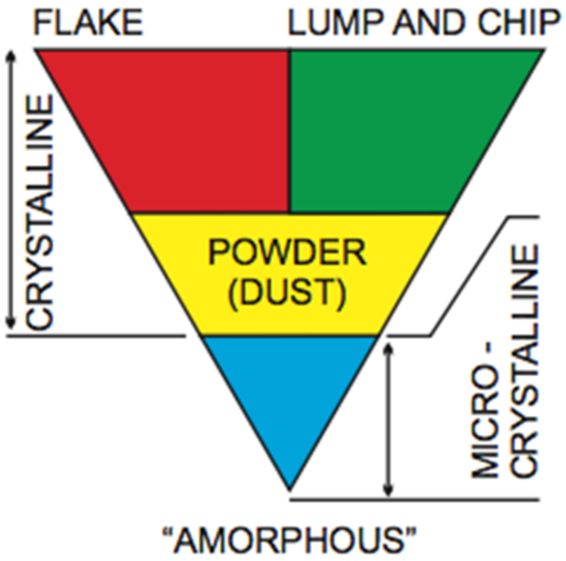

Figure 1.3 Traditional (commercial) classification of natural graphite (Simandl et al., 2015).

While this is no single, universally accepted genetic (geological) classification of graphite deposits, many researchers invoke some form of a two-tier classification: fluid-derived and meta-sedimentary (Beyssac et al., 2014; Luque et al., 2012; Rumble & Hoering, 1986; Taner et al., 2017) (Fig 1.3). Natural graphite may form from the *in-situ* transformation of sedimentary organic matter during metamorphism or by precipitation from carbon-bearing fluids. Some graphite deposits are formed through a combination of both (Parnell et al., 2021; Taner et al., 2017).

Both types of graphite exhibit distinct characteristics. First, in fluid-derived deposits, there are generally relatively extensive degrees of mobilization of carbon from the source in comparison to *in-situ* metamorphic processes (Drever et al., 2023). Second, metamorphic graphite typically occurs as courser (flakey) crystals, whereas the precipitation of carbon-bearing fluids forms vein (also known as lump) graphite, resulting in a wider array of crystal habits (e.g., flaky, spherulitic, colloform, cryptocrystalline, rings, cones, tubes, e.g., Barrenechea, 2009). Although metamorphic graphite typically has a wider range of crystallinity, fluid-derived graphite deposits typically yield higher purities and higher degrees of crystallinity (Luque et al., 1998, 2012). Fluid-derived deposits can be described as syn-metamorphic to epigenetic, whereas the meta-sedimentary deposits are syngenetic to syn-metamorphic (Luque et al., 2012a, 2012b; Taner et al., 2017). Fluid-derived deposits can be further classified into granulite-hosted and igneous-hosted, while meta-sedimentary deposits can be subdivided into carbonated-hosted and siliciclastic-hosted.

The term "granulite-hosted deposit" mostly originated based on the examination of the Sri Lanka deposits, which consist of high-grade veins within granulite rocks. These have been extensively studied by Luque and others (Luque et al., 2012; 2014; Simandl et al., 2015; Touret et al., 2019). Carbonate-hosted deposits can be challenging to classify since they can have carbon sourced from both sedimentary organic matter and through the devolatilization of carbonate. Carbonate-host deposits that have undergone devolatilization have generated a metasomatic CO_2-rich fluid, which, if it is reduced, can generate graphite. Conly (personal communication, 2021) suggested linking the granulite-hosted and carbonated-hosted graphite deposit within the "metasomatic subtype". Because certain carbonate-hosted deposits that, because of metamorphism, have undergone significant devolatilization (which is the case in calc-silicate metamorphic systems and in some marbles) with granulite-hosted.

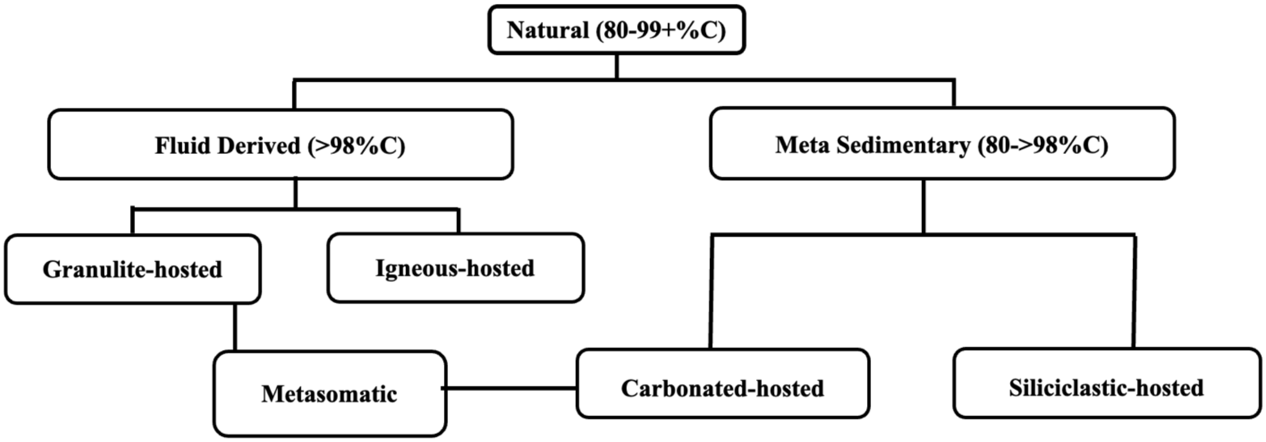

Figure 1.4 Genetic classification of graphite (Conly, in prep)

1.6 Characteristics of Fluid-Derived Graphite Deposits

Occurrences of fluid-derived graphite can be characterized according to parameters such as the volume of the deposit, host rock lithology, structural relation between the graphite and its host, graphite: host volumetric ratio (e.g., massive or disseminated graphite), morphology of the graphite (e.g., isolated blades, spherulites, massive fine-grained), crystallite size and graphite purity (wt% C) (Luque et al., 1998). Graphite deposition from fluids can occur due to interactions between the fluid and the surrounding rock, resulting in two distinct modes: massive replacement and dissemination (Luque et al., 1998). Table 1 provides some well-known geologic occurrences of fluid-deposited graphite.

Massive replacement often involves the replacement of silicate minerals. The well-known Borrowdale deposit in the United Kingdom was produced through the replacement and dissemination in the volcanic host rocks. Here the morphology of graphite ranges from flakes to spherulites and cryptocrystalline aggregates (Luque et al., 2009). Textural observations show that chlorite replaces ferromagnesian minerals, and sericite at least partially replaces original plagioclase (Barrenechea et al., 2009; Ortega et al., 2009, 2010a). Graphite disseminations can also form through the hydrous alteration of primary minerals in igneous rocks. As an example, within troctolites of the Duluth Complex of Minnesota, graphite spherulites, reaching sizes of a few millimeters in diameter, are intergrown with fine-grained amphibole and chlorite mats, the latter having replaced mafic silicate phases (Hollister, 1980; Pasteris, 1989; Pasteris et al., 1995).

Table1.1 Selected occurrences of fluid-deposited graphite

Location	Host Rock	Age	Type of Occurrence	Mineral Association	Graphite Morphologies	Inferred Origin of Carbon	References
Sri Lanka	Granulite and amphibole facies metasediment	Precambrian	Fluid-derived (granulite-hosted)	Q+Plg+Kfs+Grt+Hbl +Bio+Cal+Dol ±Opx±Cpx	Vein and flake	CO_2 infiltration of deep crustal carbon	Luque et al., 2012, 2013; Touret et al., 2019
Borrowdale (UK)	Volcanic rocks-andesites	Ordovician	Fluid-derived (igneous-hosted)	Q+Plg+Py+Chl+ Cpx+Opx±Kfs	Flake, cryptocrystalline, spherulitic aggregates, and dish-like forms.	Assimilation of organic matter (biogenic)	Barrenechea et al., 2009; Ortega et al., 2010
Bissett Creek (Grenville, Canada)	Granitic gneisses	Mesoproterozoic	Fluid-derived Hybrid (Metamorphic siliciclastic and calc-silicate)	Q+Plg+Kfs+Bio+Grt ±Py±Po	Flake and disseminated	Assimilation of organic matter (biogenic)	Taner et al., 2017; Drever et. al., 2022
Montpellier (Grenville, Canada)	Metavolcanic rocks, metasedimentary schists	Mesoproterozoic	Fluid-derived Metamorphic (calc-silicate)	Plg+Kfs+Bio+Grt +Cal+Dol±Py±Po	Flake	Assimilation of organic matter (biogenic)	Taner et al., 2017
Huelma, Betic Cordillera (Spain)	Alkali basalts	Jurassic	Vein	Aug+Ol+Plg+Kfs ±Chl±Fe-Ti Ox	Flake and nodular	Devolatilization of organic matter	Barrenechea et al., 1998
Duluth Complex, Minnesota (USA)	Serpentinized ultramafic within troctolites	Precambrian	Fluid-derived (igneous-hosted) Disseminated	± Cu – Fe sulfides	Flake	Assimilation of organic matter (biogenic)	Hollister, 1980; Pasteris, 1989; Luque et al., 1998

Abbreviations; Q = Quartz, Plg = Plagioclase feldspar, Kfs = K-feldspar, Grt = garnet, Opx = Orthopyroxene, Cpx = Clinopyroxene, Hbl = hornblende, Bio = Biotite, Cal = Calcite, Dol = Dolomite, Py = Pyrite, Chl = Chlorite, Po = Pyrrhotite, Aug = Augite, Ol = Olivine, Ox = Oxide.

1.6.1 The Source of Carbon

To thoroughly understand the formation of fluid-deposited graphite, it is imperative to investigate both the origin of the carbon and the mechanisms of mobilization and precipitation (Barrenechea et al., 1997). Graphite can precipitate from a CO_2-CH_4-H_2O fluid. Potential sources of carbon include: 1) C-bearing compounds released during maturation of organic matter: (2) C-bearing compounds released during devolatilization of carbonate-rich materials; and (3) igneous (mainly mantle-derived) carbon (Fig 1.4) (Luque, 1998; Ortega, 2010; Simandl, 2015). The possible carbon sources (organic matter, mantle-derived magmatic carbon, and carbonates) are characterized by different isotope ranges (Luque, 2012). Thus, the most reliable information on the origin of carbon in C–O–H fluids is provided by the carbon isotope ratio ($^{13}C/^{12}C$) of the graphite (Barrenechea, 1997; Ortega, 2010). Fluid-derived graphite deposits vary in carbon isotope ranges and sources of carbon (Fig1.4).

During the assimilation of organic matter, carbon-bearing gases may be released. These contain reduced carbon that is biogenically produced, so are enriched in ^{12}C, with ^{13}C. For organic matter (biogenic), $\delta^{13}C$ values range from about -40‰ to -15‰, with an average of -25‰ (Weis et al., 1981; Barrenechea, 1997; Luque, 2012, 2014). For comparison, the isotopic composition of diamonds and mid-oceanic ridge basalts (MORB) indicates that the $\delta^{13}C$ values of mantle-derived carbon range between -9.8‰ and -4.8‰ (Pearson et al., 1990; Barrenechea, 1997). The devolatilization of carbonate minerals may produce carbon, and this type of oxidized carbon is enriched in ^{13}C. When incorporated into a liquid, this oxidized carbon should lead to the formation of graphite isotopically heavier than the biogenically derived carbon. The $\delta^{13}C$ values of marine carbonates are between -5‰ to +5‰ (Hahn-Weinheimer and Hirner, 1981; Weis et al., 1981; Barrenechea, 1997; Luque, 2012, 2013). Conly and Moore (2015) postulate that graphite precipitated from an ortho-magmatic carbon-rich (CO_2-CH_4-H_2O ± H_2S) fluid and, through possible Fischer-trophy synthesis, produced a CO_2-CH_4 fluid from which graphite precipitated. The stable carbon isotope compositions of the Albany graphite, with values of $\delta\ ^{13}C$ -16.9‰ and -16.8‰, are thus consistent with the theory that the carbon is derived from a mantle source (Conly & Moore, 2015).

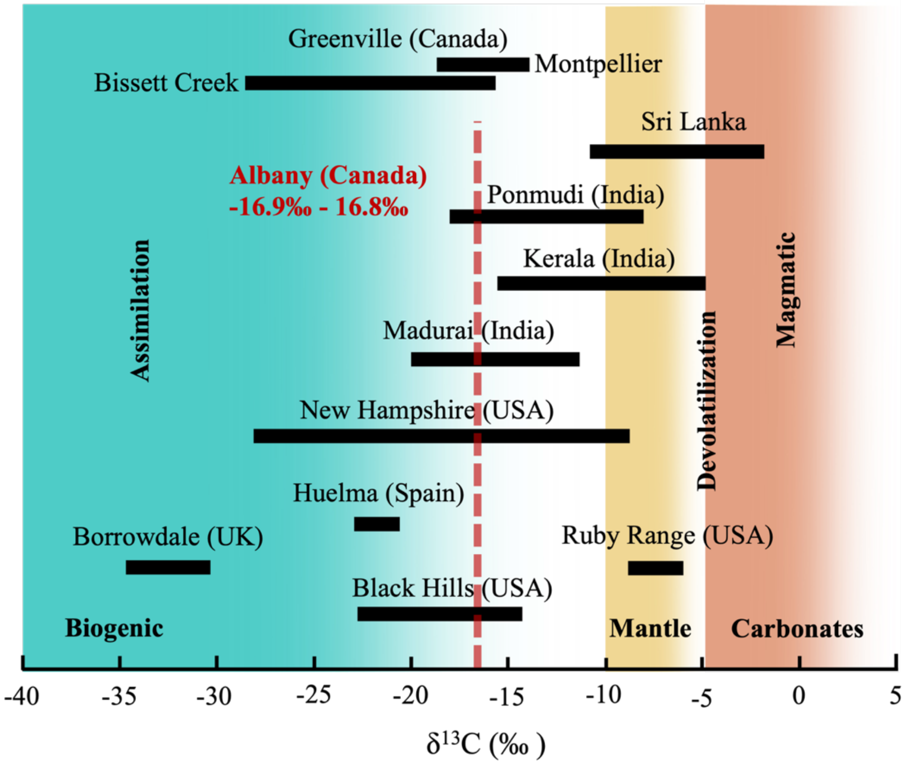

Figure 1.5 Carbon isotope ranges of some selected fluid-derived graphite deposits from various locations. The colours represent the ranges of $\delta^{13}C$ for different carbon sources: green (biogenic carbon, organic matter), yellow (mantle-derived carbon), and orange (carbonated carbon). (Modified from Luque et al., 2012) (Albany from Conly & Moore, 2015 ; Greenville from Taner et al., 2017).

1.7 Regional and Deposit Geology

1.7.1 Regional Geology

The Superior Province, covering an area of 1.4 x 10^6 km^2, is the largest Archean craton on Earth (Percival & Stott, 2012). It is surrounded by provinces of Paleoproterozoic age on the west, north, and east, and Mesoproterozoic age (Grenville Province) on the southeast (Percival, 2007). The Archean craton (3.0 to 2.7 Ga) is considered to have developed the accretion of east-west trending belts during the Kenoran Orogeny whose effects extend to the far north (Percival, 2004). The Superior Province consists of a series of east-trending belts that were metamorphosed to greenschist-granulite facies, and now consist of granite-greenstone, metasedimentary, plutonic and high-grade gneisses (Card & Ciesielski, 1986). The belts are divided across multiple subprovinces or terranes according to their lithological, metamorphic, geochemical, isotopic, geochronological, and geophysical properties. The regional geology from aeromagnetic data was interpreted and mapped by Stott (2008). The Albany graphite deposit is located south of the Nagagami Alkali Complex and north of the Gravel River fault, the latter representing the boundary between the Quetico and Eastern Marmion Terrane in the Superior Province (Fig 1.9; Conly & Moore, 2015).

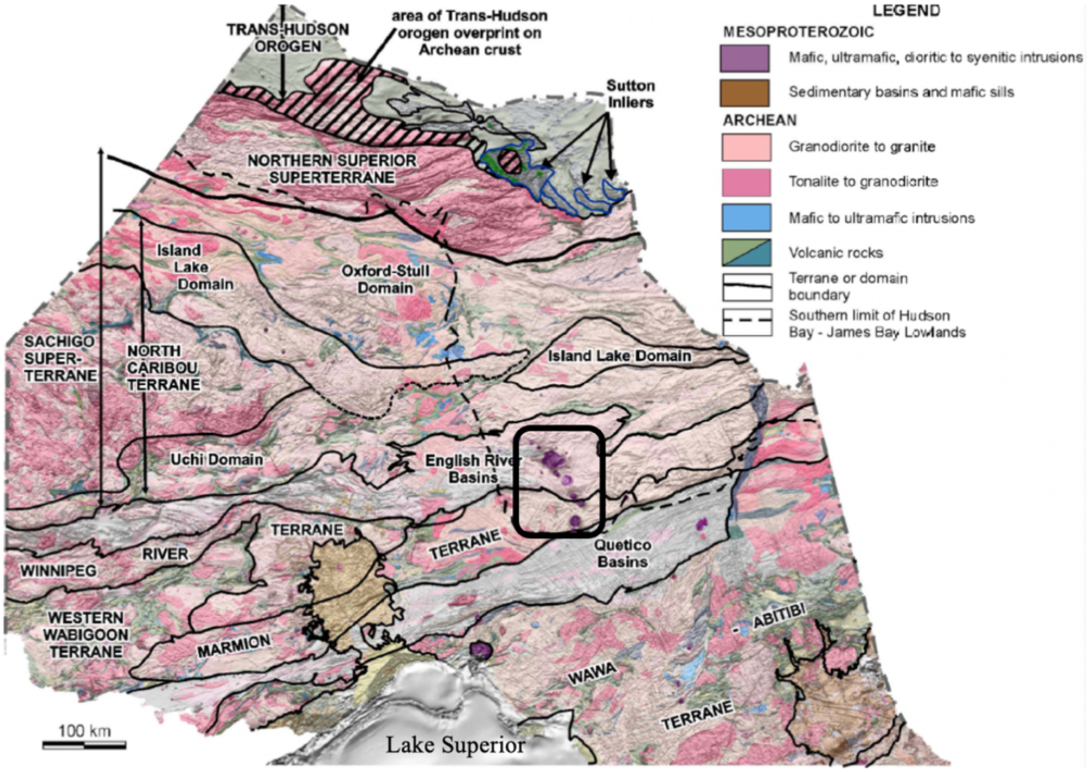

Figure 1.6 Terrane boundary map of the Superior Province (from Stott, 2011). The black marked area corresponds to Fig. 1.10.

1.7.1.1 The Quetico Subprovince

The Quetico Subprovince is located south of the Marmion Terrane and north of the Wawa Terrane in Ontario. It is a 10 km to 100 km wide by 1,200 km long belt consisting dominantly of greywacke, derived migmatite, and granite. Although no stratigraphic sequence has been determined within the poly-deformed and variably metamorphosed sedimentary succession, it is observed that the younging directions are predominantly towards the north (Percival & Williams, 1989).

According to Davis and Jackson (1988), the metasedimentary rocks were deposited before 2696 Ma. Depositional age constraints indicate slightly older ages for the northern Quetico [2.698-2.696 Ga, (Davis et al., 1990)] than for the south [<2.692 Ga, (Zaleski et al., 1999)]. The deformation events were followed by low-pressure, high-temperature, metamorphism, which tends to be east-northeast, reaching upper-amphibolite and local granulite facies at ca. 2.67 to 2.65 Ga (Pan et al., 1994, 1998) in the central region and greenschist facies at the margins (Percival & Williams, 1989).

1.7.1.2 Marmion Terrane

Located north of the Quetico basin, the Marmion terrane consists predominantly of metamorphosed felsic intrusive rocks (3.0 to 2.7 Ga) (Davis et al., 1990). After the tonalite basement formed at 3010-2999 Ma (Davis & Jackson 1988), greenstone belts formed between 2990 and 2715 Ma (Percival & Stott, 2012; Stone et al. 2002).

The period of continental arc magmatism in the Winnipeg River region (2.72-2.70 Ga) is attributed to the north- and eastward subduction of oceanic rocks (Percival, 2007). Then, the Marmion continent was affected by at least two Neoarchean deformation events, which are eastward-extending D1 structures (<2706 Ma) and eastward-trending dextral D2 shear zones (>2694 Ma) (Percival & Stott, 2012). Late strike-slip and dip-slip motion faults define the present terrane boundary (Gower & Clifford, 1981).

1.7.1.3 Nagagami Alkalic Rock Complex

The Nagagami River alkali complex (NRAC) is the southernmost portion of an arcuate collection of alkalic intrusive complexes that extend north to northwest from the Marmion terrain into the English River basin. The Gravel River fault separates the Marmion terrane and NRAC from the Quetico sub-province to the south. Aeromagnetic data observations illustrate that the Nagagami River Alkalic Rock Complex consists of two ring-shaped subcomplexes (Fig. 1.10) The fact that the aeromagnetic model of the southern subcomplex cuts that of the northern subcomplex indicates that the southern subcomplex is younger (Sage, 1988). The north subcomplex consists mainly of magnetite-bearing, amphibole-pyroxene syenite, and the south subcomplex, in addition to amphibole-pyroxene syenite, contains a nepheline syenite phase (Sage, 1988).

The Nagagami River Alkali complex truncates north to northwesterly trending Paleoproterozoic Matachewan (Hearst) dike swarms (ca. 2454 Ma; Heaman, 1988; Phinney & Morrison, 1988) and the east to northeasterly Kapuskasing dike swarm (ca. 2124-2170 Ma; Conly & Moore, 2015; Stott, 2008). Jagodits and Paterson (1964) have interpreted the trends of Matachewan and Kapuskasing dike swarms as being due to diabase dikes. Because of the relationship between these dike swarms and NRAC, the age of the Nagagami River Alkalic Rock Complex is considered to be late Precambrian.

1.7.1.4 Phanerozoic Rocks and Sediments

The Albany deposit has no outcrop exposure. It and the hosting Precambrian rocks of the Marmion terrane in the region are unconformably covered by Paleozoic (460-360 Ma) carbonate rocks of the Moose River basin, along with glacial sediments, and muskeg. The thickness range of the glacial overburden ranges from 28 to 55 m, while the Paleozoic cover is <16 mm thick (Conly & Moore, 2015; Johnson et al. 1991; Legault et al. 2015).

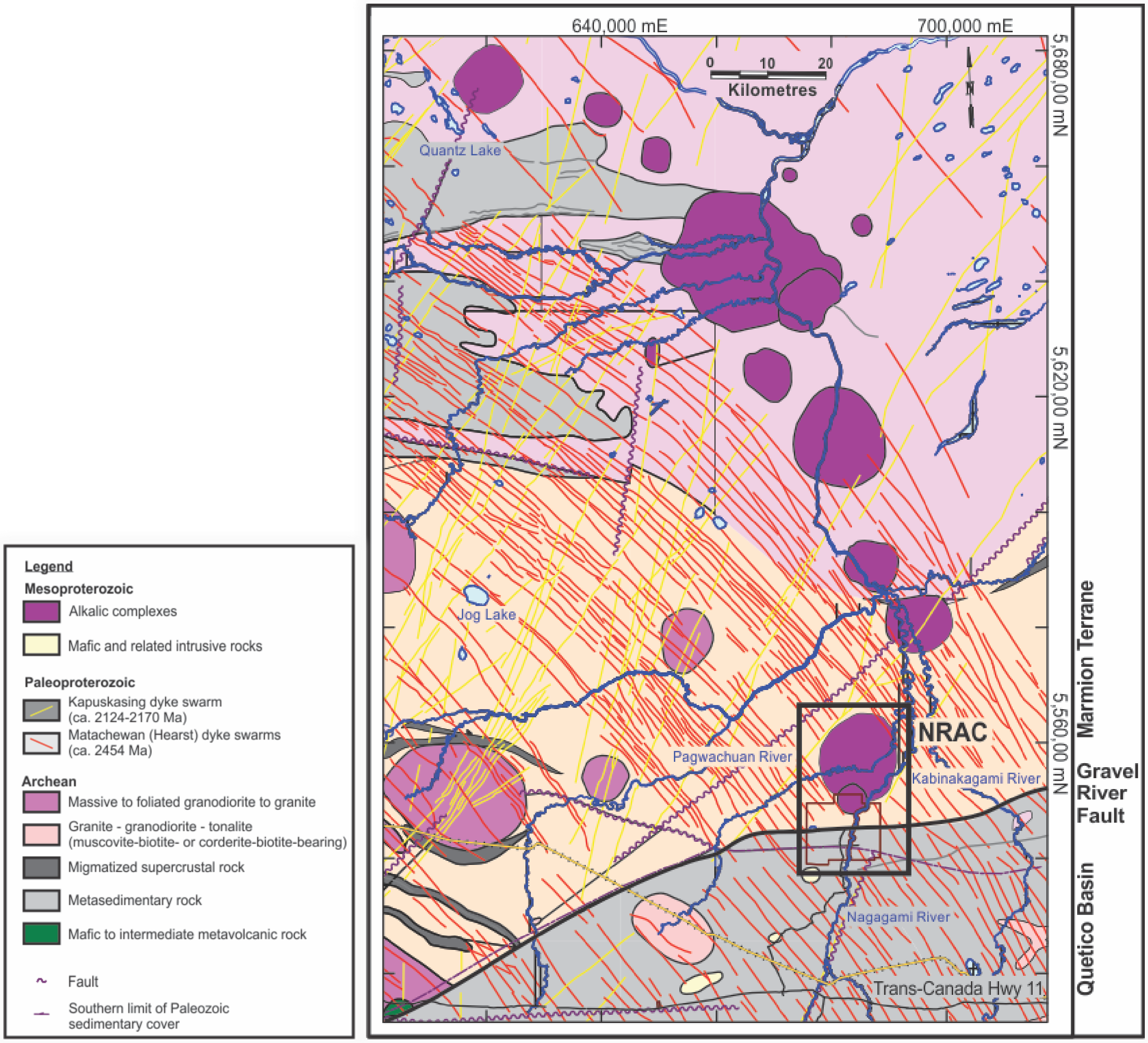

Figure 1.7 Regional geology interpreted from aeromagnetic data. Subcomplexes of the Nagagami River Alkalic Rock Complex are shown in the marked area (UTM zone Z16, NAD 83; from Conly & Moore, 2015 after modification from Stott, 2008).

1.7.2 Geology of the Albany Graphite Deposit

The Albany deposit is situated north of the Gravel River Fault boundary between the Quetico Basin and the Marmion terrain (Fig 1.10). Based on earlier interpretations of geophysical data by Conly and Moore (2015) and Zenyatta, the Albany Alkalic Complex was thought to exist. But reassessment of geophysical data by Conly (personal communication, 2022) now favours the Albany deposit being situated along the southern margin of the smaller, southern intrusive body of the Nagagami River Alkalic Rock Complex (NRAC).

The host rock of the Albany graphite deposit is quite varied, including predominantly quartz monzonite, quartz syenite, diorite, and nepheline syenite (Conly & Moore, 2015). The defining characteristic of the Albany deposit is the occurrence of fine-grained graphite within two large breccia pipes (Figs 1.8 and 1.9). The West and East pipes are comprised of angular to semi-rounded fragments that vary in size from a millimetre to several meters. Lithologically, the clasts consist of monzonitic and syentitic host rocks, along with a subordinate occurrence of amphibole biotite schist, granite, and gneiss. These later lithological compositions are similar to rocks in the Marmion terrane and Quetico subprovince (Conly & Moore, 2015).

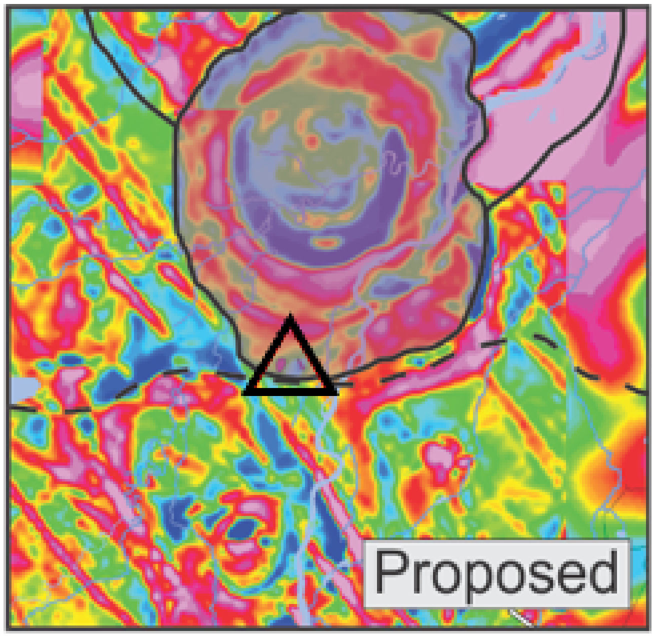

Figure 1.8 The location of the Albany graphite deposit (East and West pipes) the outline of the two breccia pipes is marked and are contained within the region delineated by the black triangle.

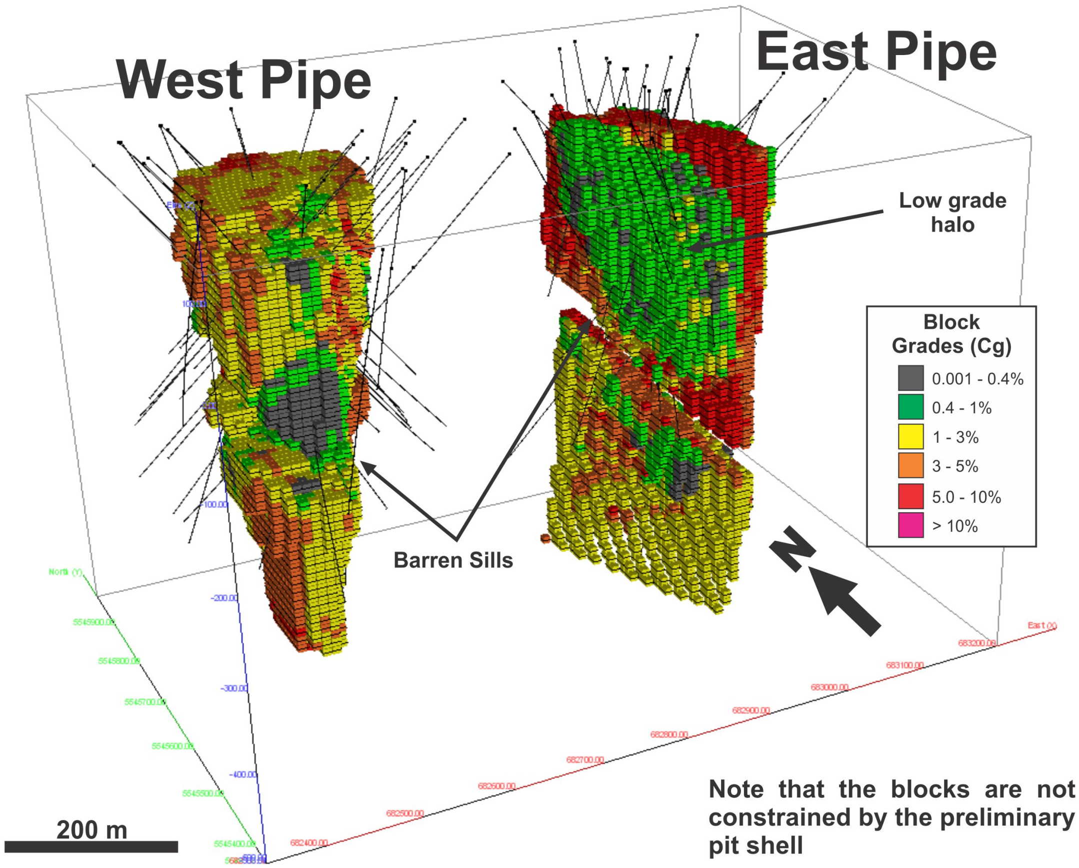

Note that the blocks are not constrained by the preliminary pit shell

Figure 1.9 A 3-D block model of the East and West pipes of the Albany graphite deposit. (Conly & Moore, 2015; courtesy of Zentek Ltd.)

Chapter 2. METHODS

Eight drill holes were selected for this study: Zen 2, Zen 26, Zen 27, Zen 29, and Zen 30 from the West pipe and Zen 10, Zen 15, and Zen 18 from the East pipe (Fig. 2.1). The drill holes and sample intervals were selected to provide a representative sample suite across each pipe and a depth below the recognized weathering zone and to depths above the sill complex (Figs. 2.2 and 2.3).

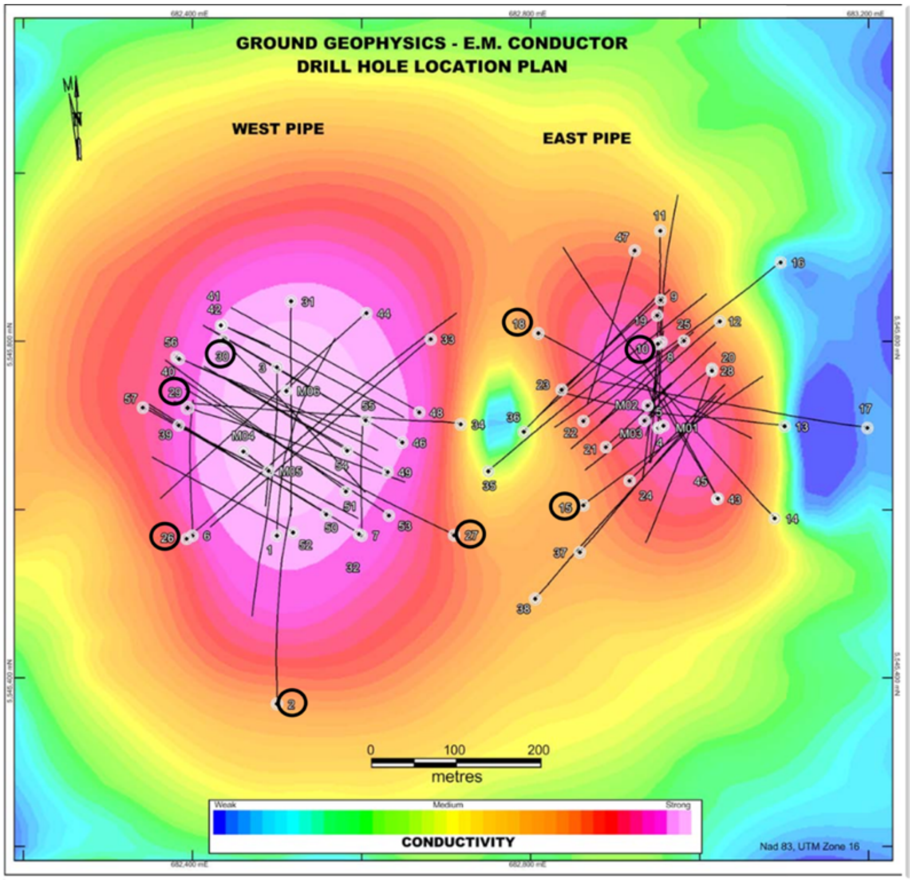

Figure 2.1 Results of ground TDEM survey and locations of drill holes (provided by Zentek Ltd.). The black circles represent the sampled drill holes.

Figures 2.2 and 2.3 indicate the examination of selected core logs from the East and West pipes. Overburden consists of outwash sediments, gravel, and muskeg, and it ranges from 51 m to 63 m in thickness. Sediments, with a thickness range from 3-10 m, are limestone. The typical lithology below the sedimentary units is a syenite with graphitic overprinting. The syenite with graphitic overprinting grades into the graphitic breccia, and both units alternate within the drill holes.

Graphite overprint means largely graphite. Graphitic overprint 1) occurs along intergranular boundaries of rock-forming minerals that comprise the wall rock or large (on the scale of several metres) breccia blocks, and 2) occurs as small (thin) veins, which have a low frequency of occurrence, and display limited degree of interconnectivity. In addition to felsic intrusive units (e.g., syenite, granite or diorite), mafic dykes, which are a few centimetres thick and small intrusive and felsic dyke are reported. Felsic dykes are characterized as being small (cm-scale) and cross-cut both breccias and non-brecciated lithologies.

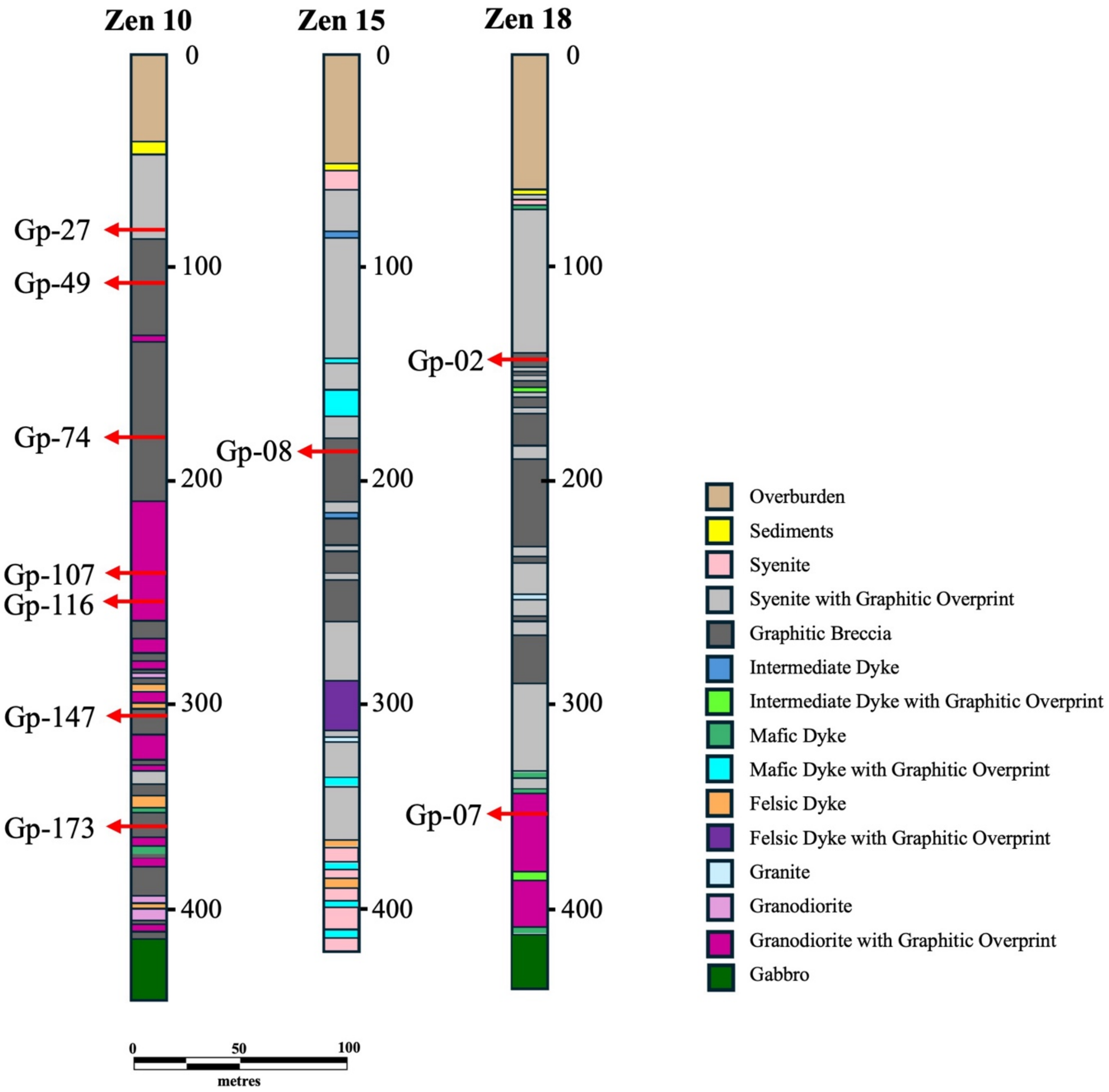

Figure 2.2 Graphic core logs of lithologies (based on Zentek drill logs) for the three drill holes from the East pipe. The locations of samples selected for petrographic observation are indicated with red arrows.

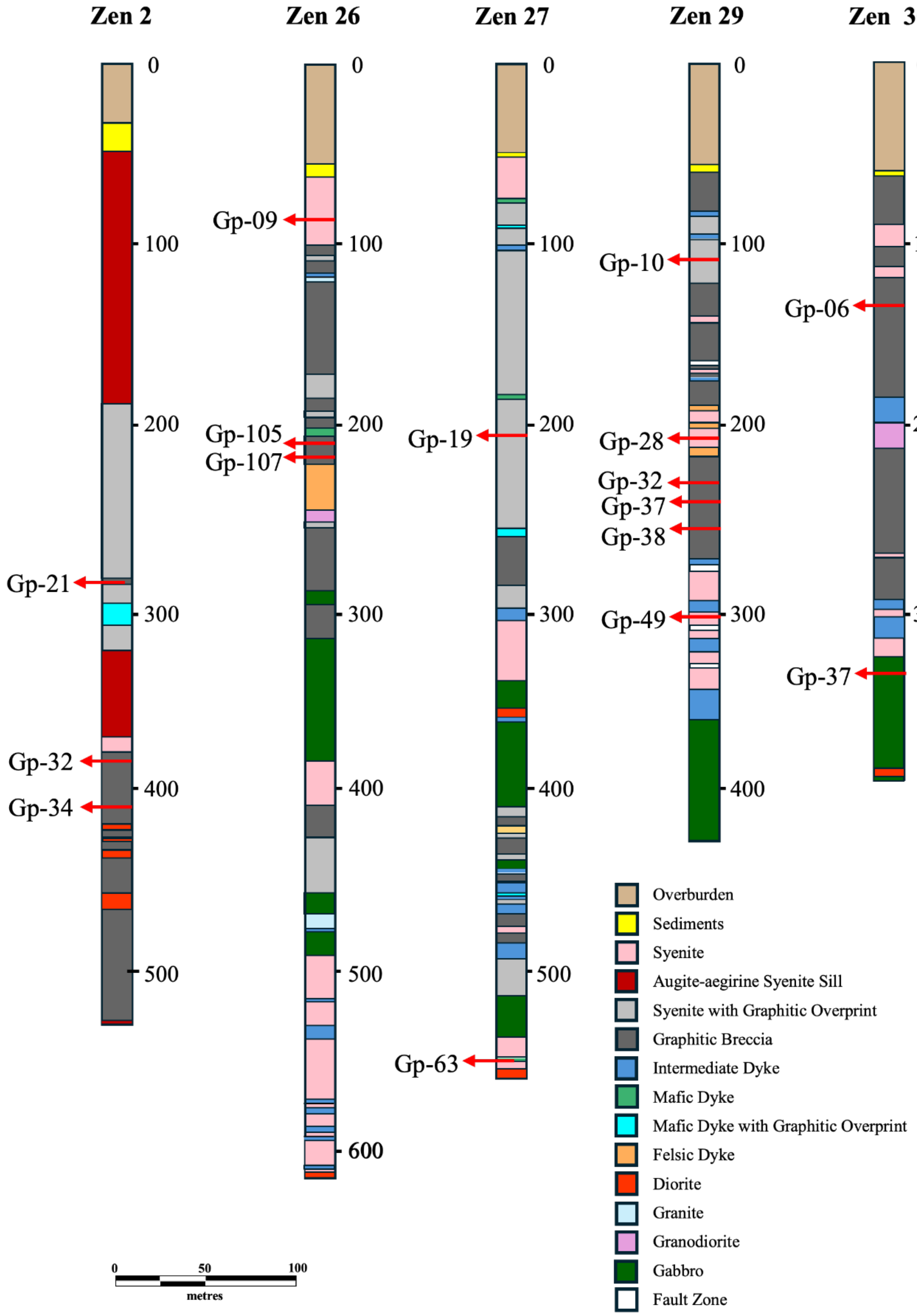

Figure 2.3 Graphic core log of lithologies (based on Zentek drill logs) for five selected drill holes from the West pipe and the locations of selected samples for petrographic observations are indicated with red arrows.

2.1 Optical Microscopy

Polished thin sections were prepared by the Department of Geology's lapidary facility and investigated using an Olympus Bx51 microscope (in both polarized and unpolarized transmitted and reflected light) equipped with an Olympus DP-70 camera at Lakehead University. Sixteen samples from the West pipe and ten from the East pipe were used to determine the Albany deposit's primary and secondary mineralogical, textural, and alteration characteristics. Samples were selected from different drill cores and depths from each pipe based on lithology (graphitic syenite breccia), the concentration of graphite (CG%), and graphite textures present.

2.2 Secondary Electron Microscopy - Energy Dispersive X-ray Spectrometry (SEM-EDS)

Due to much of the alteration mineralogy being fine-grained and/or forming finely intergrown assemblages, scanning electron microscopy-energy dispersive spectroscopy (SEM-EDS) was used for both mineral textural characterization and quantitative mineral chemical analysis. Eight samples were chosen for SEM-EDS analysis: Zen2-Gp-21, Zen2-Gp-32, Zen26-Gp-09, Zen26-Gp-105, Zen27-Gp-63, Zen29-Gp-32 from the West pipe and Zen10-Gp-107, Zen10-Gp-116 from the East pipe. SEM analyses were completed at the Lakehead Instrumentation Laboratory, Lakehead University, using a Hitachi SU-70 scanning electron microscope. Analyses were completed using an accelerating voltage of 20kV and a beam current of 300 pA. Compositional data were obtained using the attached Oxford AZtec with a processing time of 60 seconds. Elements are standardized using material from the Lakehead Instrumentation Laboratory standards library. The following elements and standards, along with their corresponding codes, are included: Si (pyroxene, DJ35), Al (corundum, LU-COR), Fe (Mnhortonolite, MN-HORT GI20), Mn (LU-MNSIO3), Mg (periclase, LU-PER), Ca (wollastonite, LU-WOLL), K (orthoclase, LU-ORTH), Na (jadeite, Lu-JAD), Ca, and P (apatite, LU-APAT1).

Chapter 3. RESULTS

3.1 Petrography

Through the integration of optical mineralogy and SEM-EDS analyses, a comprehensive, detailed mineralogical investigation was conducted. Textural relationships and the occurrence of graphite are documented through hand sample examination of representative core samples from both the West and East pipes, along with transmitted and reflected photomicrographs. The graphite-bearing rocks were classed and examined within three sub-groups, namely clast, matrix, and alteration assemblages. The modal abundances of minerals of the clasts and the matrix are normalized to 100% and given in Table 3.1 and Table 3.2. Transmitted and reflected light microscopy were utilized in this study, and modal percentages were based on visual estimation. Grain sizes are reported as very fine-grained (<0.1 mm), fine-grained (<1 mm), medium-grained (1 to 5 mm), and coarse-grained (5 to 12 mm).

3.1.1 Characteristics of Graphite in the Albany Deposit

Graphite occurs as elongated, lath-shaped, plate-like crystals that are <0.05 mm in width and range from 0.1 to 1.5 mm in length (Figs. 3.3a and b). The occurrence of graphite is controlled by the orientation of breccia fragments, crystal boundaries, and veins. Crystals are typically randomly oriented and show both intergranular and intragranular textures. The presence of these distinct textures provides valuable insights into the distribution of graphite within the breccia rocks in the pipes.

The intergranular texture occurs where graphite is restricted to the matrix, usually where it surrounds centimeter-sized angular to rounded fragments (Figs. 3.1 and 3.2). It is characterized by the extensive occurrence of graphite overprinting fragments (Fig. 3.1b), coinciding with graphite penetrating into the fragments along the crystal boundaries (Figs. 3.3a-3.3d). In the West pipe, graphite predominantly occurs with an intergranular texture. Intragranular graphite is also observed from photomicrographs of some samples from the West pipe (Figs. 3.3a and 3.3c). Both intergranular graphite and intragranular graphite were observed in the East pipe (Fig. 3.1c).

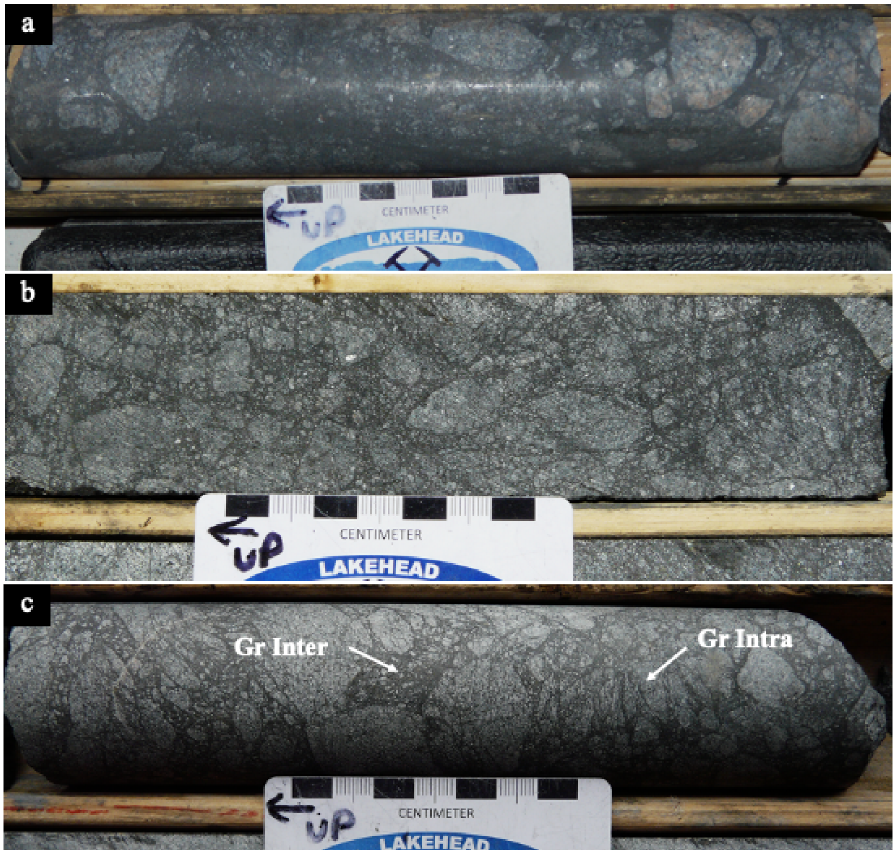

Figure 3.1 Images of drill core showing the two types of textures that graphite develops in. In image (a), from the West pipe, graphite is present with an intergranular texture, while in (b) from the East pipe, it only occurs with an intragranular texture. Sample (c) from the East pipe shows both textures. (Photographs of core samples courtesy of A. Conly).

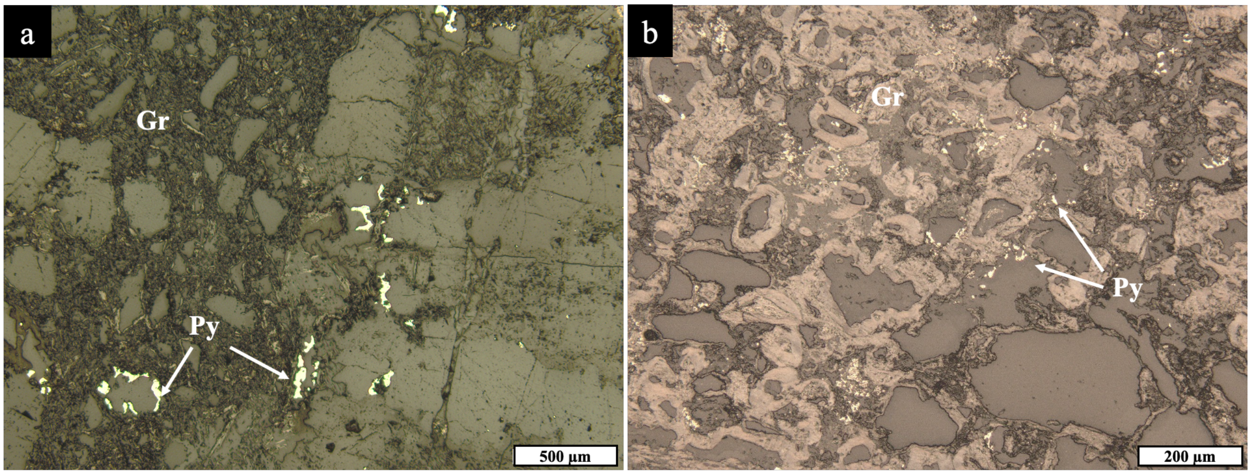

Figure 3.2 Reflected light photomicrographs of intergranular texture of graphite. Representative intergranular texture of graphite from (a) the West pipe and (b) the East pipe.

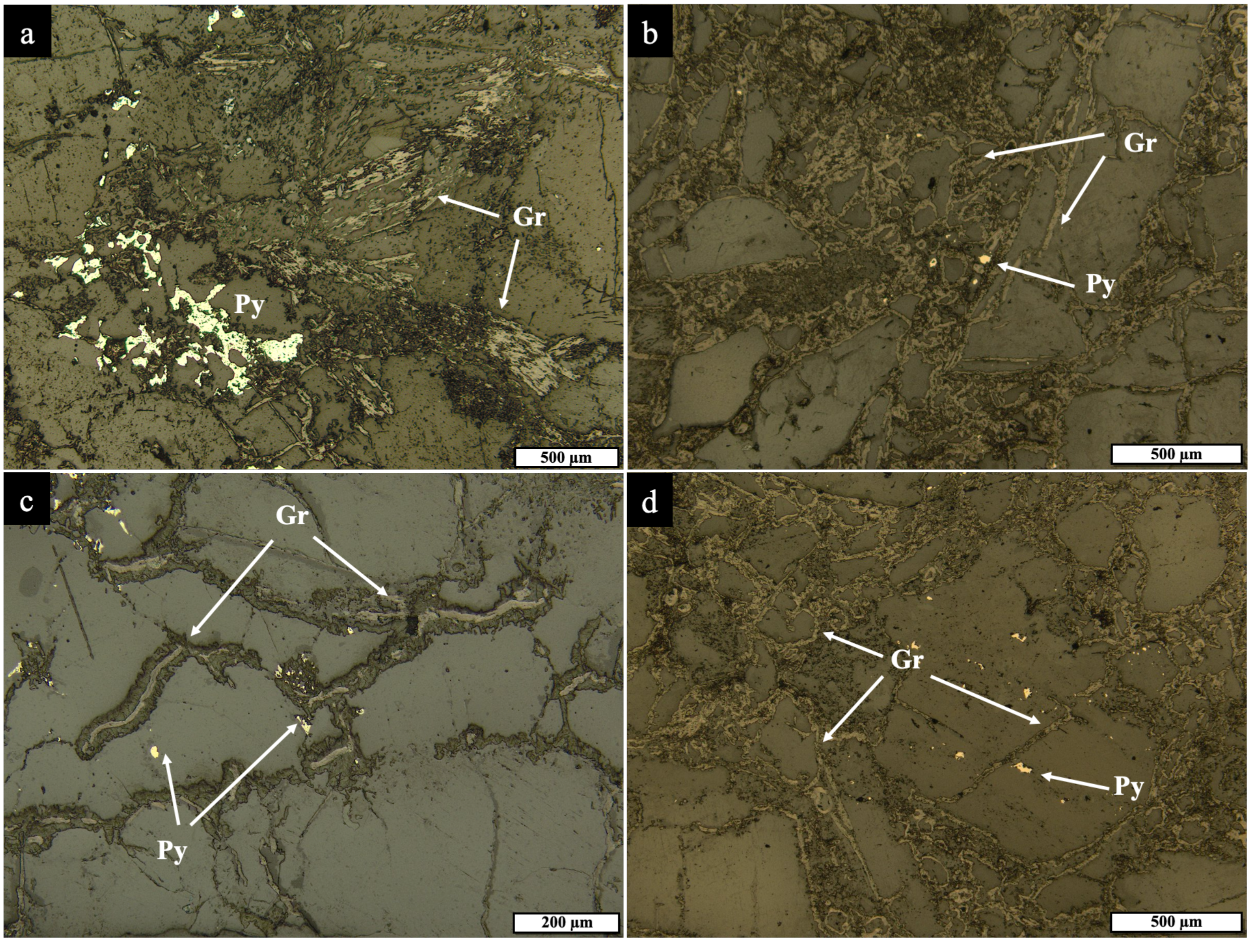

Figure 3.3 Reflected light photomicrographs of graphite showing an intragranular texture. Representative images show the intragranular texture of graphite from (a and c) the West pipe and (b and d) the East pipe.

Graphite occurs in both clasts and the matrix. The abundance of graphite in the matrix (<15%) is higher than that in the clast (<10%; see Tables 3.1 and 3.2). The selected image (Fig 3.4a) shows the typical graphite flakes distributed along grain boundaries of silicate minerals (predominantly quartz and plagioclase) comprising the clasts. Very fine-grained and anhedral biotite (Figs 3.4a) and calcite (Figs 3.4b) are found intergrown with graphite in this sample. In the matrix, graphite commonly shows an intergranular texture (Fig 3.4a). Another common occurrence of graphite in the matrix is situated along a biotite schist fragment, with a lower amount of graphite penetrating the quartz-rich fragment along grain boundaries (Figs 3.4d and 3.4e). Graphite is often associated with very fine to fine-grained pyrite, the predominant sulphide mineral (Figs 3.4c and 3.4f).

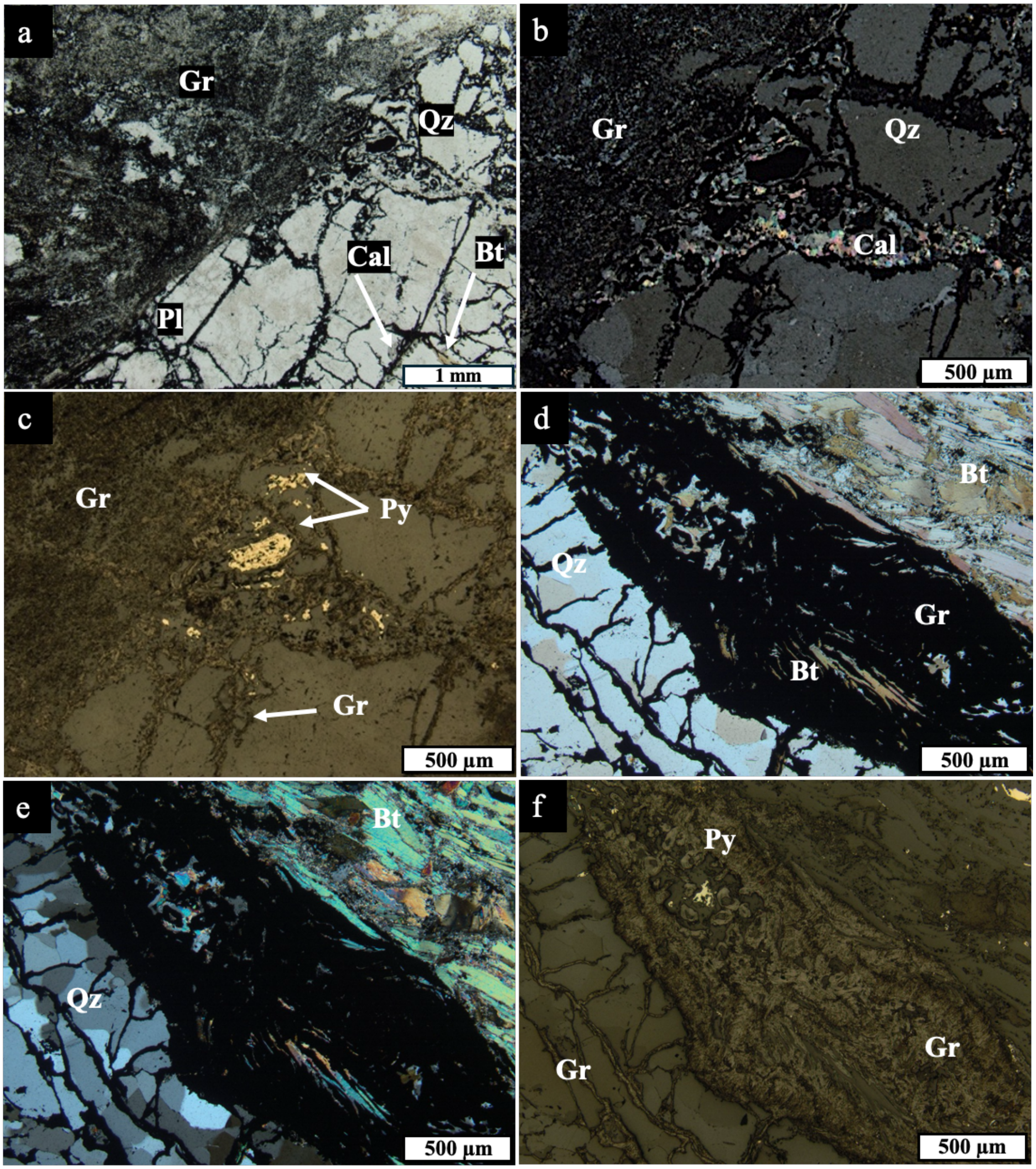

Figure 3.4 Photomicrographs of the occurrence of graphite in the matrix and along the boundaries of silicate fragments. Plane polarized (a) and cross-polarized (b) transmitted light and reflected light (c) photomicrographs showing textural relationship and the occurrence of graphite in the matrix and along the boundaries of silicate fragments. Calcite and biotite are intergrown with graphite and associated with pyrite. Plane polarized (d) and cross-polarized (e) transmitted light and reflected light (f) photomicrographs showing deposited graphite is deposited along the biotite schist fragment, while it is penetrating along grain boundaries of quartz fragment.

3.1.2 Clast Petrography

Although both matrix and clast contain polymineralic and monomineralic components, their proportions differ significantly. The matrix exhibits a higher proportion of monomineralic components, while the clast displays a higher abundance of polymineralic components. Furthermore, the definitions of matrix (<1.5mm) and clast (>1.5mm) differ in grain size. The matrix is comprised of lithic fragments derived from clasts. The predominant minerals in the clasts are plagioclase (20-25%) and potassium feldspar (15-20%), typically exhibiting sizes less than 3 mm and a crystal habit that is subhedral to anhedral (Table 2.1, Figs. 3.5a and 3.5b). Quartz typically constitutes less than 15% of a clast and has a size range from fine to medium-grained (<2 mm). Quartz often exhibits an interlocking texture with plagioclase and potassium feldspar, as shown in Figures 3.5a and 3.5b. Clasts display varying degrees of alteration, but alteration is generally weak. Sericitation of plagioclase and potassium feldspar is present, with between 5% and 50% replacement, although 10 to 15% is typical. Sericite alteration typically occurs as fine dusting (Fig. 3.6a). Although not very common, a graphic texture (Fig. 3.6b) and also perthitic texture (Fig. 3.6d) have been observed with quartz in potassium feldspar. Sericitization occurs along fractures within quartz grains, while it occurs disseminated in plagioclase and potassium feldspars (Fig. 3.5d). Accessory minerals include apatite, titanite, and zircon.

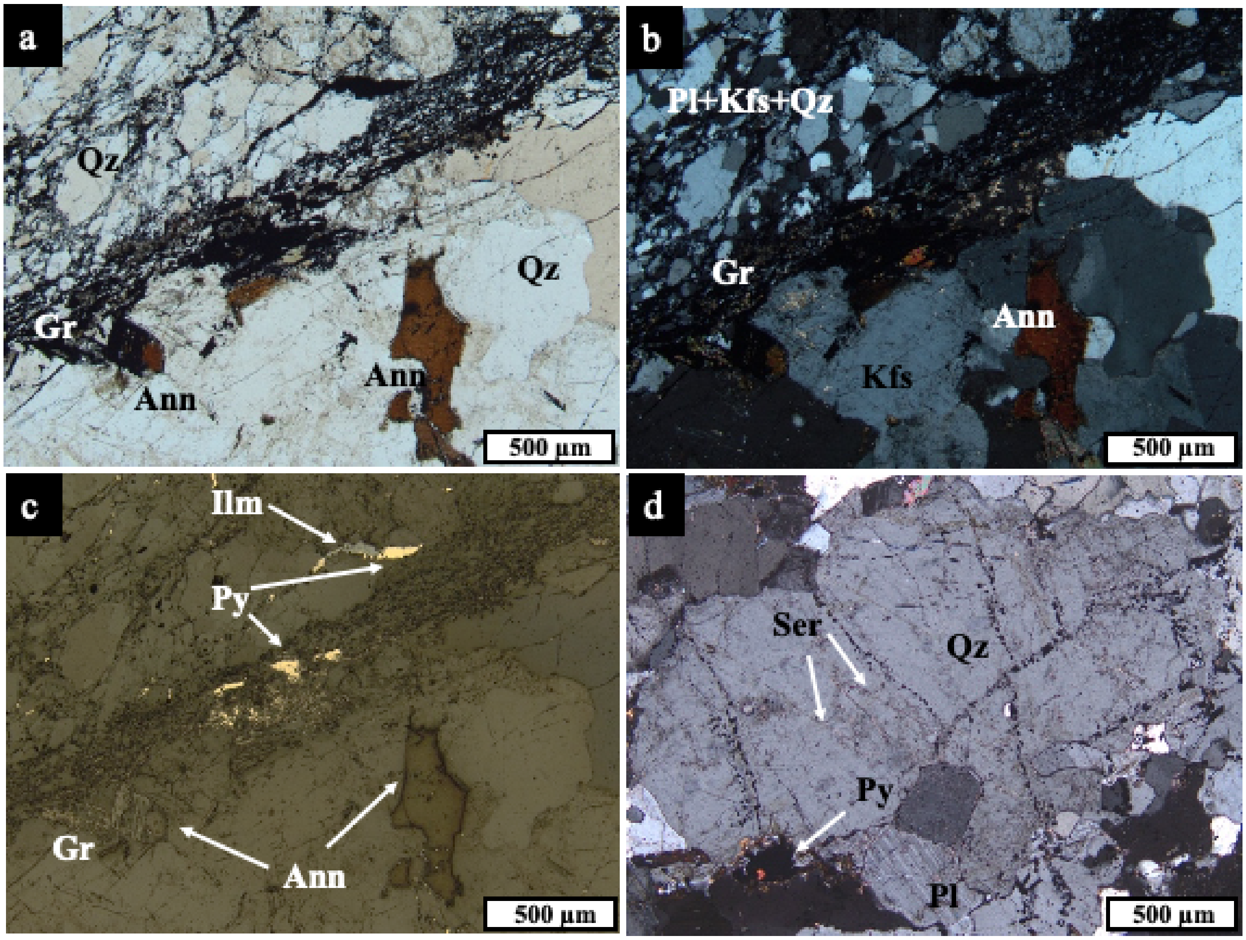

Figure 3.5 Photomicrographs of both fragments and matrix components of the breccias. Plane polarized (a), cross-polarized (b) transmitted light and reflected light (c) photomicrographs, which show textural relationships and representative mineralogies of both fragments and the matrix components of the breccias. Cross-polarized (d) transmitted light photomicrograph shows along fractures of medium quartz grain (<3mm) has sericite and it is interstitial to plagioclase.

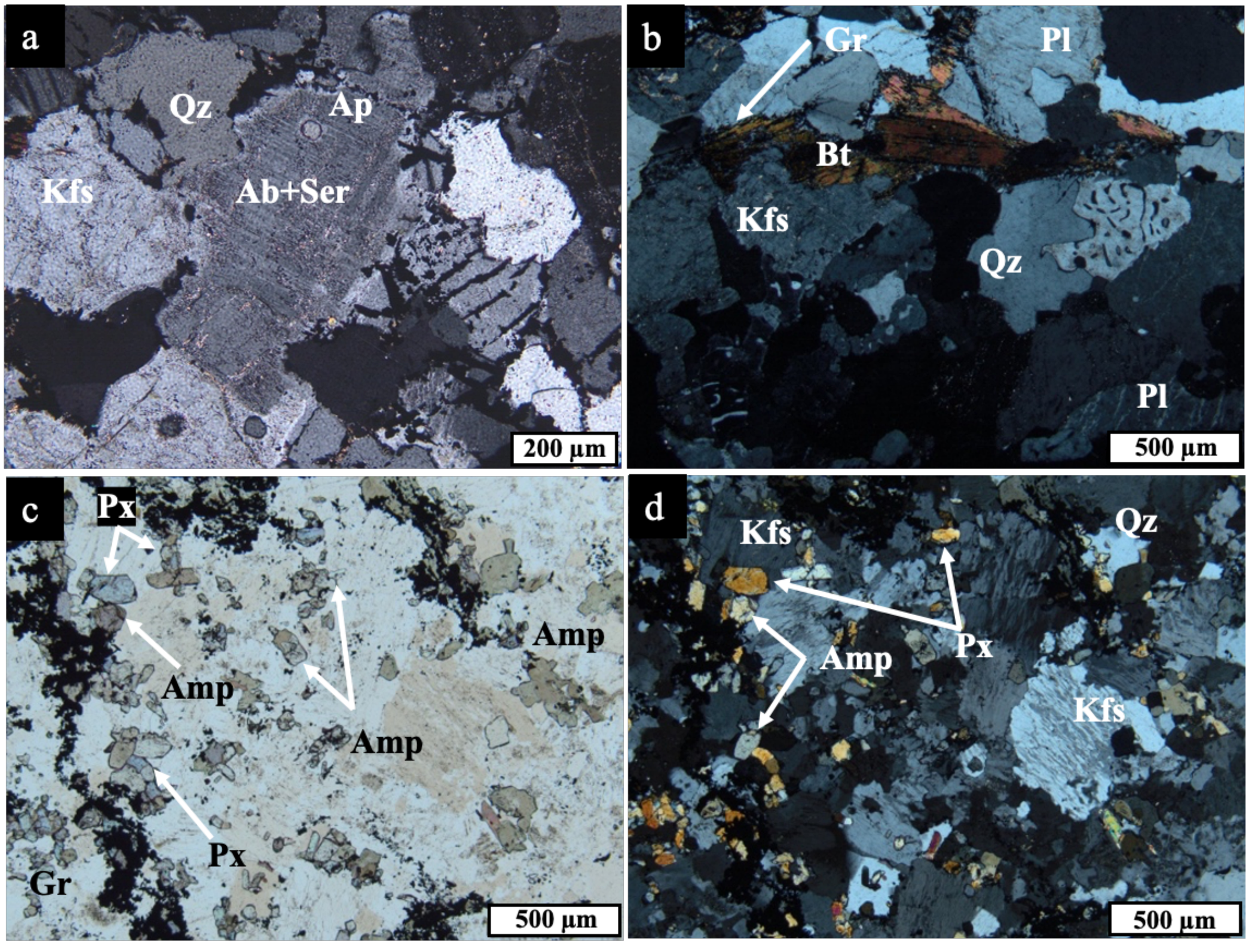

Figure 3.6 Photomicrographs of components of a clast. Cross-polarized (a) transmitted light photomicrographs show weak to moderate sericitization of plagioclase and potassium feldspar. Cross-polarized (b) transmitted light photomicrograph shows graphic intergrowths of quartz and potassium feldspar. Also, it exhibits an isolated grain of biotite, which has graphite deposited along its cleavage planes. Plane-polarized (c) transmitted light photomicrographs showing subhedral amphibole and pyroxene grains associated with graphite. Cross-polarized (d) transmitted light photomicrographs showing the perthitic texture in potassium feldspar.

The abundance of annite is up to 15%. It mainly occurs as fine-grained, euhedral to subhedral isolated grains (Figs. 3.5a, 3.5b, and 3.6b). Annite is associated with quartz and feldspar, and graphite flakes are deposited along its cleavage planes (Figs. 3.5c and 3.6b). Based on petrographic observations, three types of biotite exist in the clasts. Euhedral to subhedral annite crystals up to 1 mm in size show a strong pleochroism, ranging from light to dark brown (Figs. 3.7a and 3.7b). Annite crystals occur interstitial to rock-forming silicates such as plagioclase, potassium feldspar, and quartz within clast (Figs. 3.7c and 3.7d). Due to displaying igneous texture, this annite will be referred to as igneous annite in the chemical result.

While most biotite in the clasts is annite (see section 3.2.1), SEM-EDS analysis did lead to the identification of phlogopite in one sample. It is in association with pyroxene, amphibole, euhedral ilmenite, and key accessory minerals (chromite and apatite) in the clast (Fig 3.7f). Moreover, graphite is seen to be situated parallel to the cleavage of the very fine grain phlogopite grain (Fig. 3.7e). Notably, BSE imaging of the phlogopite in Figure 3.7f suggests that the pipes include fragments of brecciated lamprophyre.

Elongated biotite schist fragments, euhedral to subhedral and platy, show a green-light brown colour. These fragments were observed as isolated (Fig. 3.8a) and well-foliated biotite schist, which shows interlocking textures (Fig. 3.8b-d). Moreover, they are associated with potassium feldspar, plagioclase, and quartz. Biotite schist fragments will be called metamorphic annite. In general, igneous annite do not exhibit direct contact with graphite as shown in Figure 3.7. However, graphite was observed to be deposited parallel to the foliation of metamorphic annite (Fig. 3.8).

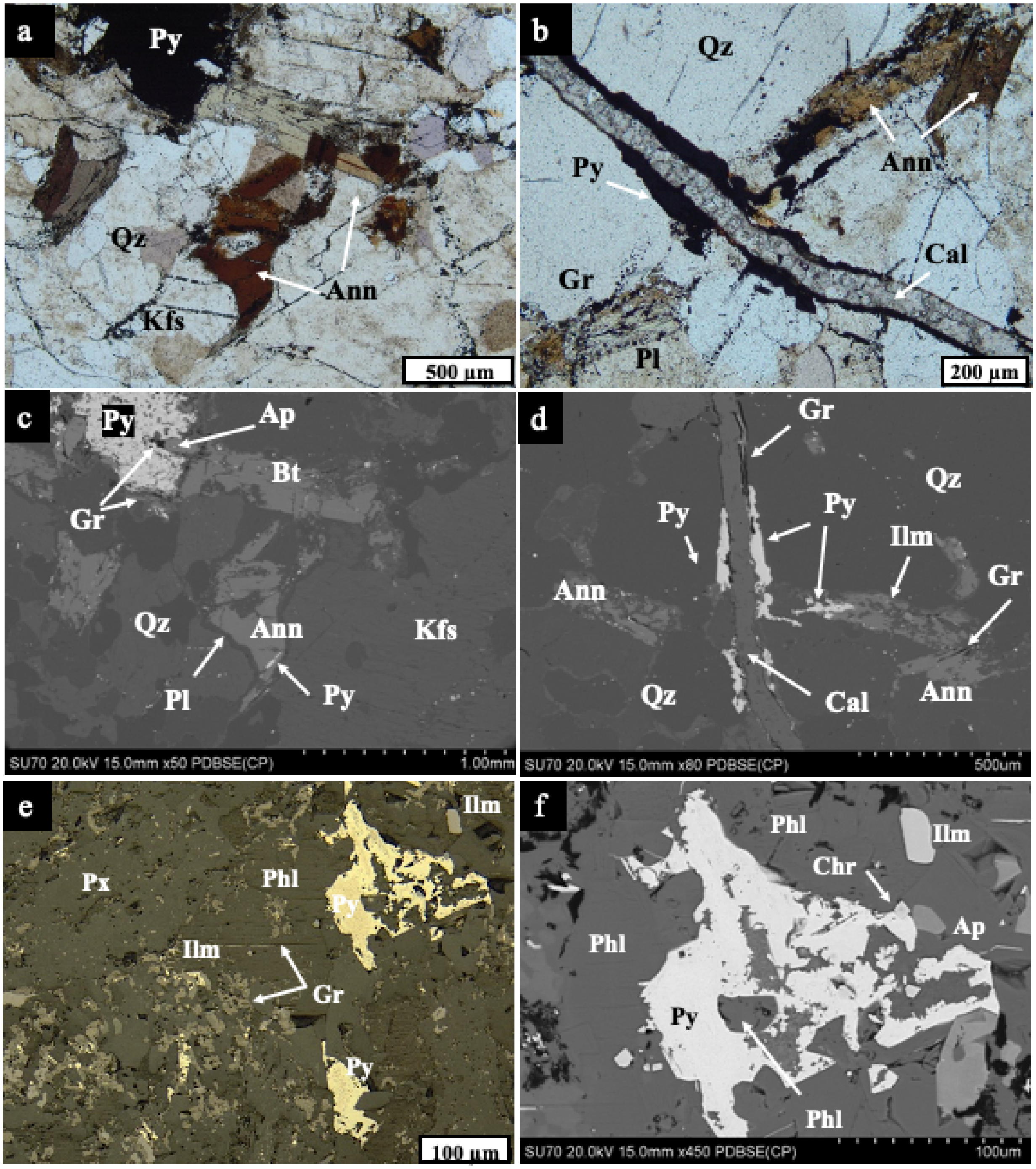

Figure 3.7 Photomicrographs and BSE images of igneous annite. Plane-polarized (a) and (b) transmitted light photomicrographs igneous annite, which has a typical strong brown colour within the clast. (b) illustrates that the igneous annite is interstitial to the quartz and plagioclase fragments, which are cut by calcite veins. BSE images (c) and (d) display common pyrite and very fine-grained (<50 µm) less abundant

ilmenite associated with igneous annite. Reflected (e) photomicrograph and BSE (f) image of very fine-grained, irregularly shaped pyrite interstitial to phlogopite.

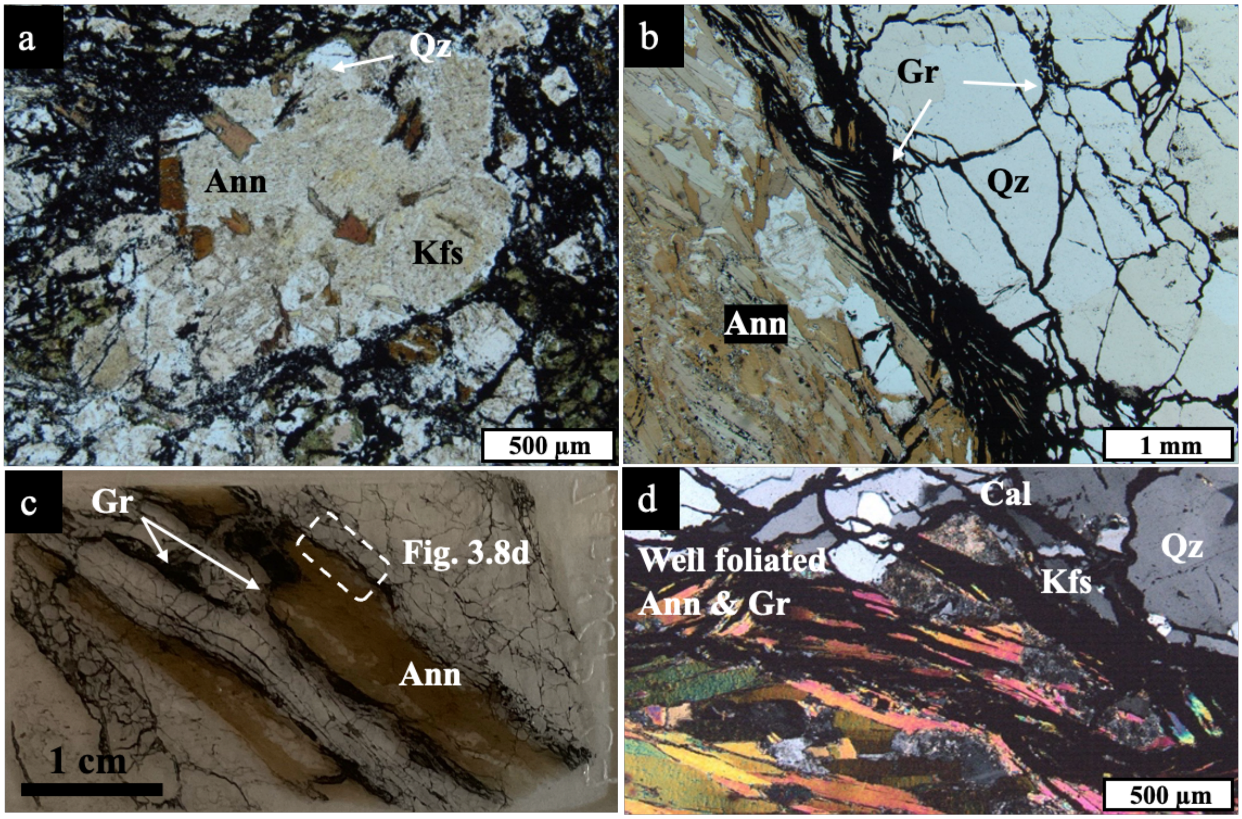

Figure 3.8 Photomicrographs and BSE images of metamorphic annite. Plane-polarized (a) and (b) transmitted light photomicrographs show representative metamorphic annite, which has a typical green-light brown colour within the clast. (a) illustrates the subhedral isolated biotite schist fragment is in contact with potassium feldspar. (b) exhibit typically elongated biotite schist, which shows interlocking texture. Many graphite flakes are >1mm in length. The thin section (c) photograph shows graphite is situated between a biotite schist-rich fragment and a quartz-rich fragment. Cross-polarized (d) transmitted light photomicrograph shows the textural relationship of graphite and well-foliated biotite schist fragment.

The abundance of amphiboles is less than 5%. Amphibole exhibits a variable grain size, ranging from very fine to fine (Fig. 3.9a). Amphiboles, which mostly exhibit euhedral crystal shape, are found together with rock-forming silicates such as plagioclase, potassium feldspar, and quartz within the clast (Figs 3.9b and 3.9e). Additionally, amphibole fragments are usually observed to be associated with pyroxene in the clast (Fig 3.9d). The pyroxene (3-5%) is very fine-grained and euhedral (Figs. 3.6c and 3.6d). Both pyroxene and amphibole crystals are seen in contact with graphite. Graphite flakes are found deposited along the cleavages of amphibole (Fig. 3.9f).

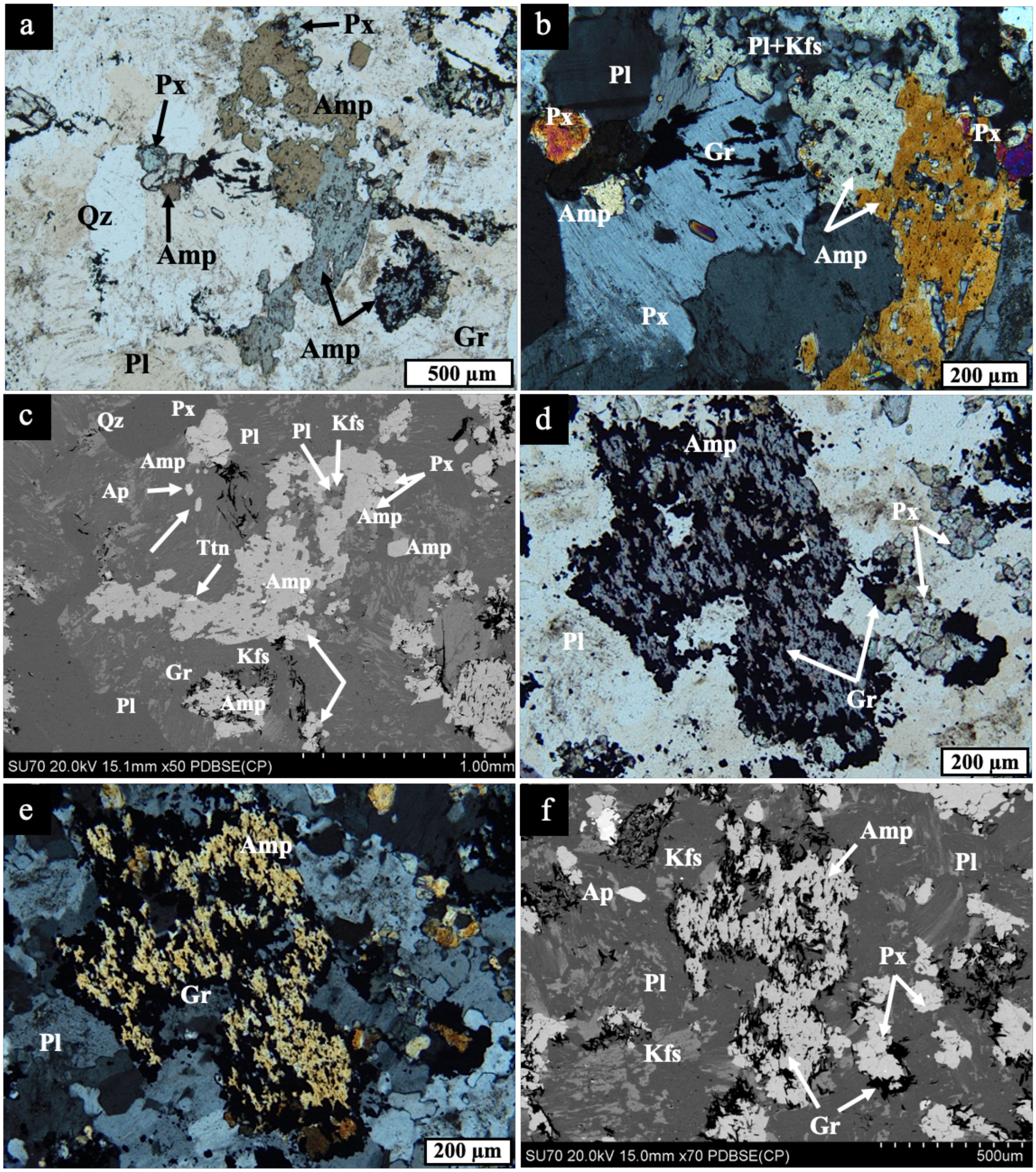

Figure 3.9 Photomicrographs and BSE images of igneous amphibole. Plane-polarized (a) and (d), cross-polarized (b) and (e) transmitted light photomicrographs and BSE images (c) and (f) display the typical occurrence of amphibole crystals in the clast and their textural relationship with graphite.

Very fine-grained, anhedral chlorite (3-5%) occurs interstitially to graphite and the main rock-forming minerals (Fig. 3.10a-b). It is observed penetrating along the grain boundaries in the clast. Sulphides occur as agglomerated masses of subhedral to anhedral crystals. Very fine-grained, subhedral to anhedral pyrite (less than 3% abundance) and trace amounts of chalcopyrite are observed within the clasts. Figures 3.10c and 3.10d show sulphides as being interstitial to the main rock-forming minerals. Trace amounts of very fine-grained, anhedral ilmenite are observed within the clasts frequently in association with annite. Furthermore, the presence of ilmenite, associated with graphite and pyrite, is frequently seen along the grain boundaries of brecciated clasts (Fig. 3.5c). As accessory minerals, apatite, titanite, and zircon, are very fine-grained and euhedral, and are interstitial to other accessory minerals and the main rocking forming minerals (Fig. 3.10c). Euhedral apatite, the most common accessory mineral, occurs interstitially to quartz, feldspar, and pyrite (Figs. 3.6a and 3.10). In the clasts, euhedral zircon and titanite are commonly observed interstitial to chlorite and pyrite, respectively.

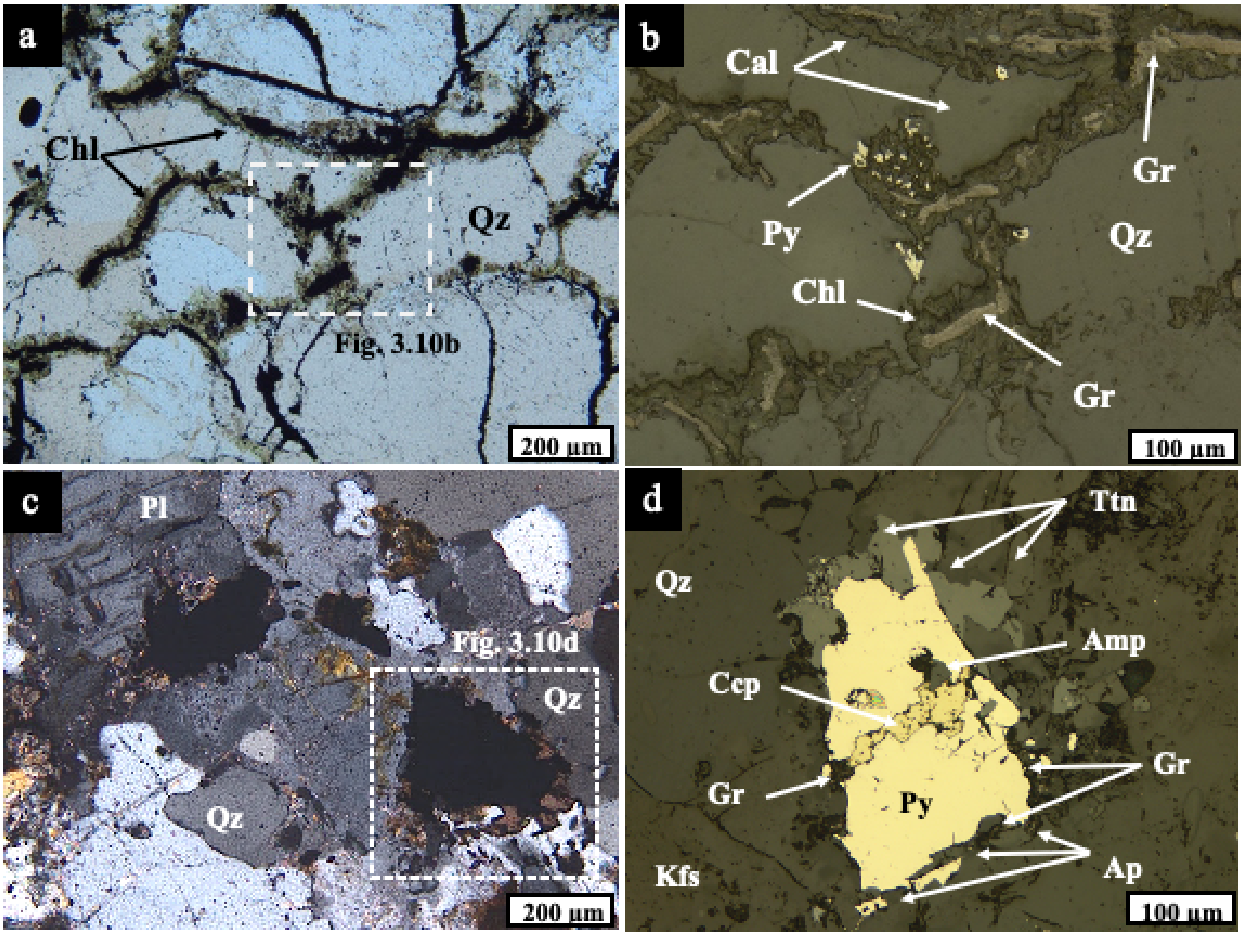

Figure 3.10 Representative photomicrographs of chlorite, sulphide, and accessory mineral in the clast. Plane-polarized (a) transmitted and reflected (b) light photomicrographs exhibit chlorite intergrowing with graphite along the boundaries of a quartz fragment and associated with pyrite. Cross-polarized (e) transmitted photomicrograph displays the occurrence of pyrite interstitial to silicates in the clast. Reflected (f) light photomicrograph displays very fine-grained amphibole enclosed in pyrite, while chalcopyrite is interstitial with pyrite grain.

Table 3.1 Clast mineral abundance. Sulphide minerals include pyrite and chalcopyrite, while Fe-oxide minerals include ilmenite and magnetite. Accessory minerals include apatite, titanite, chromite, and zircon.

Minerals	Abundance	Size	Habit
Plagioclase	20-25%	Fine - Medium	Subhedral - Anhedral
Potassium feldspar	15-20%	Fine - Medium	Subhedral - Anhedral
Quartz	<15%	Fine - Medium	Subhedral - Anhedral
Biotite	<15%	Fine - Medium	Euhedral - Subhedral
Graphite	<10%	Fine	Lath-shaped/Plate-like
Amphibole	<5%	Very fine - Fine	Euhedral - Subhedral
Pyroxene	3-5%	Very fine	Euhedral
Chlorite	3-5%	Very fine	Anhedral
Carbonate	<2%	Fine - Medium	Euhedral - Subhedral
Sulphides	<3%	Very fine - Fine	Subhedral- Anhedral
Fe-Oxides	<1%	Very fine	Anhedral
Accessory minerals	<1%	Very fine	Euhedral

3.1.3 Matrix Petrography

The matrix is mainly comprised of equigranular plagioclase, potassium feldspar, quartz, biotite, and graphite (Table 3.2). The most abundant minerals in the matrix are anhedral to subhedral plagioclase (20-25%) and potassium feldspar (<20%), which are <1 mm in size (Fig. 3.11a). Variable amounts of sericite alteration occur in patches within plagioclase and potassium feldspar, ranging from 20% to 100%, with an average of 40% (Figs. 3.11b). Quartz (15-20%) is dominantly fine-grained and anhedral. Biotite, which represents 10% of the matrix, is up to 500 µm in size and anhedral. Anhedral biotite (<10%) is found altering the plagioclase and potassium feldspar crystals within the matrix (Figs. 3.11c and 3.11d).

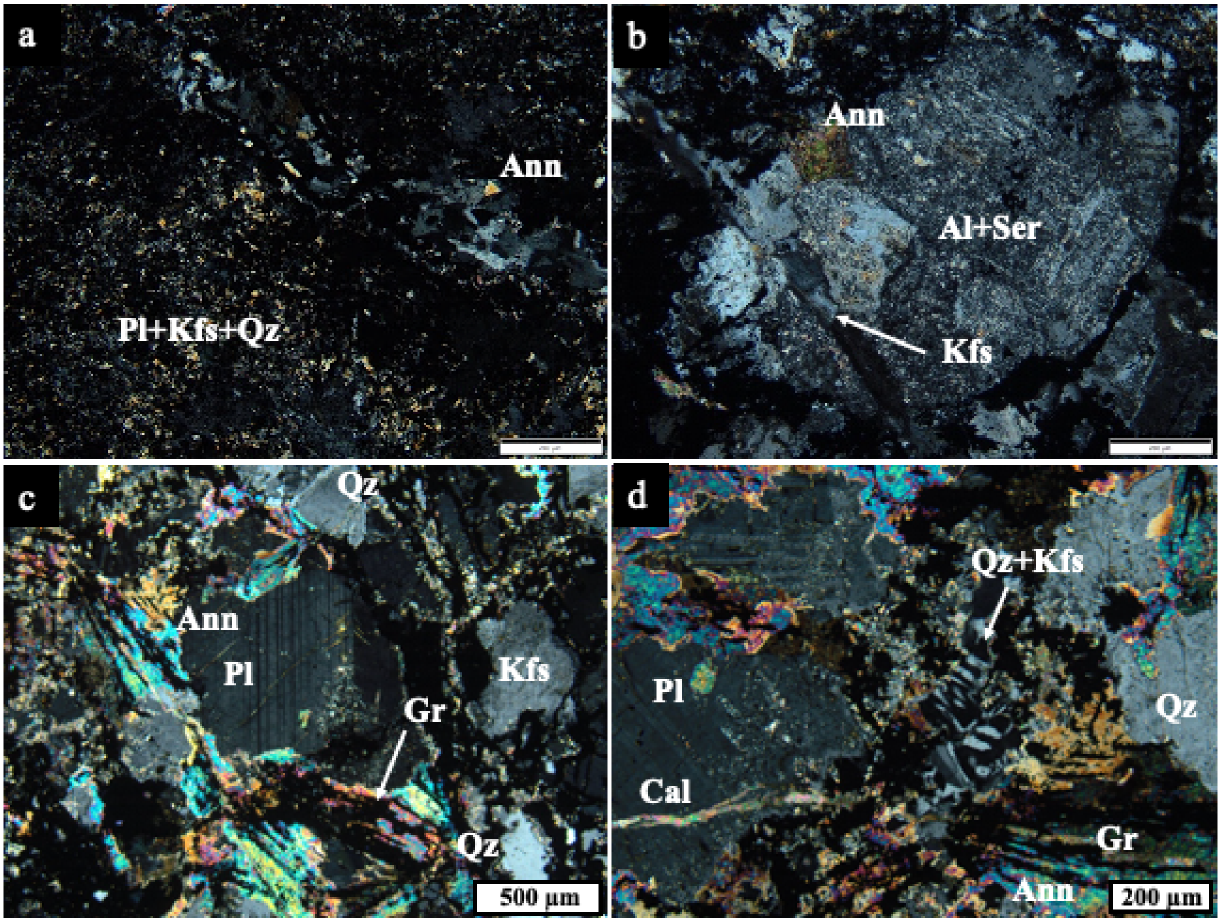

Figure 3.11 Representative photomicrographs of matrix components. Photomicrographs (a-d) were taken from cross-polarized transmitted light. (a) illustrating the distribution of grain size distribution and mineral composition of the matrix. (b) annite grain interstitial to plagioclase and potassium feldspar, which are pervasively sericitized in the matrix. (c) and (d) display quartz, plagioclase, and potassium feldspar altered by subhedral-anhedral annite and anhedral calcite. Graphic intergrown of quartz in potassium feldspar is also seen in (d).

Very fine-grained and anhedral carbonates comprise less than 5% of the matrix. Carbonate was seen mainly enveloping quartz and feldspar grains (Fig 3.12a). Carbonates, which exhibit rim replacement of the plagioclase and potassium feldspar, are often found to be associated with annite in the matrix. Anhedral amphibole altered to annite (up to 2%) is found at the boundaries of quartz and intergrown with rock-forming silicates. Also, it is commonly seen interstitial to pyroxene and phlogopite in clast (Fig. 3.12b). Trace amounts of euhedral to subhedral ilmenite (Figs. 3.7e and f) and lesser amounts of magnetite are observed within the matrix. While very fine-grained pyrite is the dominant sulphides (2%), sphalerite was seen in a few samples. Pyrite is frequently observed interstitial to graphite and rarely interstitial to fine-grained phlogopite grain (Fig 3.7f). Trace minerals include apatite, titanite, and zircon.

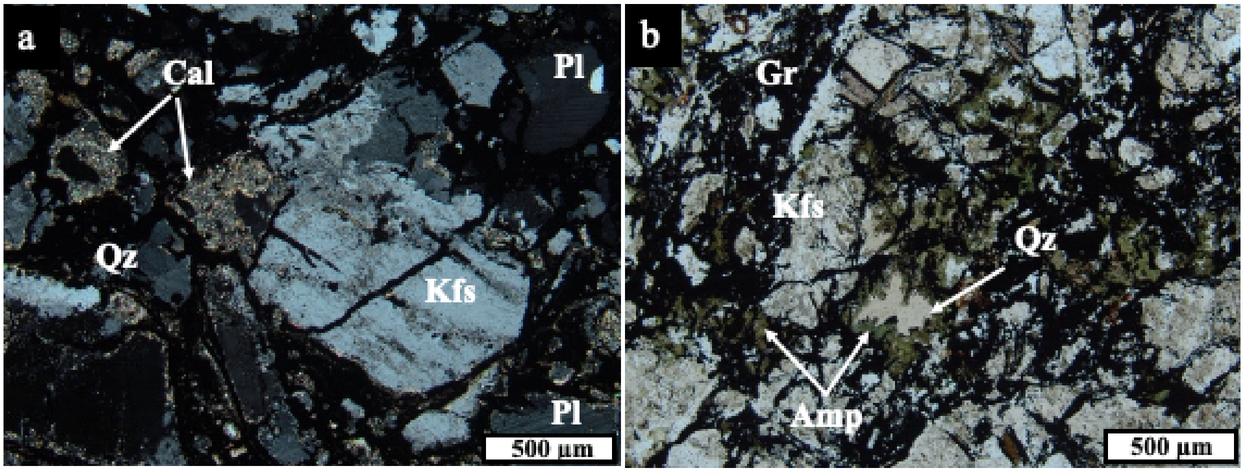

Figure 3.12 Representative photomicrographs and BSE images of matrix components. Cross-polarized (c) transmitted light photomicrographs exhibit the presence of very fine-grained carbonate rimming quartz and potassium feldspar. Plane-polarized (d) transmitted light photomicrograph exhibits amphibole altered by annite, which is seen with the silicate crystals in the matrix.

Table 3.2 Matrix mineral abundance. Sulphide minerals include pyrite and sphalerite. Fe-oxide minerals include ilmenite and magnetite. Accessory minerals include apatite, titanite, and zircon.

Minerals	Abundance	Size	Habit
Plagioclase	20-25%	Very fine-Fine	Subhedral - Anhedral
Potassium feldspar	<20%	Very fine -Fine	Subhedral - Anhedral
Quartz	15-20%	Very fine - Fine	Anhedral
Graphite	<15%	Fine	Lath-shaped/Plate-like
Biotite	<10%	Very fine - Fine	Anhedral
Carbonate	<5%	Very fine	Anhedral
Amphibole	<2%	Very fine	Anhedral
Pyroxene	<3%	Very fine	Anhedral
Sulphides	<2%	Very fine	Anhedral
Fe-Oxide	<1%	Very fine -Fine	Euhedral-Subhedral
Accessory	<2%	Very fine - Fine	Euhedral-Subhedral

3.1.4 Carbonates

Dominantly calcite and dolomite are the carbonate minerals observed. Calcite occurs commonly in veins, while isolated fragments are observed in a few samples. Veins are approximately 100µm wide and 3cm in length. The grain size of calcite forming the vein is very fine-grained (30µm- 100µm), and the crystal habit is dominantly anhedral. These veins are observed to cut both the matrix (Fig. 3.13a) and the clast (Figs. 3.13b and 3.13c). Although the main mineral composition of the clast and matrix are similar, the grain size and morphology differ. The quartz, plagioclase, potassium feldspar, and annite fragments range from fine to medium-grained and are subhedral in the clasts, while grains in the fragments in the matrix are very fine-grained and anhedral. Graphite is often observed at the boundaries between calcite and the associated minerals (Fig. 3.13d and 3.7b (reflected light photomicrograph of 3.13b)). Pyrite is frequently seen as associated with calcite, and chalcopyrite may present but is rare (Figs. 3.7b, 3.13a, and 3.13d). Calcite grain sizes can reach up to 1.75 mm but typically range from 0.5 to 1.0mm. It is found to fill intergranular open space in the clast and interstitial to plagioclase and potassium feldspar (Fig. 3.14a). Additionally, calcite is also occasionally observed to be associated with anhedral chlorite and disseminated graphite (Fig. 3.14a). Compared to calcite, dolomite is more rare. It is often found in veins with widths of 1 mm and lengths of >6 cm. Dolomite vein cross-cut clasts consisting of rock-forming silicates and graphite (Fig. 3.14c). In one sample taken from the West pipe, tiny chlorite veinlets (Figs. 3.14d and 3.14e) have been observed within the dolomite vein (Fig. 3.14f).

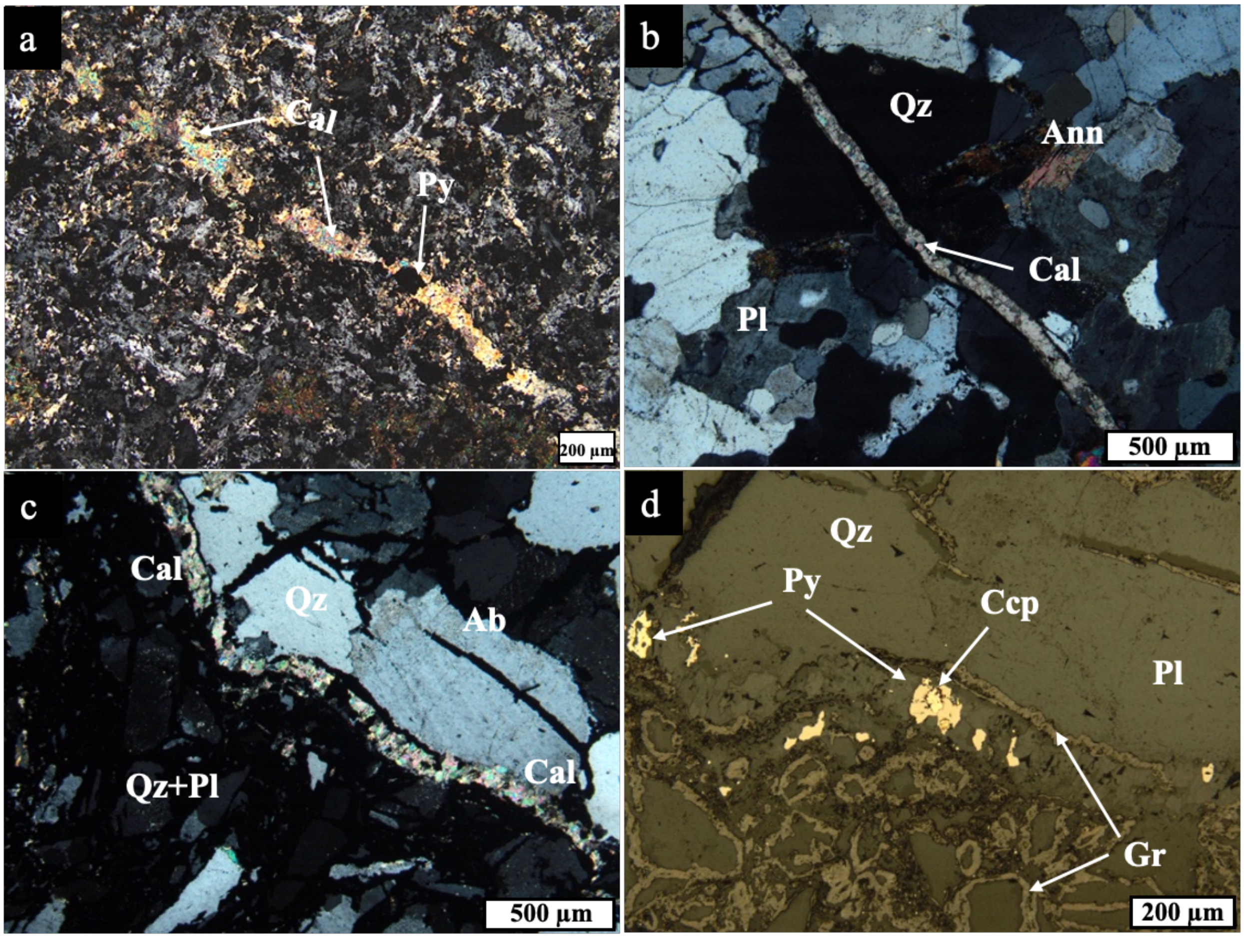

Figure 3.13 Photomicrographs of calcite veining. Calcite vein in cross-polarized (a), (b), and (c) transmitted light exhibit the matrix cut by the calcite vein. Reflected (d) light photomicrograph shows graphite occurs along the calcite vein and is associated with pyrite and chalcopyrite. (The scale bar is 200 µm for (a) in the bottom right).

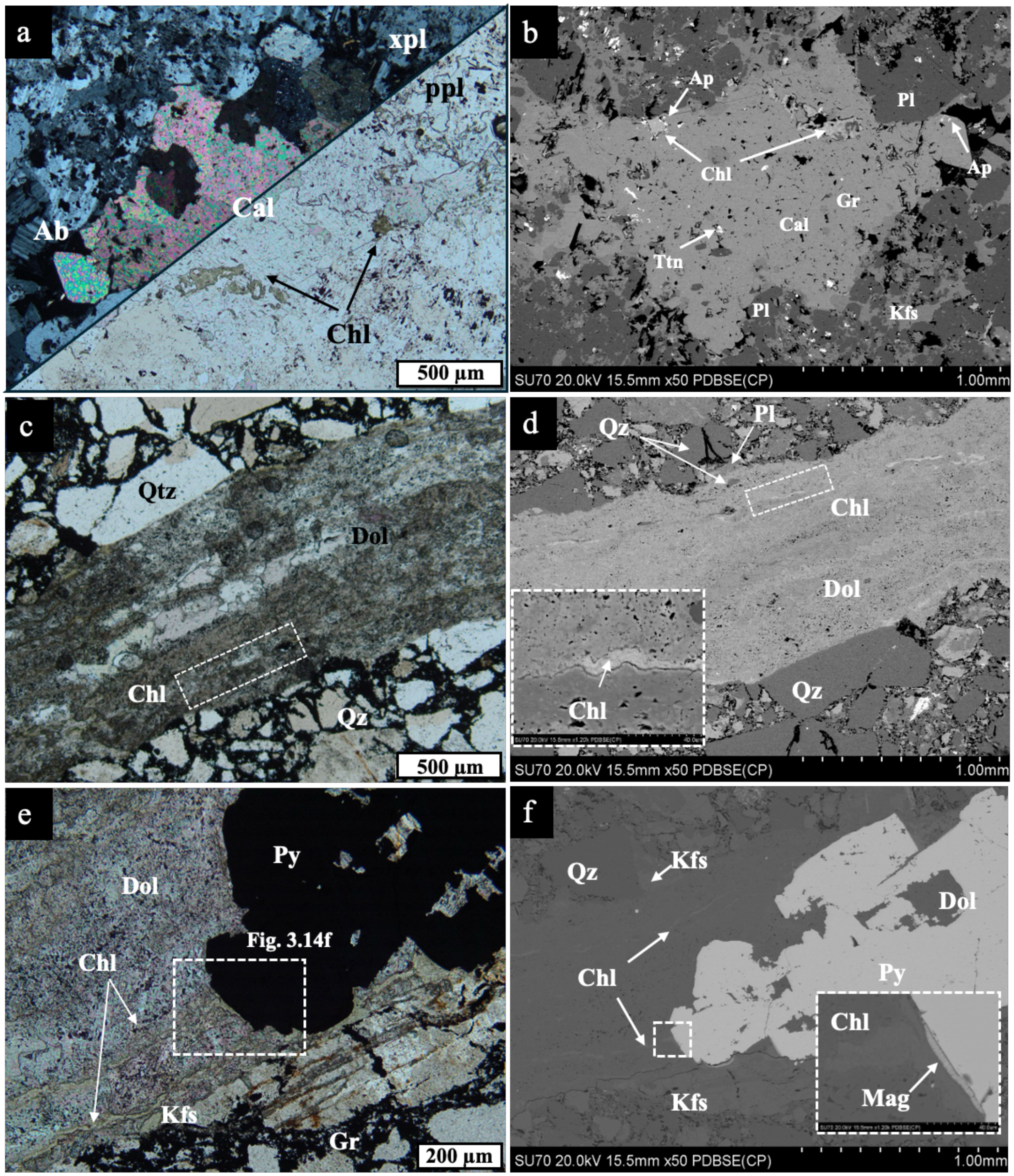

Figure 3.14 Photomicrographs and BSE images of isolated calcite grains and dolomite veining. Plane-polarized and cross-polarized transmitted light photomicrograph (a) and BSE image (b) display isolated calcite grain filling the intergranular open space and interstitial to chlorite. Photomicrographs of dolomite vein in plane-polarized (c) and (e) transmitted light and BSE (d) and (f) images (c) shows the matrix cut by the dolomite vein which contain tiny chlorite veinlets with pyrite and magnetite.

3.1.5 Alteration

An alteration assemblage of minerals that show replacement textures, including annite, calcite, and chlorite. Annite is a randomly oriented aggregate of anhedral, dominantly very fine-grained (typically <200 μm) crystals that occur in both clast and matrix. These annite grains are characterized by exhibiting a replacement texture and are referred to as hydrothermal annite. Hydrothermal annite crystals commonly occur as intergrowth or overgrowth with plagioclase and potassium feldspar, and replaces both feldspar grains in the matrix (Figs. 3.15a and c). It is also often associated with very fine-grained calcite within the matrix. Besides the rim replacement, some of the plagioclase is seen to be completely altered by hydrothermal annite and calcite (on the right side of Fig. 3.15a). Potassium feldspar is weakly replaced by hydrothermal annite, and it is seen adjacent to quartz grains in the matrix. These quartz grains are rarely observed cut by continuous and discontinuous calcite veins in the matrix (Fig. 3.15b). Moreover, hydrothermal annite replaces amphibole, which is found intergrown with plagioclase, potassium feldspar, and quartz in a sample examined (Figs. 3.15e and f). By being in direct contact with graphite, hydrothermal annite is distinguished from igneous and metamorphic annite, which are rarely in contact with graphite.

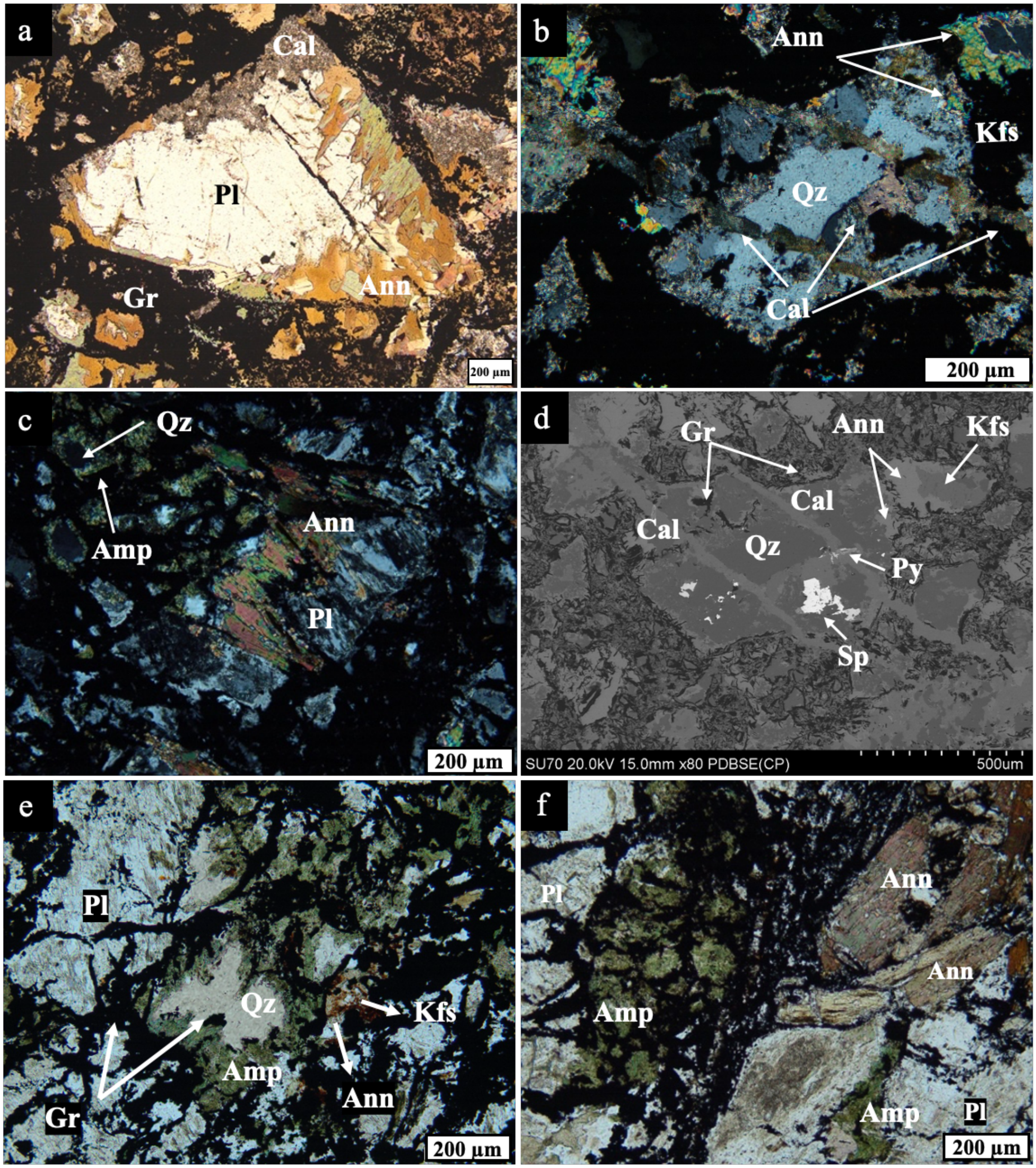

Figure 3.15 Representative photomicrographs of annite alteration. Cross-polarized (a-c) transmitted light photomicrographs show hydrothermal annite replaces the rock-forming silicates namely plagioclase, potassium felspar, and quartz. BSE (d) image exhibits the quartz grain altered by hydrothermal annite and then cut by calcite veins, which are associated with pyrite and sphalerite. Cross-polarized (e) and (f) transmitted light photomicrographs hydrothermal annite replaces the amphibole which shows intergrown phases with silicates in the matrix. (The scale bar is 200 µm for (a) in the bottom right).

Calcite that replaces plagioclase and potassium feldspar in both matrix and clast components is very fine-grained and anhedral. It is commonly observed as a patchy occurrence in the matrix (Figs. 3.15a and 3.16a). Less commonly, calcite is found penetrating the fragments of quartz and plagioclase (Figs. 3.16b-d). Calcite is often associated with hydrothermal annite (Figs. 3.16a, 3.15 (a), and (b)), and less commonly with chlorite (Fig. 3.17a). As shown in Figure 3.16, calcite alteration is directly in contact with graphite, suggesting the two may be syngenetic.

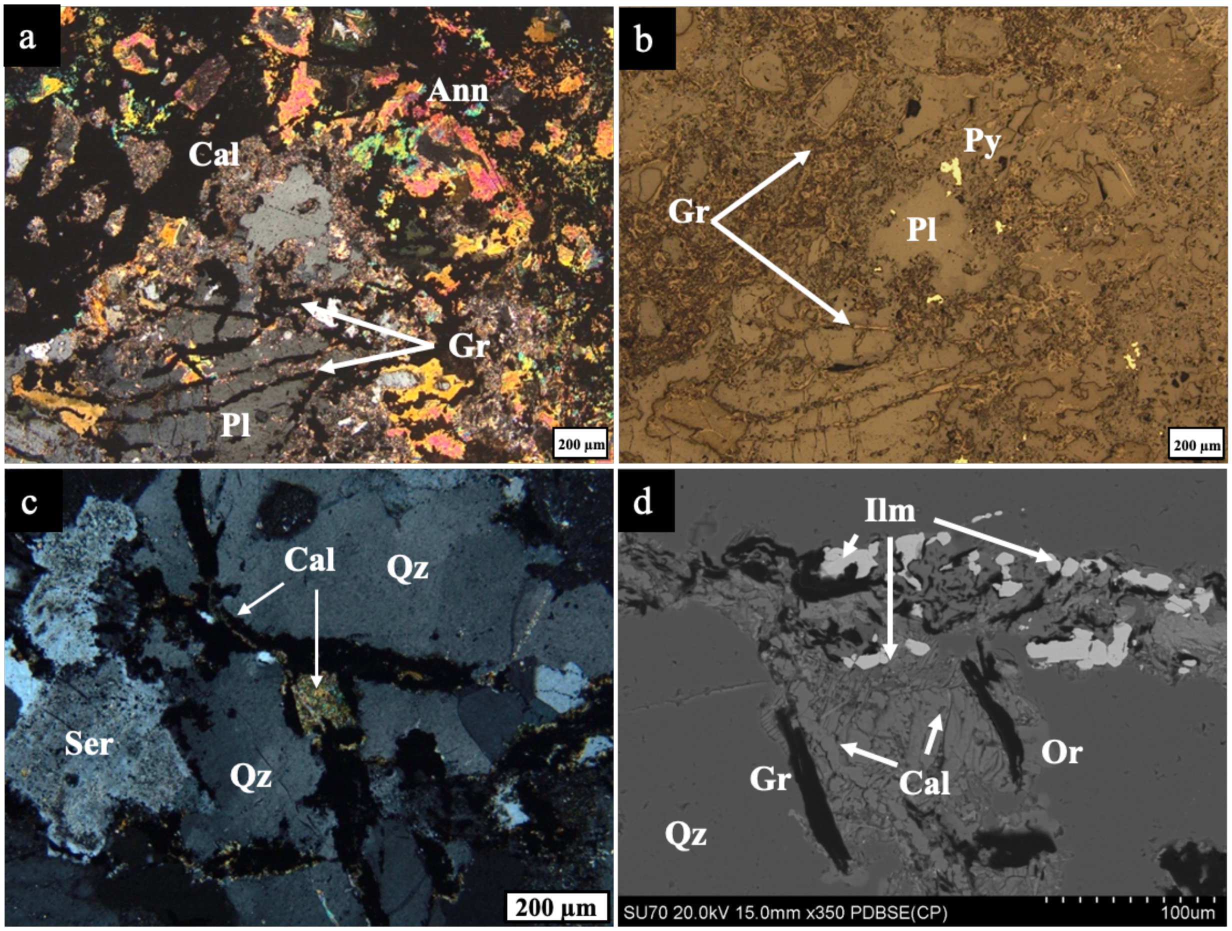

Figure 3.16 Photomicrographs and BSE images of key alteration assemblages. Cross-polarized (a) transmitted light and reflected (b) light photomicrographs show calcite, which is associated with hydrothermal annite, strongly alters the plagioclase in the matrix. Graphite is deposited at the fractures of plagioclase grain. Cross-polarized (c) transmitted light and BSE (d) image exhibits calcite, associated with graphite ilmenite, that occurs along the boundaries of quartz fragments. (The scale bars are 200 µm in the bottom right).

Replacive chlorite is typically very fine-grained, anhedral, and frequently displays a fibrous texture (Figs 3.17d and 3.18d). Another characteristic feature is its pale green colour under plane-polarized transmitted light. Chlorite occurs along the grain boundaries of silicate minerals that comprise the breccia fragments (Fig. 3.10a). Chlorite predominantly replaces annite and more rarely the plagioclase grains in the clast (Figs. 3.17 and 3.18). It is often associated with calcite (Figs. 3.17a and 3.19g), and it is seen adjacent to amphibole (Figs. 3.17 (a) and (e)), and pyrite (Figs. 3.17 (b)-(d) and 3.19c). Figure 3.19 provides another example of annite being altered by chlorite. Chlorite alteration is found adjacent to medium-grained pyrite and shows a distinct brownish colour. Furthermore, chlorite exhibits a fibrous texture upon SEM examination, albeit less prominently than in other occurrences (Fig. 3.19d). Based on the evidence from reflected light photomicrographs and BSE images, it is evident that chlorite is in direct contact with graphite, suggesting that they are likely for syngenetic.

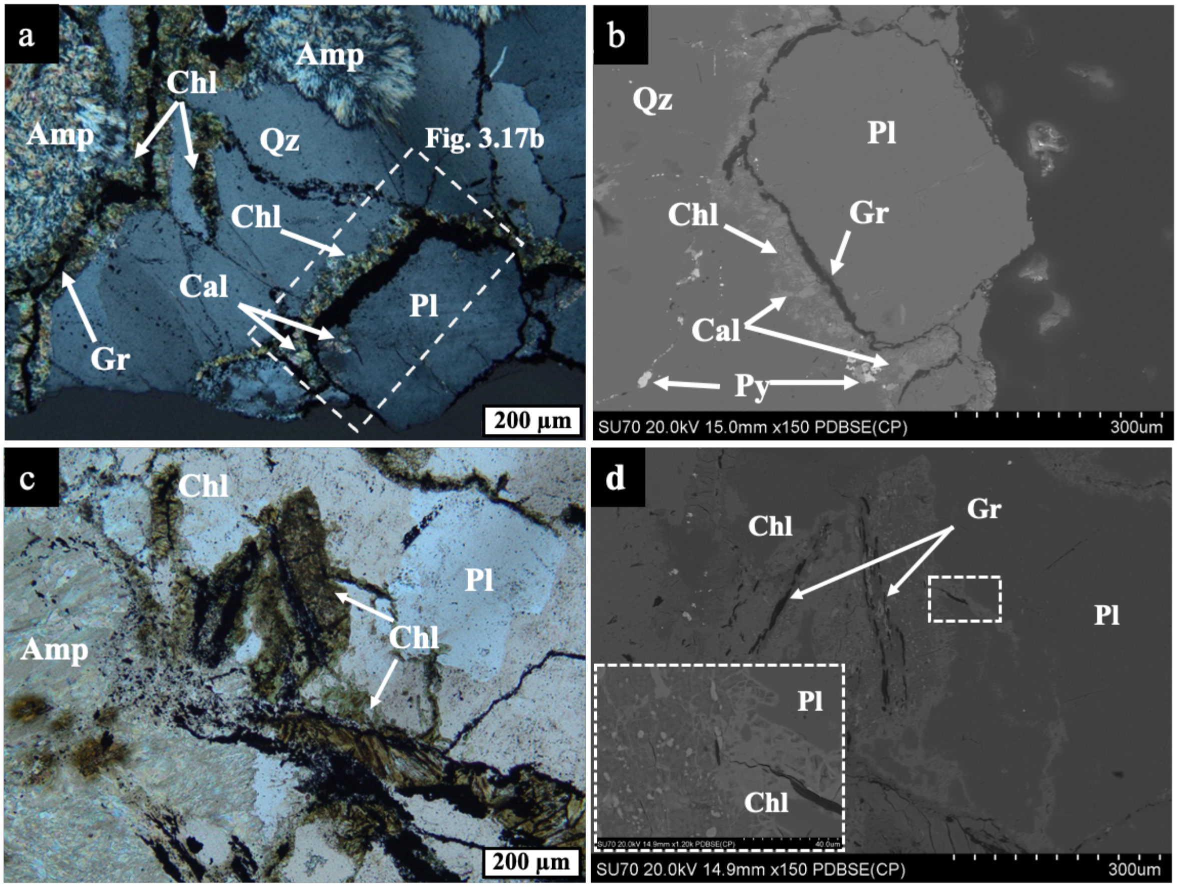

Figure 3.17 Photomicrographs and BSE images of chlorite alteration after plagioclase. Pale-green chlorite alteration which shows fibrous texture. Cross-polarized (a) transmitted light photomicrograph, and BSE (b)

images show chlorite and calcite replacing along the boundaries of plagioclase fragment and directly associated with graphite. Plane-polarized (c) transmitted light display annite replaced by chlorite, which is adjacent to amphibole. BSE (d) image shows chloritization of annite is intergrown with graphite.

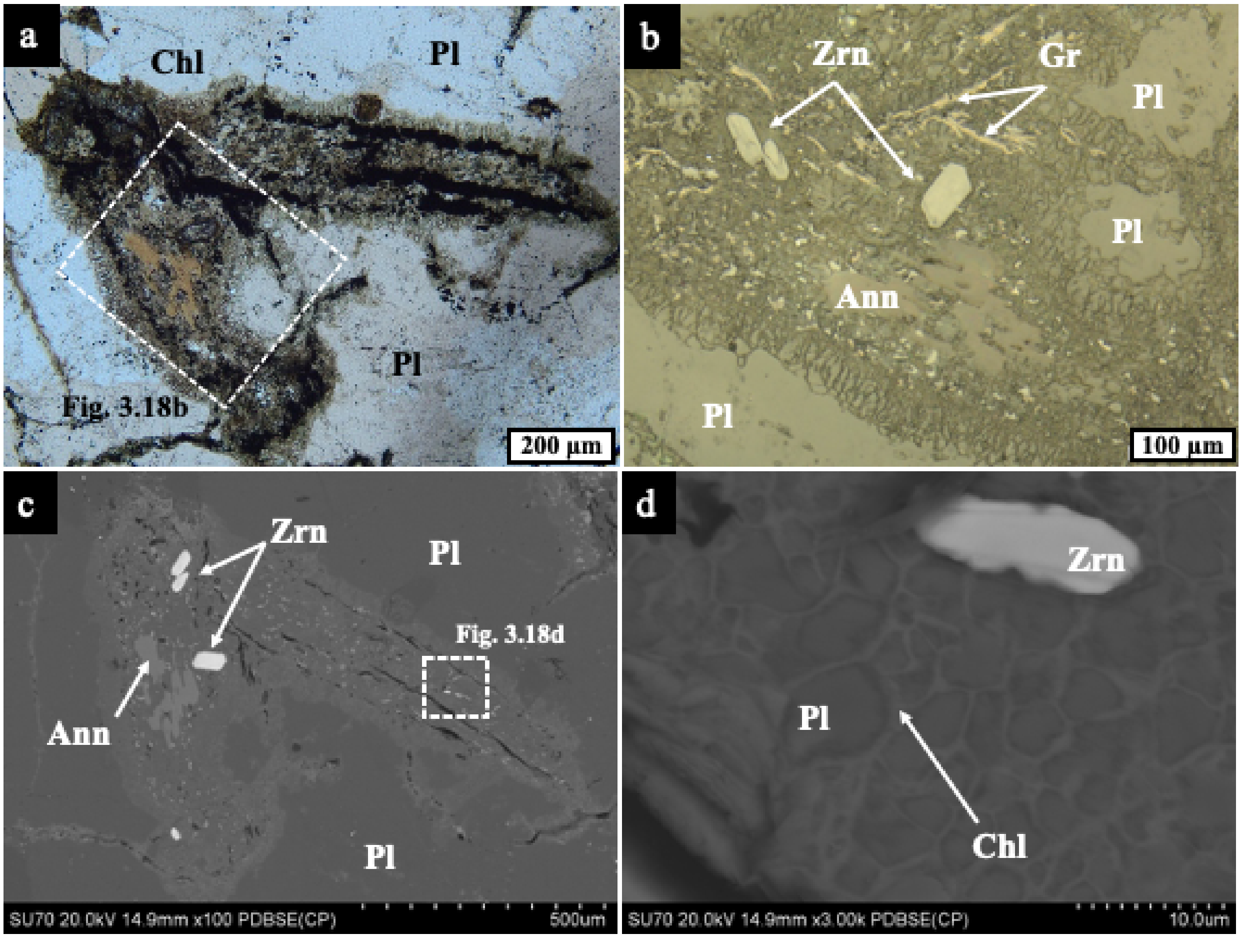

Figure 3.18 Photomicrographs and BSE images of replacive chlorite after annite. Plane-polarized (a) transmitted and reflected (b) light photomicrographs are showing replacive chlorite after annite. BSE (c) image exhibits chlorite is associated with graphite and contains euhedral zircon. (d) shows the fibrous texture. Plagioclase is rounded and dark and is surrounded by chlorite(lighter).

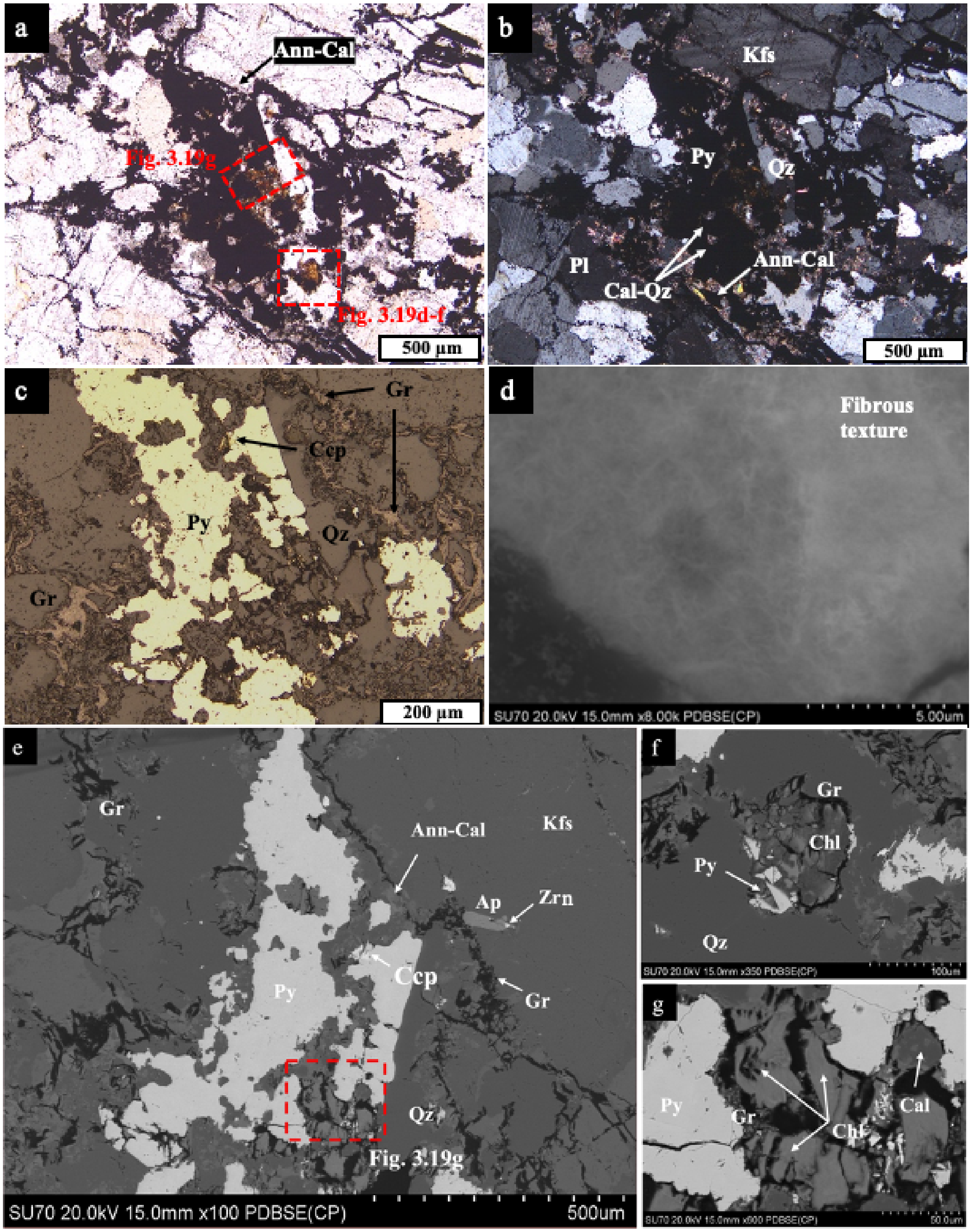

Figure 3.19 Photomicrographs and BSE images of replacive chlorite after annite. Plane polarized (a), cross-polarized transmitted (b), and reflected (c) light photomicrographs and BSE images (d-g) show the annite, which is found together with calcite and graphite along grain boundaries of silicates, has been altered by chlorite.

3.2 Mineral Chemistry

Mineral chemistry analyses were carried out on six samples (Zen2-Gp-21, Zen2-Gp-32, Zen26-Gp-09, Zen26-Gp-105, Zen27-Gp-63, Zen29-Gp-32) from the West pipe and two other samples (Zen10-Gp107 and Zen10-Gp-116) from the East pipe. Mineral compositions are used to define the alteration assemblages and their relationship with graphite. Phases analyzed include biotite, calcite, and chlorite. The complete mineral dataset is presented in Appendix l.

3.2.1 Biotite

The representative elemental compositions of biotite are shown in Table 3.3. The composition of biotite from the Albany deposit ranges from 34.13 to 44.66 wt. % SiO_2, 11.17 to 13.31 wt. % Al_2O_3, 8.16 to 16.59 wt. % MgO, 16.44 to 24.95 wt. % FeO, 9.42 to 10.34 wt. % K_2O (n=100). All the iron is assumed to be Fe^{2+} as stoichiometric calculation following Droop (1987) indicated no Fe^{3+}. Biotite from Zen2-Gp-21, Zen10-Gp-107, Zen26-Gp-09, Zen2-Gp-32, and Zen27-Gp-63 samples plot within the annite field, near the composition boundary with phlogopite in Figure 3.20. Zen26-Gp-105 is unique among the analyzed samples, as all analyses plot within the phlogopite field (Fig. 3.20). Some of the analyses from Zen 26-Gp-09 differ from other groups due to the alteration of amphibole by biotite (Fig. 3.22). The average composition of biotite from the Zen 26-Gp-09 is 49.8 wt% SiO_2, 11.5 wt% Al_2O_3, 11.7 wt% FeO, 12.0 wt% MgO, and 8.3wt% K_2O.

Table 3.3 Representative compositions of biotite from Albany deposit.

		Zen 10-GP-107 Ann	**Zen 26-GP-09 Ann**	**Zen 29-GP-32 Ann**	**Zen 26-GP-105 Phl**	**Zen 26-GP-105 Phl**	**Zen 26-GP-09 Ann**	**Zen 26-GP-09 Ann**
wt.%								
	SiO_2	39.60	41.16	41.52	45.66	42.72	52.20	55.78
	TiO_2	1.46	0.64	-	-	0.93	-	-
	Al_2O_3	12.13	11.08	12.13	11.62	11.94	10.33	9.78
	FeO	20.69	17.85	20.02	5.24	6.31	15.65	17.81
	MnO	0.51	-	-	-	-	-	-
	MgO	13.49	15,47	16.21	26.78	24.84	5.04	5.37
	CaO	-	-	-	-	-	-	-
	Li_2O	-	-	-	-	-	-	-
	Na_2O	-	-	-	-	-	-	-
	K_2O	9.38	10.23	0.97	10.63	10.71	7.39	7.46
	F	2.73	3.43	-	-	2.93	-	-
	Cl	0.53	0.37	-	0.13	-	-	-
		100.52	**100.95**	**99.85**	**100.06**	**100.38**	**90.61**	**96.20**
	-O≡F	1.15	1.44	-	-	1.23	-	-
	-O≡Cl	0.24	0.17	-	0.06	-	-	-
	Total	**99.13**	**99.34**	**99.85**	**100.00**	**99.15**	**90.61**	**96.20**
Structural formulae calculated on the basis of 22 oxygens								
a.p.f.u.								
	Si	5.94	6.09	6.02	6.16	5.98	7.76	7.84
	Ti	0.16	0.07	-	-	0.10	-	-
	Al	2.14	2.06	2.07	1.85	1.97	1.81	1.62
	Fe	2.60	2.21	2.43	0.59	0.74	1.95	2.09
	Mn	0.06	-	-	-	-	-	-
	Mg	3.02	3.41	3.50	5.39	5.19	1.12	1.13
	Ca	-	-	-	-	-	-	-
	Li	-	-	-	-	-	-	-
	Na	-	-	-	-	-	-	-
	K	1.79	1.93	1.84	1.83	1.91	1.40	1.34
	Total	**15.72**	**15.77**	**15.87**	**15.83**	**15.89**	**18.03**	**18.02**

Dash (-) - indicates values are b.d. limits

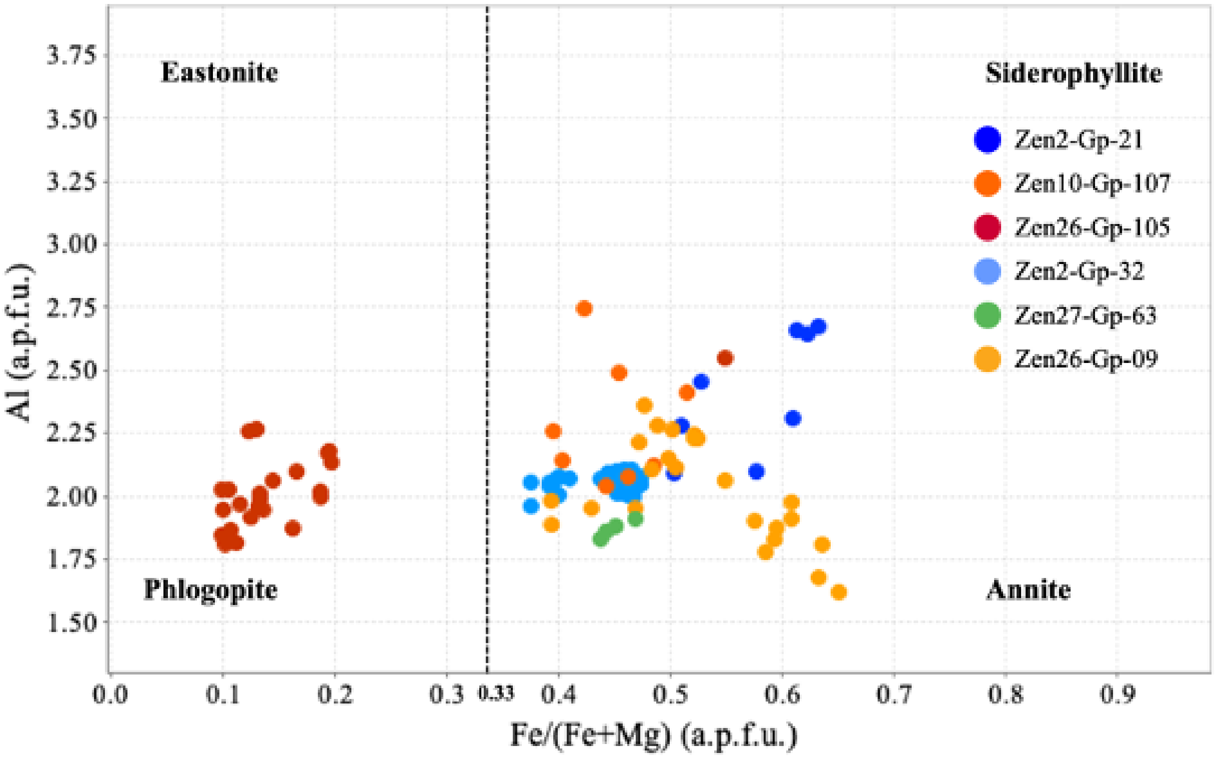

Figure 3.20 Biotite from Albany graphite deposit in the ASPE (Annite-Siderophyllite-Phlogopite-Eastonite) quadrilateral (Deer et al., 1992).

Based on textural characteristics, biotite was divided into four subgroups: igneous, metamorphic, hydrothermal, phlogopite, and Zen26 Gp-09. Variations of primary, re-equilibrated, and secondary biotite are illustrated using the ternary diagram TiO_2 – FeO – MgO (Fig. 3.21; after (Yamini et al., 2017). Igneous and metamorphic annite, which show predominantly euhedral subhedral morphology, are contained with igneous and metamorphic lithoclasts (Figs. 3.7 and 3.8). Igneous annite falls within the field of primary biotite. Metamorphic annite plots in the re-equilibrated biotite domain, with the analyses concentrated at the margin of the primary biotite domain. Hydrothermal annite exhibits a replacement texture and anhedral morphology in both clasts and matrix (Fig. 3.15a-c), and plots in the re-equilibrated biotite domain, except for a few biotite analyses that plot in the secondary biotite domain. Phlogopite, observed only in clasts, analyses are dominantly plotted in the re-equilibrated biotite domain. In the sample Zen26-Gp-09, replacive hydrothermal annite after amphibole is found intergrown with rock-forming silicates (e.g. quartz, plagioclase, and potassium feldspar) within the matrix (Figs 3.15 (e) and (f)).

Hydrothermal annite, very fine-grained and anhedral, from Zen26-G p-09 plots in the secondary biotite domain.

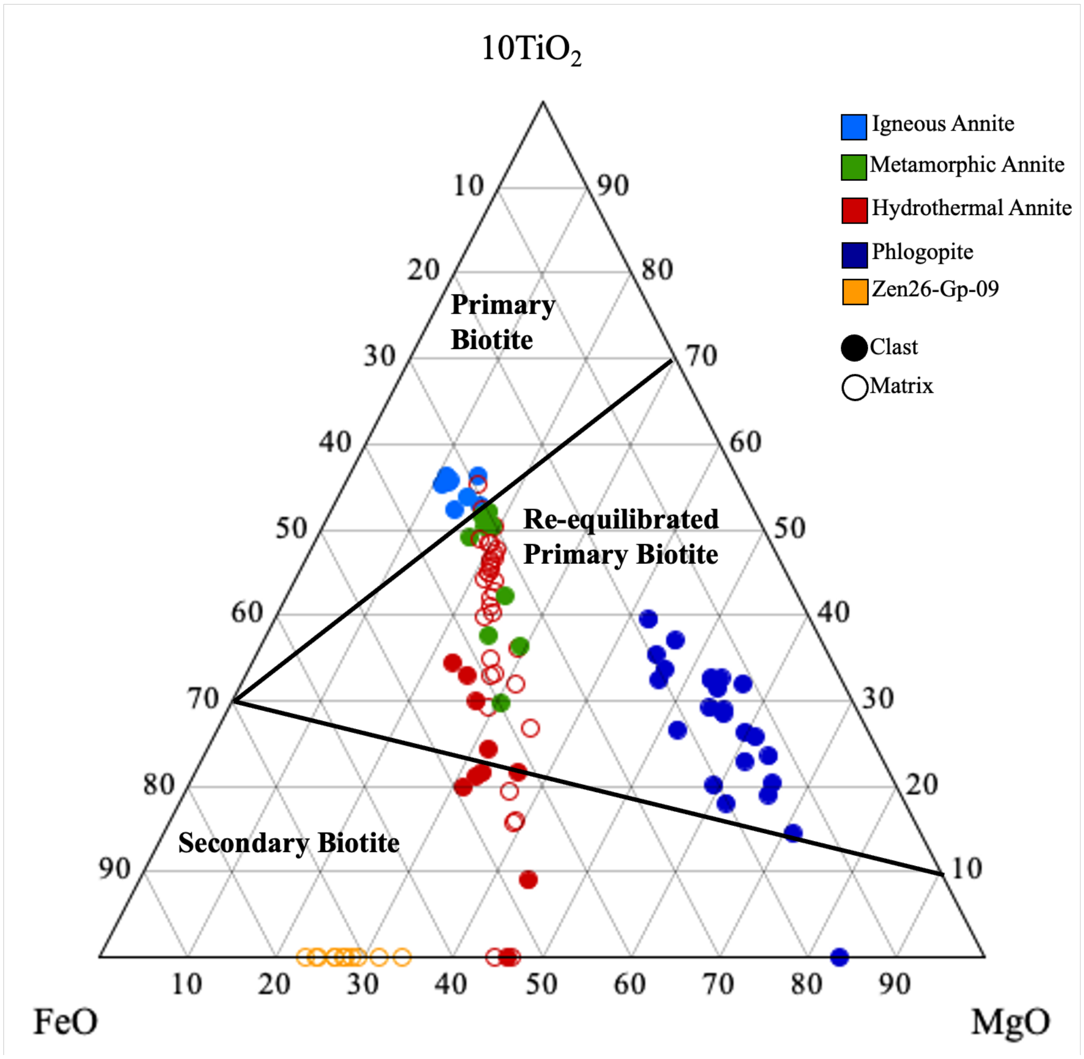

Figure 3.21 Albany Graphite deposit annite and phlogopite compositions plotted in the $10*TiO_2$-FeO-MgO ternary diagram (Yamini et al., 2017). Igneous annite n=9, Metamorphic annite n=10, Hydrothermal annite n=41, Phlogopite n= 24, Zen26-Gp-09 n=11

The relation between the contents of Fe versus Mg and Ti versus Mg in examined biotite is illustrated in Figure 3.22. Igneous annite has the highest amount of Fe (2.66–3.28 a.p.f.u.) and Ti (0.41-0.49 a.p.f.u.), coupled with lower Mg (1.91–2.62 a.p.f.u.) in comparison to other groups. Metamorphic annite has slightly lower Fe (ranges from 2.13 to 2.82 a.p.f.u.) and Ti (ranges from 0.15 to 0.40 a.p.f.u.) than igneous annite (Fig. 3.22). Hydrothermal annite in the clast and matrix differ in the concentration of Ti present. The Ti content of hydrothermal annite in the matrix is more variable and < 0.47 a.p.f.u., the clast-hosted hydrothermal annite is typically <0.20 a.p.f.u. Phlogopite grains are only observed in the clast, while annite grains are both in the matrix and clast. Phlogopite has higher Mg (4.48–5.39 a.p.f.u.) and lower Fe (0.57–1.11 a.p.f.u.) than the annite groups. However, the composition of Si in phlogopite and annite does not show significant variation, ranging from 5.3 to 6.3 (a.p.f.u.). The analysis of the hydrothermal annite taken from sample Zen26-Gp-09 is accepted as semi-quantitative due to the low total oxide values (ranging from 90-96 wt.%). The compositions of this annite, which alter from the amphibole in the matrix, are not ideal because amphibole is finely intergrown with other silicate phases. While these annite grains do not have Ti, they show a high amount of Fe (average 1.74 a.p.f.u.) and low Mg (around 1.17 a.p.f.u.).

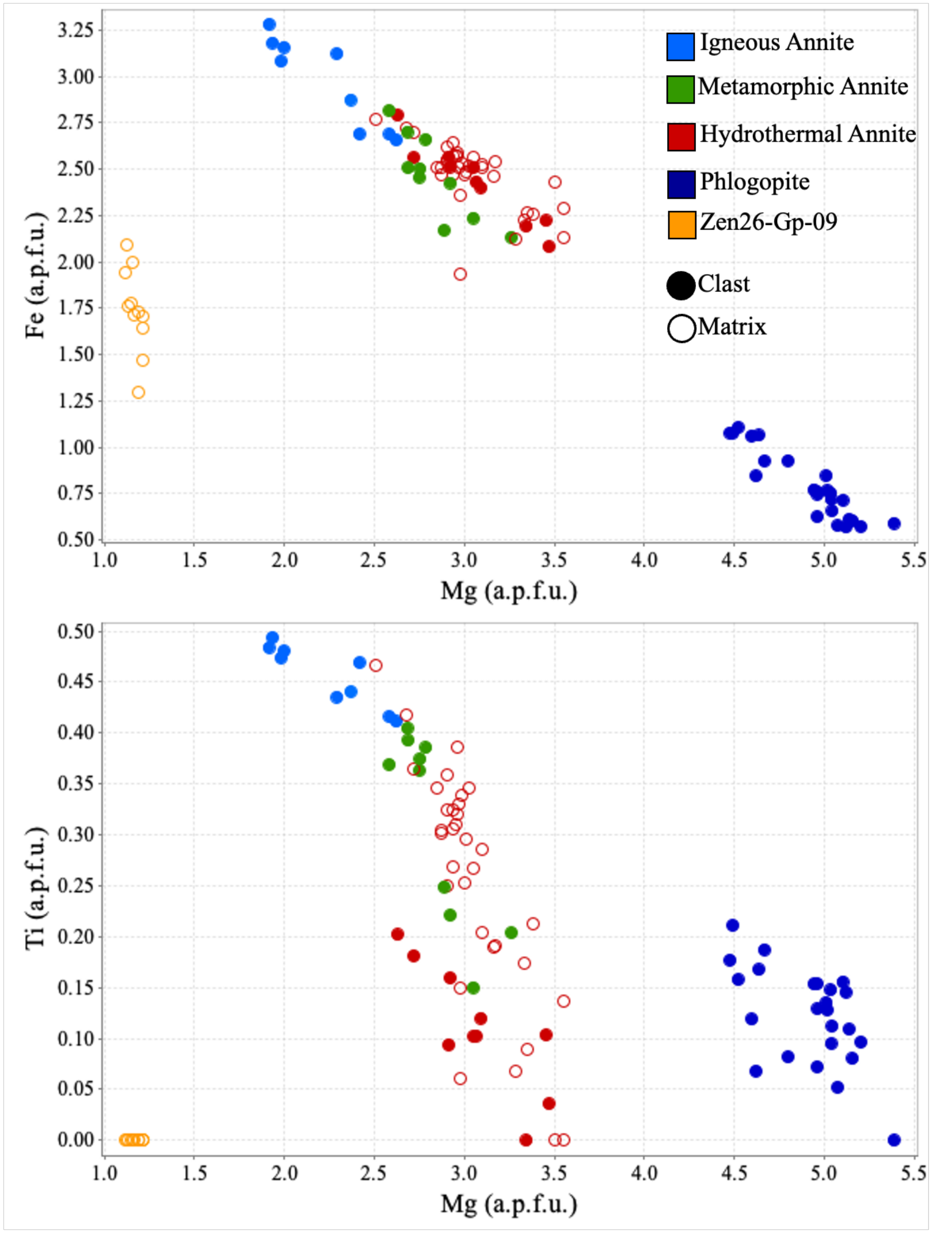

Figure 3.22 Diagrams of Fe vs. Mg and Ti vs. Mg of annite and phlogopite in the Albany graphite deposit in atoms per formula unit (a.p.f.u.).

The relationship between graphite and the examined biotite is shown in the ternary diagram (Fig. 3.23). Igneous annite, which shows a dark brown color, is not in direct contact with graphite (Fig. 3.23a). Most of the metamorphic annite, which shows a green-brown color, is rarely in contact with graphite. Graphite flakes were observed along the cleave plains of some of the metamorphic annite grains (Fig. 3.23b). Hydrothermal annite, which shows a pale green-light brown color, is in highly proximal contact with graphite (Fig. 3.23c). Phlogopite grains were observed directly in contact with graphite. Generally, graphite is seen to be deposited parallel to the cleavage of the very fine-grain phlogopite grain (3.7e and f). Hydrothermal annite grains from Zen26-Gp-09, which are in the secondary domain, are directly in contact with graphite (Fig. 3.15 (e) and (f)).

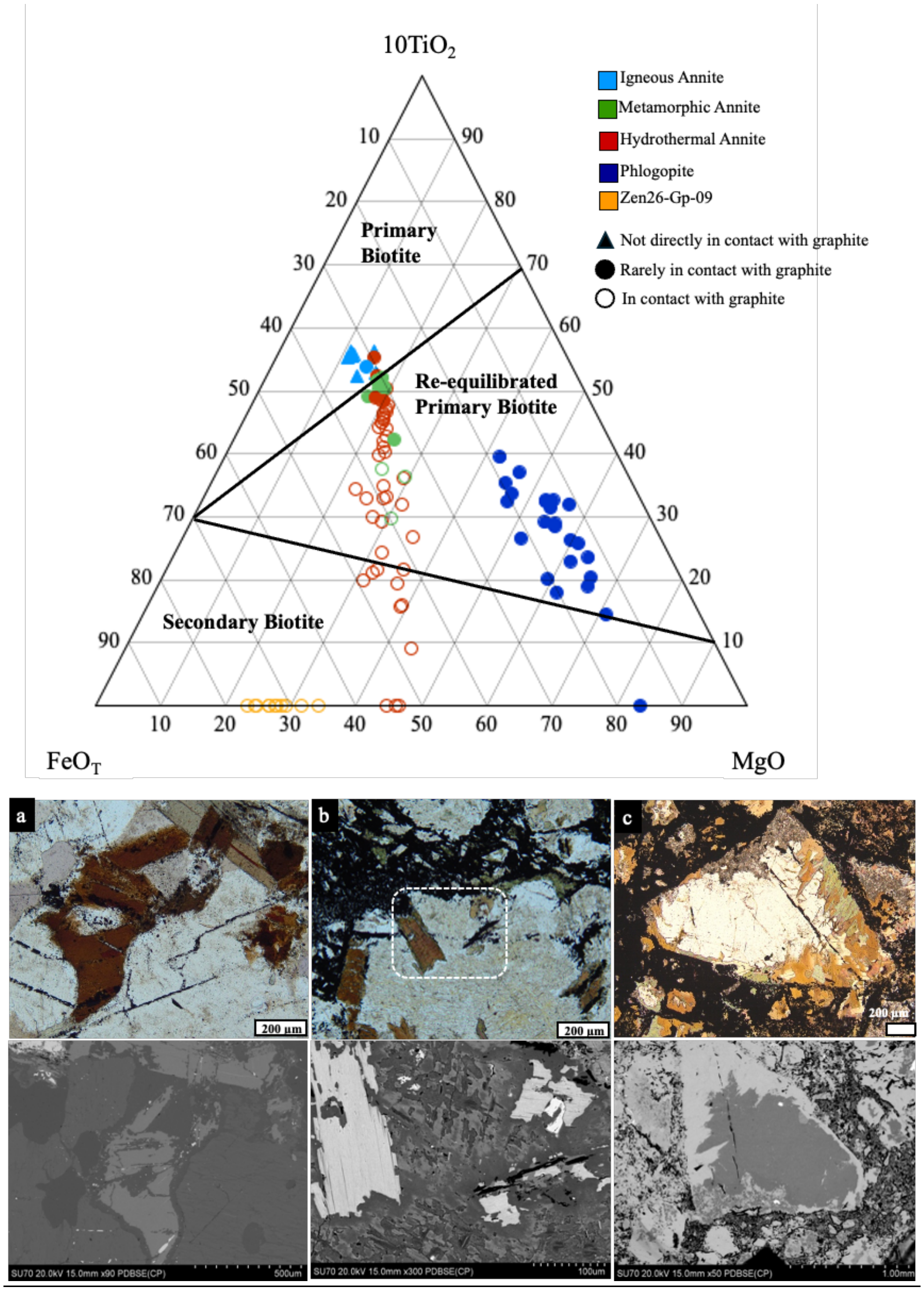

Figure 3.23 Ternary diagram and photomicrographs exhibit varying degrees of biotite-graphite contact. Representative transmitted light photomicrographs and BSE images show (a) igneous biotite not in contact with graphite, (b) metamorphic biotite is rarely in direct contact with graphite, and (c) hydrothermal biotite is directly in contact with graphite. (The scales are 200 µm for (a), (b), and (c)).

3.2.2 Carbonates

Carbonate minerals were observed in seven samples, two from the East pipe (Zen10-Gp-107 and Zen10-Gp-116) and five from the West pipe (Zen-2-Gp-21, Zen-2-Gp-32, Zen-26-Gp-105, Zen-27-Gp-63, and Zen-29-Gp-32). The Albany graphite deposit contains both calcite and dolomite, with the former being predominant (Fig. 3.24). West (2016) studied the supergene alterations of the Albany deposit nothing both continuous and discontinuous carbonate veins and isolated masses were identified in the weathering profile. In this study, the calcite examined is below the weathering profile, so is related to supergene alteration. However, dolomite is closer to the paleosurface and, therefore, may be weakly affected by supergene fluids, and thus, dolomite might be related to weathering.

Representative compositions of calcite are presented in Table 3.4, with structural formulas calculated based on six oxygen atoms. Carbonate chemistry is plotted on a Ca – Mg – (Fe + Mn) ternary diagram (Fig. 3.24). Calcite compositions do not vary greatly: 43.70 to 53.94 wt. % CaO, < 1.86 wt. % MgO, < 5.76 wt. % MnO and < 4.45 wt. % FeO. Calcite that occurs as a breakdown of plagioclase is observed as isolated grains in clasts and veins, whereas replacive calcite is observed in the matrix and along the grain boundaries in clasts. Calcite veins are seen to cross-cut aggregates of clast and matrix. Also, it is rarely observed to cross-cut annite-rimmed quartz grains in the matrix (3.15(b) and (d)). Calcite alters the rock-forming silicates along the grain boundaries in the clasts (Fig. 3.17a), while it shows rim replacement and filling the fractures of plagioclase and potassium feldspar crystals in the matrix (Figs. 3.15a and 3.16a).

Graphite is rarely associated with isolated calcite grains (Fig. 3.14) and with calcite veins (Figs. 3.13(a)- (c)), which for the latter graphite is situated along some of the vein wall (Figs. 3.7d and 3.13d). However, calcite alteration within the matrix and clast are frequently associated with graphite (Fig. 3.15). The substitution of Fe, Mn, and Mg for Ca is shown in Figure 3.25, where calcite compositions have a strong negative correlation (R=-1).

Table 3.4. Representative composition of calcite.

		Zen 2-GP-32	**Zen 2-GP-32**	**Zen 2-GP-32**	**Zen 10-GP-107**	**Zen 10-GP-107**	**Zen 2-GP-21**	**Zen 2-GP-21**
Wt.%								
	$FeCO_3$	1.77	2.00	1.90	1.95	2.48	-	0.64
	$MnCO_3$	0.68	-	0.58	0.81	5.95	2.77	1.25
	$MgCO_3$	0.92	3.85	-	0.71	1.46	-	-
	$CaCO_3$	91.75	91.59	96.08	89.75	90.00	91.59	95.17
	$SrCO_3$	-	-	-	-	-	-	-
	$BaCO_3$	-	-	-	-	-	-	-
	Total	**95.12**	**97.43**	**98.57**	**93.22**	**99.89**	**94.36**	**97.06**
Structural formulae calculated on the basis of 6 oxygens								
a.p.f.u.								
	Fe	0.10	0.11	0.10	0.11	0.13	-	0.03
	Mn	0.04	-	0.03	0.05	0.31	0.15	0.07
	Mg	0.07	0.28	-	0.05	0.11	-	-
	Ca	5.80	5.61	5.87	5.79	5.45	5.85	5.90
	Sr	-	-	-	-	-	-	-
	Ba	-	-	-	-	-	-	-
	Total	**6.00**	**6.00**	**6.00**	**6.00**	**6.00**	**6.00**	**6.00**
Dash (-) - indicates values are b.d. limits								

The chemical composition of dolomite, which is rare, is given in Table 3.5, with structural formulas calculated based on six oxygen atoms. Dolomite displays minimal compositional variability, with compositions ranging from 28.10 to 30.50 wt. % CaO, 13.08 to 16.19 wt. % MgO, 1.03 to 2.42 wt. % MnO and 5.38 to 7.51 wt. % FeO. Dolomite compositions are plotted in the ternary diagram Ca – Mg – (Fe + Mn) (Fig. 3.24).

Table. 3.5 Representative composition of dolomite.

		Zen 29-GP-32	**Zen 29-GP-32**	**Zen 29-GP-32**	**Zen 29-GP-32**
Wt.%					
	$FeCO_3$	11.51	10.13	10.16	9.90
	$MnCO_3$	1.85	2.01	2.46	2.30
	$MgCO_3$	32.80	31.95	33.70	33.77
	$CaCO_3$	52.06	52.09	54.43	52.65
	$SrCO_3$	-	-	-	-
	$BaCO_3$	-	-	-	-
	Total	**98.22**	**96.17**	**100.75**	**98.61**
Structural formulae calculated on the basis of 6 oxygens					
a.p.f.u.					
	Fe	0.58	0.11	0.10	0.11
	Mn	0.09	-	0.03	0.05
	Mg	2.28	0.28	-	0.05
	Ca	3.05	5.61	5.87	5.79
	Sr	-	-	-	-
	Ba	-	-	-	-
	Total	**6.00**	**6.00**	**6.00**	**6.00**
Dash (-) - indicates values are b.d. limits					

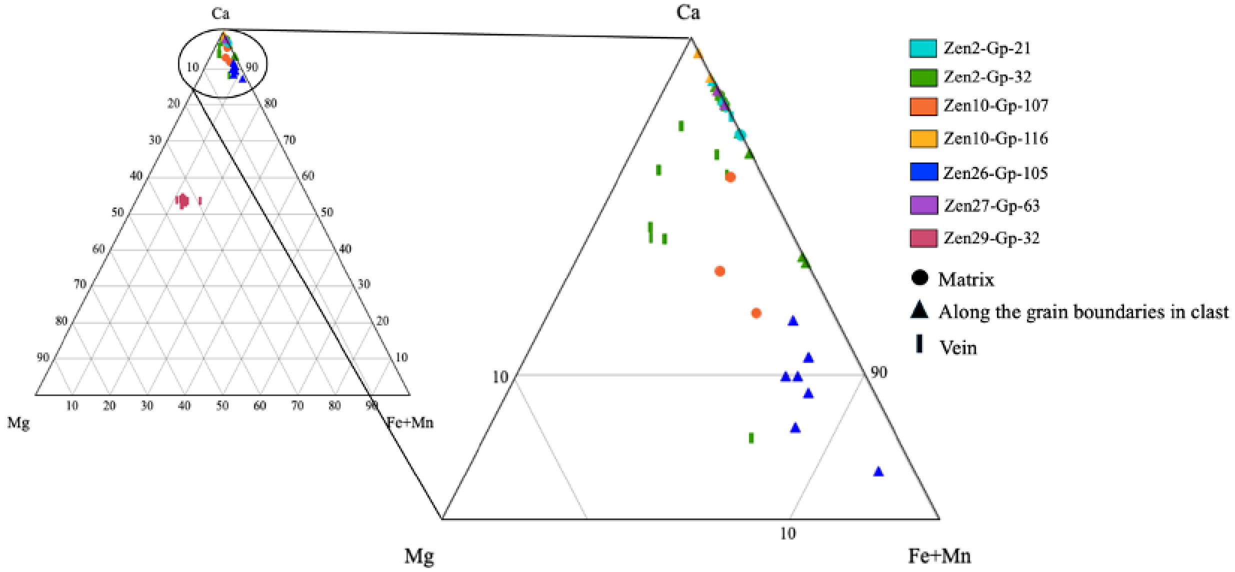

Figure 3.24 Ternary diagram Ca – Mg – (Fe + Mn) with calcite and dolomite from the Albany graphite deposit.

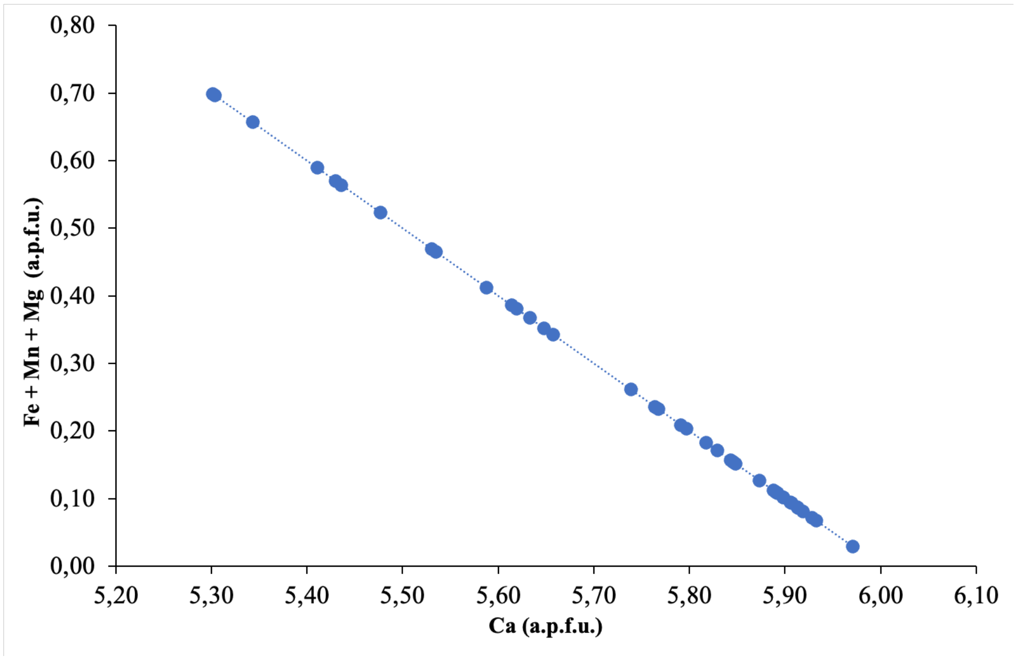

Figure 3.25 Bivariate plots of the calcite compositions from the Albany graphite deposit; Fe + Mn + Mg (a.p.f.u.) versus Ca (a.p.f.u.) showing a strong negative correlation (R = -1). Pearson's Product correlation coefficients (R) have been calculated using all samples (n=54).

While calcite has been observed to frequently be an alteration product after plagioclase and potassium feldspar, it can also be found to be adjacent to chlorite and biotite. The chemistry of calcite varies in response to the phase with which it is associated. Figure 3.26 exhibits the change in the chemical composition of calcite, according to the minerals it is associated with. The bivariate plot of Fe+Mn (a.p.f.u.) versus Ca (a.p.f.u.) shows that while Ca increases, Fe+Mn composition in the calcite decreases. Calcite, which is adjacent to the chlorite, has the lowest Ca contents (i.e., in the range of 5.30-5.54 a.p.f.u), but the highest Fe+Mn contents (up to 0.63 a.p.f.u.). However, where calcite is associated with biotite, it has the highest Ca, approximately 5.90 a.p.f.u, and the lowest Fe+Mn, less than 0.15 a.p.f.u.

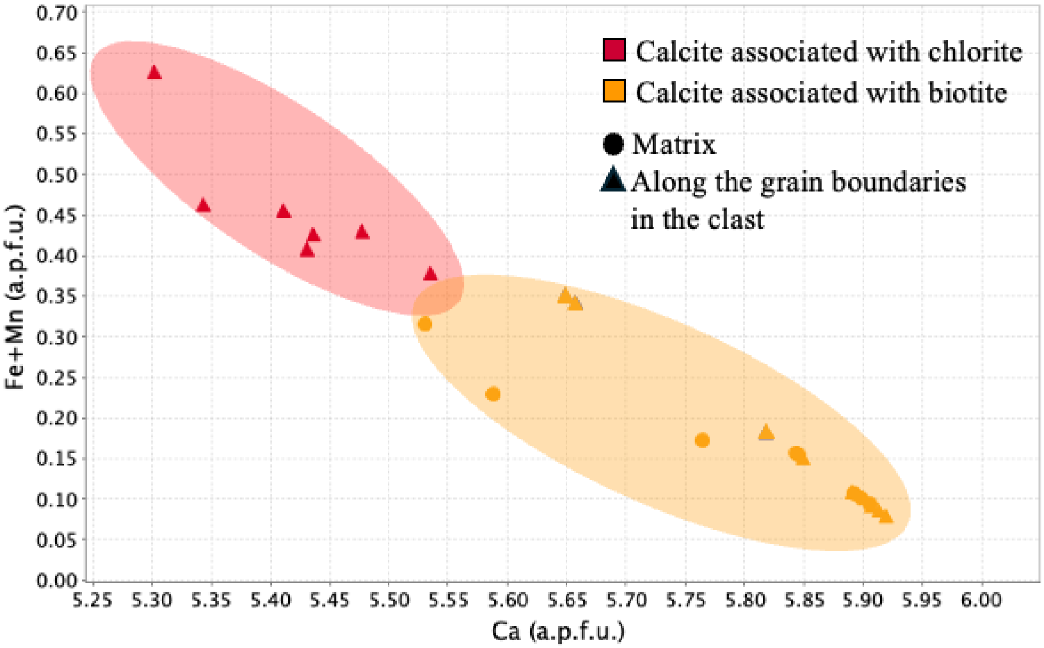

Figure 3.26 Bivariate plot illustrates the inverse relationship between the Ca (a.p.f.u.) content and the Fe+Mn (a.p.f.u.) content in calcite. Calcite is evaluated, which is found to be associated with chlorite and biotite, based on their occurrence in the clast or matrix.

3.2.3 Chlorite

Three textural types of chlorite-group species are observed in the Albany graphite deposit: (1) replacive chlorite, which exhibits fibrous textured after secondary (hydrothermal) annite (Fig. 3.19); (2) replacive chlorite, pale-green and fibrous, after primary (igneous) annite and plagioclase

(Figs. 3.17 and 3.18); (3) non-replacive chlorite, which occurs as pale-green small veinlets hosted in dolomite (Figs. 3.14). Chlorite compositions are presented in Table 3.6, with structural formulas calculated based on twenty-eight atoms of oxygen. The SiO_2 content varies from 26.78 to 53.71 wt. %, with an average of 37.19 wt. %, the Al_2O_3 content ranges from 5.59 wt. % to 16.49 wt. % with an average of 10.01 wt. %, the FeO content ranges between 13.83 to 40.18 wt. %, with an average of 27.29 wt.%, and the MgO content ranges from 1.75 to 17.58 wt. %, with an average of 8.83 wt. %.

Compared to replacive chlorite varieties (1) and (2), the compositions of the (3) non-replacive chlorite group (indicated as the pink line in Fig. 3.27 and the pink area in Fig. 3.28) show low Fe and slightly elevated Mg. The compositions of the (1) group (indicated as the blue line in Fig. 3.27 and the blue area in Fig. 3.28) are not fully quantitative as there is likely Fe contamination from the adjacent pyrite (Fig 3.19). Thus, Fe may be abnormally high, Al may be underestimated, Si is slightly overestimated, and S is in chlorite content (last column in Table 3.6). Zane and Weiss (1998) introduced a classification diagram based on the chemical composition and structure of chlorite. According to the Al–Fe–Mg compositional diagram (Fig. 3.28), all analyzed chlorite plots within the chamosite (Fe-Chlorite) in the trioctahedral-type chlorite field.

Figure 3.28 shows the relationship between chlorite composition and the association with graphite. Replacive chlorites are often directly in contact with graphite (Fig. 3.28a), especially when it forms intergrowths with graphite along the boundaries of quartz and plagioclase fragments (Fig. 3.28b). Non-replacive chlorite is not associated with graphite (Fig. 2.38c).

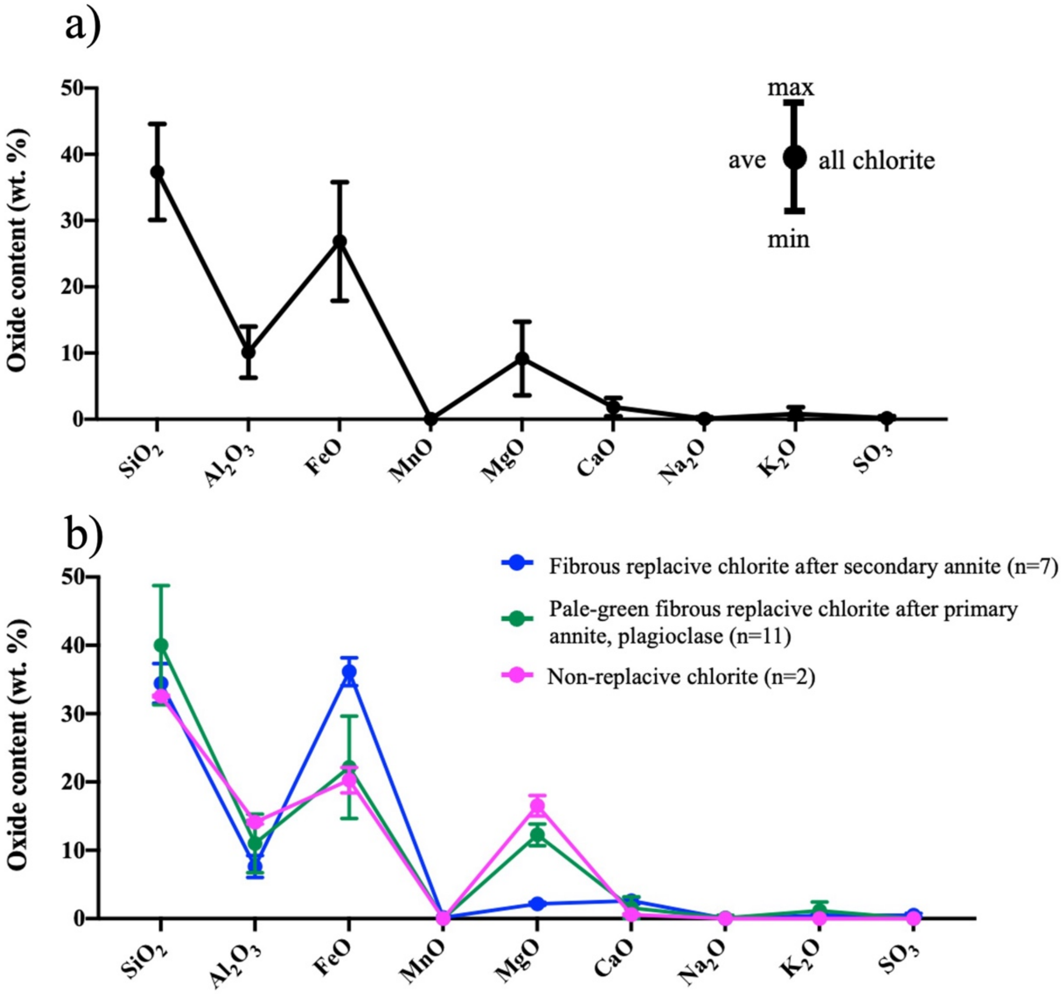

Figure 3.27 (a) Maximum, minimum, and average oxide content of all chlorite analyses. (b) Maximum, minimum, and average oxide content of three types of chlorite-group species based on their texture in the Albany graphite deposit

Table 3.6 Representative compositions of chlorite.

		Zen 26-GP-09	Zen 29-GP-32	Zen 29-GP-32	Zen 10-GP-116	Zen 26-GP-105	Zen 2-GP-32	Zen 2-GP-32
Wt.%								
	SiO_2	26.78	32.67	32.46	29.84	34.50	38.14	30.85
	Al_2O_3	15.97	14.34	13.92	15.11	12.40	6.61	10.91
	FeO	21.58	21.58	18.96	30.87	27.59	34.56	40.18
	MnO	-	-	-	-	-	0.53	-
	MgO	14.94	15.47	17.58	12.26	13.08	2.07	2.37
	CaO	0.34	0.68	0.49	0.39	0.63	3.04	1.69
	K_2O	0.32	-	-	-	0.16	0.36	0.24
	Na_2O	-	-	-	-	-	-	-
	Cr_2O_3	-	-	-	-	-	-	-
	SO_3	-	-	-	-	-	-	0.54
	Total	**88.54**	**84.74**	**83.41**	**88.47**	**88.36**	**85.31**	**86.78**
Structural formulae calculated on the basis of 28 oxygens								
a.p.f.u.								
	Si	5.77	6.90	6.88	6.38	7.19	8.62	7.12
	Al	4.06	3.57	3.48	3.81	3.05	1.76	2.97
	Fe	5.44	3.81	3.36	5.52	4.81	6.53	7.76
	Mn	-	-	-	-	-	0.10	-
	Mg	4.80	4.87	5.55	3.91	4.07	0.70	0.82
	Ca	0.08	0.15	0.11	0.09	0.14	0.74	0.42
	K	0.09	-	-	-	0.04	0.10	0.07
	Na	-	-	-	-	-	-	-
	Cr	-	-	-	-	-	-	-
	S	-	-	-	-	-	-	0.09
	Total	**20.24**	**19.31**	**19.38**	**19.71**	**19.30**	**18.55**	**19.24**

Dash (-) - indicates values are b.d. limits

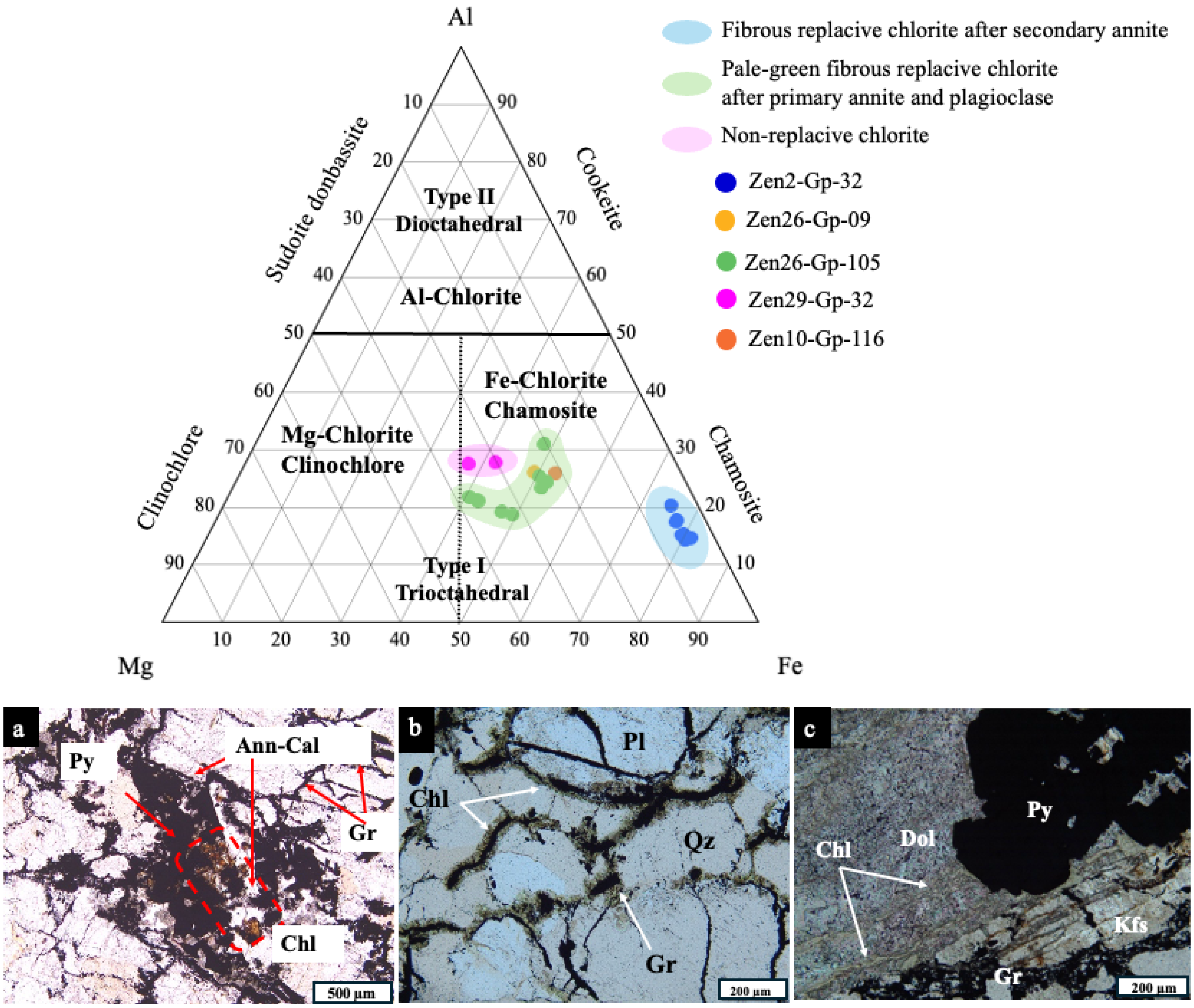

Figure 3.28 Compositions of chlorite from Albany are plotted in the Al – Fe – Mg ternary diagram, indicating the compositions fall into the chamosite field (Zane, A. & Weiss, A., 1998). Representative photomicrograph of chlorite groups; (a) represents the fibrous chlorite replacing secondary annite, which is adjacent to the pyrite (blue area) (b) represents pale-green fibrous chlorite, which is associated with graphite, migrating along the boundaries of quartz and plagioclase fragments (green area). (c) non-replacive chlorite hosted in dolomite (pink area).

Chapter 4. DISCUSSION

Through the integration of petrographic, SEM observations, and mineral chemistry, differentiation among brecciated host rock-forming minerals and phases associated with alteration events was investigated to assess the relationship between alteration processes and graphitization. Key alteration minerals that were identified and deemed critical to the crystallization of graphite are hydrothermal annite, chamosite, and calcite.

4.1. Paragenesis

Figure 4.1 is the paragenetic sequence for the Albany graphite deposit that was derived from the petrographic and SEM observations. The main mineral-forming events are delineated: host rock, pre-graphitization alteration, graphitization, and post-graphitization alteration. The host rock stage represents the formation of the primary mineral phases that form the brecciated host rock. Phases that form during this stage include plagioclase, potassium feldspar, quartz, igneous annite, metamorphic annite, phlogopite, amphibole, and pyroxene (Figs. 3.5 and 3.6). Amphibole and pyroxene are euhedral to subhedral and interstitial to quartz, plagioclase, and potassium feldspar (Fig. 3.6(c) and (d)). In addition, Fe-Ti oxides (ilmenite and magnetite and subhedral to euhedral accessory minerals; apatite, zircon, and chromite are in the host rocks (Figs. 3.7e and f).

Biotite paragenesis is more complicated as it occurs as both an alteration phase (pre-graphitization alteration) but also an important rock-forming mineral (host rock phase) present in igneous and metamorphic fragments that comprise the framework of the graphite-bearing breccias. From the mineral chemical analyses, two compositional groups of biotite are identified, annite and phlogopite. Phlogopite, subhedral and very fine to fine-grained, is observed as a rock-forming phase in one clast lithology in the sample (Zen26-Gp-105). Backscatter electron images (Fig. 3.7f) along with the SEM-EDS compositions of phlogopite and other phases (e.g., chromite and apatite; Appendix 8) indicate a mineral assemble that suggests the fragments are brecciated lamprophyre. Three types of annites are assigned based on petrographic observations. Due to its igneous texture, one of the types of annite is referred to as igneous annite. The other one, elongated annite schist fragments, is referred to as metamorphic annite. Both igneous and metamorphic annite occur in the clast and show euhedral to subhedral morphology (Figs. 3.7 and 3.8). Anhedral and dominantly very fine-grained. annite that exhibit a replacement texture in both clasts and matrix is referred to as hydrothermal annite.

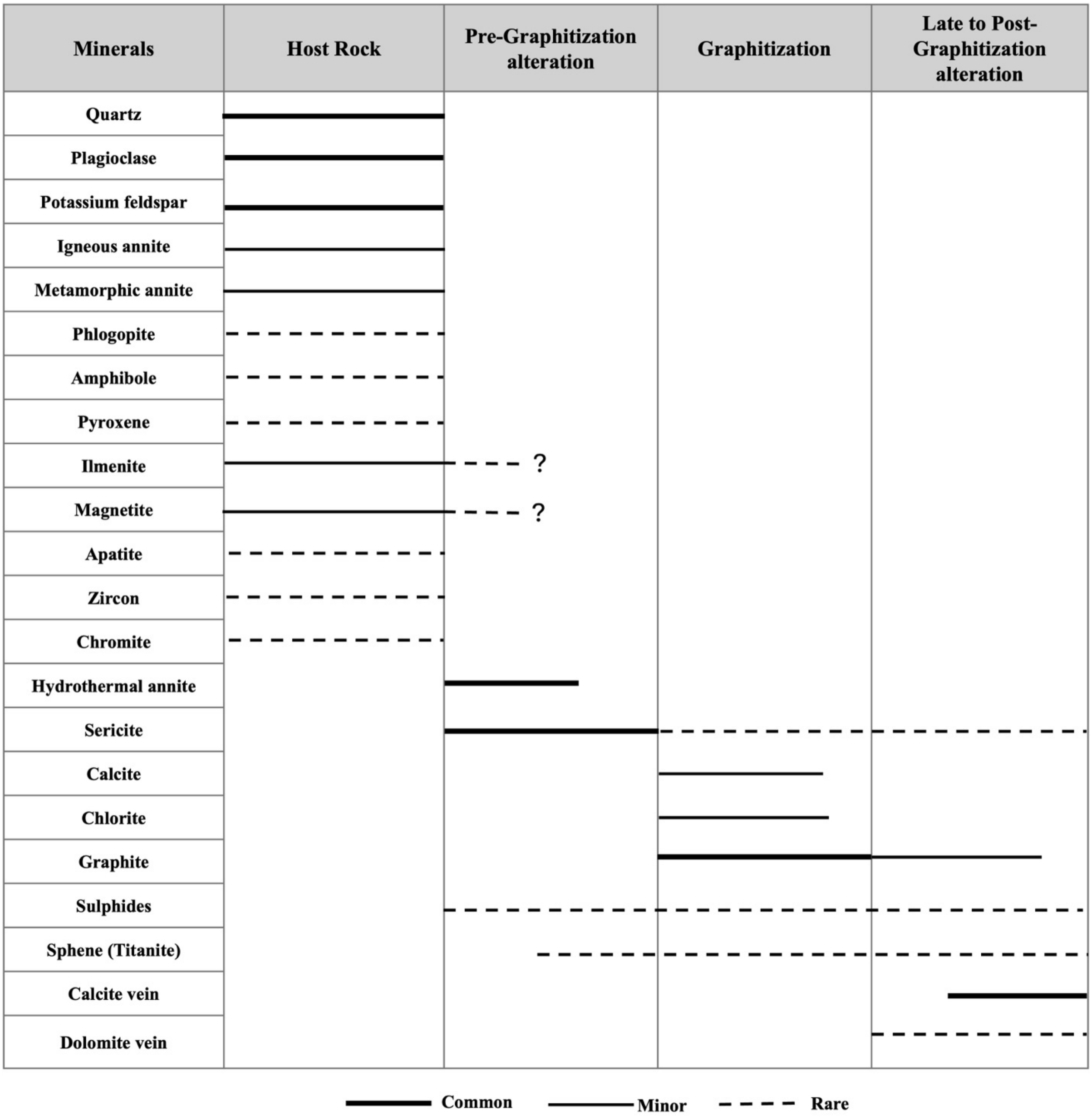

Figure 4.1 Paragenetic sequence of the Albany graphite deposit is divided into four stages: host rock, pre-graphitization alterations, graphitization, and post-graphitization alterations. Owing to breccias being heterolithic, the paragenesis primary host rock mineral phases were not assessed. The thickness of the horizontal bars is related to the relative abundance of the mineral. Sulfide minerals include pyrite and along with subordinate chalcopyrite, and sphalerite.

Pre-graphitization alteration stage is characterized by sericite and hydrothermal annite (potassic alteration). Sericitation of plagioclase and potassium feldspar is commonly observed and typically occurs as disseminated crystals in the mineralization stage (Fig. 3.6a). Graphite commonly is distributed along the boundaries of the sericitized feldspar grains in the matrix during the mineralization stage (Fig. 3.11b), which indicates that sericitization might have happened before graphite mineralization.

Hydrothermal annite is often seen replacing plagioclase, potassium feldspar, and rarely amphibole (Fig. 3.15). The replacement of these minerals by hydrothermal annite occurs at their rim, partially or completely (Figs. 3.11(c)-(d) and 3.15). Replacive hydrothermal annite is found to be associated with sericite, calcite, and graphite. Igneous annite is not in direct contact with graphite, while metamorphic annite is rarely found to be in contact with graphite (Figs. 3.23a and b). In contrast, hydrothermal annite is frequently observed in direct contact with graphite within the matrix (Fig. 3.23c). The fact that graphite is seen along the cleavage planes of annite in the matrix suggests that annite is a precursor alteration to graphitization (Fig. 3.8(b) and (d)).

Average FeO contents of the igneous, metamorphic, and hydrothermal annite are 23.07, 19.66, and 15.23 wt.%, respectively, while MgO contents are 9.75, 12.71, and 15.67 wt.%, respectively. Primary biotite (igneous and metamorphic) is enriched in Fe, while secondary biotite (hydrothermal) is rich in Mg (see Chapter 3, Figure 3.22), which can be explained by the fact that the alteration processes lead to either iron loss or magnesium enrichment (Sun et al., 2022). The TiO_2 content decreases from the igneous to metamorphic to hydrothermal annite (average 3.94, 2.77, and 1.57 wt.%, respectively), which shows consistency with literature (e.g., Parsapoor et al., 2015; Ani et al., 2022). Igneous and metamorphic annite ranges from dark brown to green-brown, while hydrothermal annite exhibits pale green-light brown (Fig. 3.23). Parsapoor (2015) explains that the chemical composition of biotite affects its pleochroism, and hydrothermal alteration of biotite causes a reduction in TiO_2. The trend of the TiO_2 content of hydrothermal annite in the Albany deposit is consistent with Parsapoor (2015). In addition, annite in the Albany deposit is distinguished by varying in its pleochroic scheme, ranging from green (Fe-rich) to red-brown (Ti-rich).

The graphitization stage is characterized by propylitic alteration assemblage, consisting of calcite and chamosite, and is interpreted to be a contributing factor to graphite crystallization. Calcite is found to fill intergranular open space in the matrix (Figs. 3.14a) and forms partial and rim replacement of plagioclase in the clast (Figs. 3.16 and 3.17a). Also, calcite is found enveloping the quartz and potassium feldspar fragments (Figs. 3.12). Calcite is typically associated with hydrothermal annite in the matrix, chlorite along the boundaries of fragments, and graphite (Figs. 3.16d and 3.17b). Calcite alters the plagioclase and potassium feldspar partially or completely. Anhedral calcite with the lowest $CaCO_3$ content (average 89.30 wt.%) is directly in contact with graphite within the matrix and along the grain boundaries in the clast. The occurrence of calcite along grain boundaries and its textural relationship with graphite suggests that it likely precipitated from hydrothermal fluids (Figs. 3.15a and 3.16).

Chlorite alteration is divided into two categories: replacive and non-replacive. Replacive chlorite is observed to occur along the grain boundaries of silicate minerals that comprise the breccia fragments (Fig. 3.10a). In addition, primary and secondary annite were replaced by chamosite in the Albany graphite deposit (Figs. 3.18 and 3.19). Titanite, as a product, is observed rimming the ilmenite that is associated with chloritization of annite (Fig. 4.6). Chloritization is often seen in direct contact with graphite and associated with pyrite (Figs. 3.17b and 3.19c). The textural relationship of chamosite and graphite indicates that chlorite may coevally with graphitization (Fig. 3.17(b), (d), and (f)).

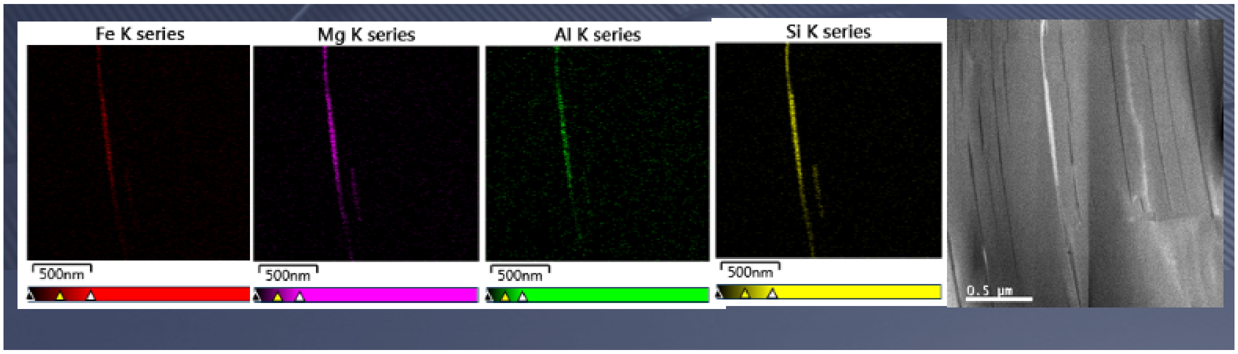

Figure 4.2 The HR-TEM-EDS elemental map showing nano-scale chlorite within the graphite, which is evidence of chlorite coexisting with graphite. (the result is shared with courtesy of Dr. A. Conly)

Non-replacive chamosite is observed along the grain boundaries of silicate minerals that comprise the breccia fragments. In contrast, non-replacive chamosite, which is found interstitial to isolated calcite grains and in dolomite veins, does not display any noticeable association with graphite (Figs. 3.14 and 3.28c). The SiO_2 content of replacive and non-replacive chamosite is usually uniform, around 37.85 wt.% and 32.57 wt.%, while average Al_2O_3 compositions are 9.69 wt.% and 14.13 wt.%, respectively. The observed replacive chamosite exhibits low MgO content (average 8.34 wt.% and 2.23 a.p.f.u.) and high FeO content (average 27.58 wt.% and 6.07 a.p.f.u.), whereas non-replacive Chamosite displays a higher MgO content (average 16.53 wt.% and 5.21 a.p.f.u.) and lower FeO content (average 20.27 wt.% and 3.59 a.p.f.u.). These findings are consistent with Morad et. al. (2011) and Wang et al. (2018) that hydrothermal chlorite tends to be more iron-rich (the average 6.4 a.p.f.u. Fe content of chlorite).

Sulphide minerals include pyrite with subordinate chalcopyrite and sphalerite. Sulphide paragenesis is not as well constrained as there is textural evidence to suggest that it spans pre-graphitization alteration to post-graphitization alteration. It is observed to be associated with graphite in the matrix (Figs. 3.4 (c) and (f)) and clast (Figs. 3.6f and 3.7). Pyrite is often found associated with calcite and chlorite (Figs. 3.17(b)-(d) and 3.19), while it is seen interstitial with sericite and hydrothermal annite (Fig. 3.16b). Additionally, pyrite is often observed in calcite (Fig. 3.7d) and dolomite veins (Fig. 3.14e). Chalcopyrite and sphalerite are often associated with pyrite, and both are observed together in calcite veins (Figs. 3.13d and 3.15b). Iron-Ti oxide minerals in the examined samples, ilmenite, and rare magnetite are observed. Ilmenite is observed associated with chloritized biotite in clasts and calcite alteration along the grain boundaries of clasts (Fig. 3.16d). Also, ilmenite and magnetite are found to be associated with pyrite (Figs. 3.5c, 3.7d, and 3.7f). Magnetite has been observed to be associated with carbonate and has an acicular texture that appears to fill an open space, indicating that it formed secondarily. (Fig. 3.14). Thus, Fe-Ti oxide minerals in the Albany deposit are directly in contact with graphite. Titanite is observed interstitial to calcite and is associated with disseminated graphite (Fig. 3.14b). Furthermore, titanite occurs as a result of the chloritization of annite and it is observed being in contact with graphite.

Post-graphitization alteration stage is characterized by carbonate veining, which includes calcite and rare dolomite veins. Both veins cut clast and matrix components. Calcite veins have higher $CaCO_3$ (average 91.25 wt.%) and $FeCO_3$ (average 2.07 wt.%) contents than calcite alteration in the graphitization stage, which display $CaCO_3$ (average 89.30 wt.%) and slightly lower $FeCO_3$ content (average 1.47 wt.%)(Fig. 3.13). Calcite veins sampled for this study are below the weathering profile, so they are non-weathering-related alteration. West (2016) determined that carbonate veining that is proximal to the unconformity (representing the paleo-surface at the time of diatreme emplacement) with the overlying Paleozoic marine carbonate rocks is comprised of dolomite. Both dolomite veining and hematitic overprinting of the breccia in proximity to the unconformity were determined to be products of meteoric water-related alteration (West, 2016). Both calcite and dolomite veins contain minor amounts of sulphide minerals. Both vein types contain pyrite, but minor amounts of chalcopyrite were observed only in calcite veins. Minor amounts of graphite were commonly observed distributed along the wall of calcite veins and are associated with pyrite (Figs. 3.7d and 3.13d). Graphite was not observed in dolomite veins. Both vein types are observed cross-cutting mineralized clast and matrix components.

Based on the observations, graphite has been deposited along the boundaries of brecciated host rock fragments. Additionally, a minor amount of graphite is observed along the walls of the calcite veins that are in the post-graphitization stage. The brecciated host rocks were variably hydrothermally altered to calcite and chamosite, which are constituents of a propylitic alteration assemblage. Both calcite and chamosite are observed with graphite along the grain boundaries of brecciated host rocks, which are pathways for fluid flow. Consequently, the textural relationship between propylitic alteration assemblage and graphite provides evidence that graphitization may occur coevally precipitate with calcite and chamosite.

4.2. Precipitation Mechanism of the Albany Graphite Deposit

4.2.1. The C-O-H System

The C-O-H system represents an igneous and/or metamorphic fluid composition in which H_2O dominates. The C–O–H ternary diagram can be used to show how graphite precipitation changes the composition of the fluid (Fig. 4.3) (Holloway, 1984; Luque et al., 1998; Ortega et al., 2010; Simandl et al., 2015). The stability field of graphite + fluid is a function of temperature (T), pressure (P), bulk composition, and oxygen fugacity (fO_2), and all these parameters cannot be independent at once because of the phase rule. For instance, at a given temperature and pressure, only compositions lying along the "graphite saturation curve" can be in equilibrium with graphite

(Luque et al., 1998, 2014). Fluids in the grey field are supersaturated in carbon and will precipitate graphite until it reaches an equilibrium fluid composition situated on the carbon saturation surface (Fig 4.3; Ortega et al., 2010).

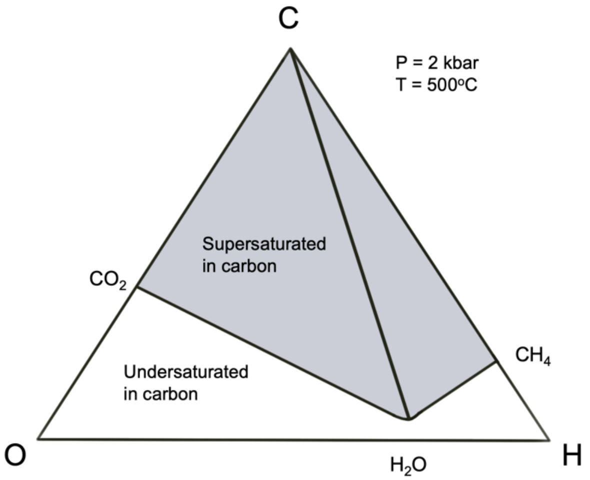

Figure 4.3 C–O–H fluid system showing supersaturated in carbon area also known as graphite stability field at 2 kbar and 500°C (Ortega et al., 2010; Simandl et al., 2015).

The C-O-H system becomes univariant when elemental carbon exists as a solid phase under specific fixed pressure-temperature (P-T) conditions. The following four independent equations can be used to express the graphite-fluid equilibrium (French, 1966; Frost, 1979; Holloway, 1984; Lamb William & Valley J. W., 1984; Ohmoto & Kerrick, 1977).

$$CO_2 \rightarrow C + O_2$$

$$CO \rightarrow C + {}^{1}/{}_{2}O_2$$

$$H_2O \rightarrow H_2 + {}^{1}/{}_{2}O_2$$

$$CH_4 \rightarrow C + 2H_2$$

The fluid coexisting with graphite mainly consists of H_2O and CO_2. The equilibrium $CO_2 \rightarrow C + O_2$ is the dominant control on the stability of graphite at high temperatures and relatively high oxygen fugacity (Frost, 1979). CH_4 becomes the most important species at lower oxygen fugacity (fO_2), with H_2O and H_2 as the other major components (Holloway, 1984). At these conditions, the controlling equilibrium is:

$$CH_4 + O_2 \rightarrow C + 2H_2O \quad (1)$$

In the case of graphite precipitate from a CO_2-bearing fluid, an alternative reaction is:

$$CO_2 + 2H_2 \rightarrow C + 2H_2O \quad (2)$$

Re-expressing the previous reaction as a Fischer-Tropsch reaction gives the following results (e.g., Salvi and Williams-Jones, 1997):

$$CO_2 + 4H_2 \rightarrow CH_4 + 2H_2O \quad (3)$$

We can take into consideration the following reactions involving CO_2 and CH_4 from which graphite can precipitate from a C-O-H fluid (Barrenechea et al., 2009; Ortega et al., 2010):

$$CO_2 \rightarrow C + O_2 \quad (4)$$

$$CO_2 + CH_4 \rightarrow 2C + 2H_2O \quad (5)$$

$$CH_4 + O_2 \rightarrow C + 2H_2O \quad (6)$$

4.2.2. The Mobilization and Mechanisms of Precipitation of Graphite

Carbon is transported as mobile species such as CH_4 and CO_2 dominantly or carbonate and bicarbonate ions in aqueous fluids. To transport and precipitate graphite, certain molecular reactions must occur. Graphite precipitates from a CO_2-CH_4-H_2O fluid through various mechanisms (Barrenechea et al., 1997; Luque et al., 1998; Ortega et al., 2010; Rumble, 2014; Rosing-Schow et al., 2017; Touret et al., 2019):

(1) reducing the temperature or increasing the pressure;
(2) mixing of fluid with a different CO_2/CH_4 ratio;
(3) hydration reactions between the fluid and anhydrous minerals in the host rock; and,
(4) reduction of the fluid.

4.2.2a Isobaric cooling or isothermal pressure increase (Temperature-Pressure Variations)

Graphite saturation curves on C-O-H ternary diagrams are temperature and pressure-dependent (Huizenga & Touret, 2012; Simandl et al., 2015). The thermodynamic requirement for graphite precipitation is the change of P-T conditions, where increasing the pressure and/or decreasing the temperature expands the graphite stability field (Luque et al., 1998a; Simandl et al., 2015). The most effective mechanism leading to graphite precipitation is the cooling of the carbon-containing aqueous fluid (Luque et al., 1998).

As displayed in Figure 4.4a, the graphite stability field increases with decreasing temperature at constant pressure (Ortega et al., 2010a; Simandl et al., 2015). For instance, assuming a constant pressure of 2 kb, the cooling of a C-O-H fluid with composition Z at temperatures of 1000°C or 700°C does not result in the precipitation of graphite. However, the graphite will precipitate before the fluid cools below 400°C (Simandl et al., 2015). At constant temperature, the stability field of graphite increases with increasing pressure (Barrenechea et al., 1997; Ferry &Baumgartner, 1987; Simandl et al., 2015). For example, graphite will not precipitate from a fluid of composition Y at pressures of 0.5 and 1.0 kb at 500°C, but when the pressure is 3 kb or higher, it will start to precipitate (Fig. 4.4b).

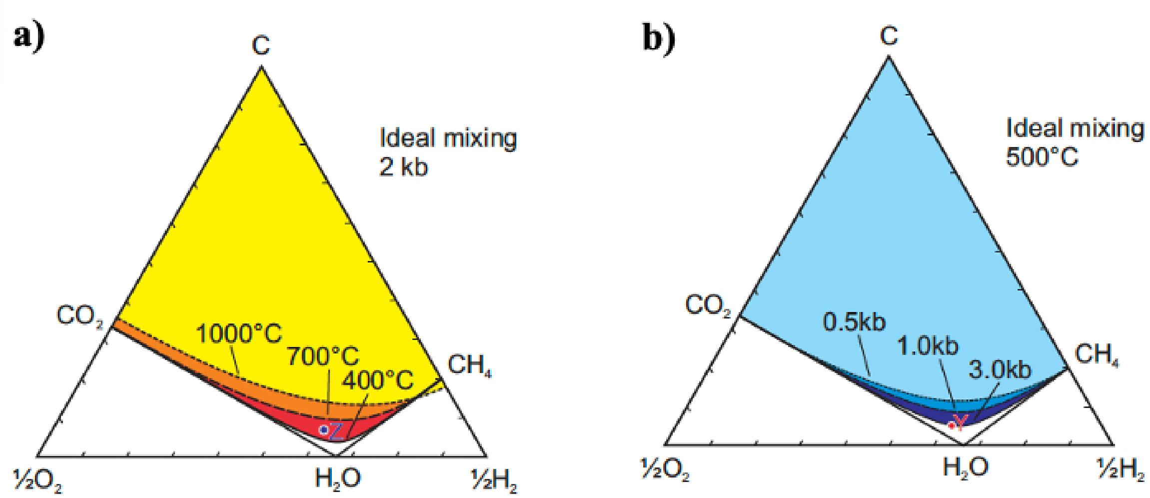

Figure 4.4 a) Ternary C-O-H diagram showing the effect of temperature and pressure variations on graphite precipitation. Increasing size of graphite stability field with decreasing temperatures from 1000º to 400°C

for the constant pressure of 2 kb, b) Ternary C-O-H diagram showing the increasing size of graphite stability field with increasing pressure from 0.5 to 3.0 kb for constant temperature of 500°C, assuming ideal mixing (Simandl et al., 2015).

However, the temperature effect can not be fully assessed for the Albany deposit. The fine-grained nature and random orientations indicate rather rapid nucleation with limited time for crystal growth. Thus, temperature effects if present are postulated minimal. In addition, the role of temperature has not been fully evaluated. The XRD graphite geothermometer yielded an average temperature (based on a bulk sample) for Albany of 571°C within ±20 to 50°C error (Conly and Moore, 2015). Initial attempts to evaluate, using *in situ* Raman graphite geothermometry, possible temperature effects between the pipes and across individual pipes lead to inconsistent results, possibly due to crystallographic modification induced by the development of turbostratic graphite, a variant of hexagonal graphite (Conly, personal communication, 2022). Pressure effects have not been evaluated for Albany. Graphite precipitation is typically induced by an increase in pressure (Luque et al., 1998, 2014). Nevertheless, the Albany deposit is a geological formation characterized by a vent breccia/diapir-hosted system that extends to the paleosurface. Consequently, it would have been subject to rapid loss of pressure (Conly & Moore, 2015).

4.2.2b Mixing of different C-bearing fluids

Changes in fluid composition can also occur by the incorporation of one gas species into another by in situ diffusion or by more dynamic fluid mixing between two chemically different reservoirs (Luque et al., 1998). Figure 4.5 demonstrates the effects of fluid mixing on the precipitation of graphite can be visualized in the C-O-H diagram at 600°C and pressure of 3.5 kb. Different fluid compositions are shown as points (A, B, C, D, E, and F) on the diagram. The composition of the fluid at point A, located in the graphite stability area, changes as graphite precipitates, as indicated by the green arrow. To precipitate graphite, the composition of the fluid changes along the corresponding tie-line, moving in the direction of the graphite saturation curve.

Fluids with compositions B and F lie outside the stability field of graphite, and graphite cannot precipitate from any of these liquids by itself. If we combine these two fluids, the composition of the resulting mixture will be at some point along the mixing line B-F. The mixing of two aqueous fluids (which are not saturated with respect to graphite), one CO_2-rich (B) and another CH_4-rich (F), can result in composition C and D within the field graphite + fluid. As more fluid F is added to the system, the composition of the resulting fluid will keep shifting from point C until it reaches point D, and graphite will start to precipitate. Graphite continues to precipitate as more fluid with composition F enters the system. The fluid's composition follows the graphite saturation curve, passing through point E. In this situation, graphite precipitation will occur by the reaction $CO_2 + CH_4 \rightarrow 2C + 2H_2O$ (Luque et al., 1998; Rumble et al., 1982; Rumble & Hoering, 1986; Simandl et al., 2015).

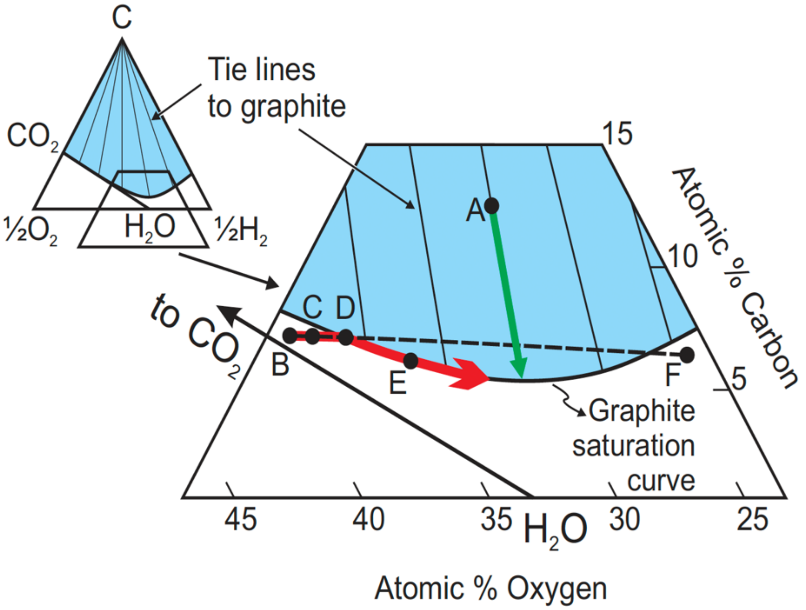

Figure 4.5 The C-O-H ternary diagram shows the effect of the fluid of composition A (within the graphite stability field) and the mixing of fluids of composition B and F (outside of the graphite stability field) to graphite precipitation at 600°C and 3.5 kb (Simandl et al., 2015).

4.2.2c Hydration reactions (Hydrous Alterations)

Hydrous reactions enable graphite precipitation by changing the composition of the fluid under specific pressure and temperature conditions (Luque et al., 1998; Ortega et al., 2010; Rosing-Schow et al., 2017). These reactions tend to occur at relatively low temperatures. Hydration reactions can reduce the H_2O content of the fluid, which causes an enriching carbon in the fluid and triggers the deposition of graphite (Luque et al., 1998, 2013; Rumble, 2014).

4.2.2d Precipitation reactions catalyzed by reducing agents

Based on both experimental (Morgan et al., 1992) and some natural occurrences, graphite precipitation can be triggered due to the presence of catalyzing minerals. It is well known that certain compounds (i.e., sulfides and oxides) act as catalysts during the process of metamorphic graphitization. Duke and Rumble (1986) show that pyrrhotite appears to play a role in the graphite vein deposits of New Hampshire. At the well-known Borrowdale replacement deposit, it was observed that the presence of graphite rims around pyrite and hematite cores led to the postulate that graphite precipitation was catalyzed by these minerals (Luque et al., 1998).

4.3. The Role of Hydrothermal Alteration for Precipitation of Graphite at the Albany Deposit

The graphite in the Albany deposit has been suggested to be the result of the combination of a carbonaceous fluid phase (CO_2-CH_4-H_2O) that is segregated from a mantle-derived melt and carbon derived from the metasedimentary country rock (Conly & Moore, 2015). The specific carbon species composition of the mineralizing fluid is unknown for the Albany deposit. In the absence of fluid inclusion studies, the textural features of alteration assemblages and graphite, as suggested by Luque et. al., (2012), could provide valuable insights into the mechanism of graphite deposition.

Consequently, fluid-related mechanisms are more likely responsible for graphite precipitation at Albany. Regarding the exact mechanisms, graphite will precipitate from a CO_2-CH_4-H_2O-bearing fluid (Barrenechea et al., 2009; Ortega et al., 2010) through equations (2), (4), (5), and (6).

Graphite may have precipitated due to the Fischer-Tropsch reaction (Equation 2), which requires the addition of H_2, which can be produced via:

$$2\,Fe^{2+}_{(aq)} + 2H_2O \rightarrow 2Fe(OH)^{+} + H_2 \quad (7)$$

To decrease the amount of CO_2 in the fluid to precipitate graphite from CO_2-bearing fluid is to have minerals (Fe^{3+}- containing) co-precipitating with graphite to provide changes in the fO_2

of the liquid required to trigger graphite precipitation. The presence of Fe-Ti-oxides (ilmenite and magnetite) and hematite are the common minerals that provide the necessary Fe to trigger the formation of graphite. However, the abundance of magnetite and ilmenite is low (<1 modal%). Moreover, hematite is associated with post-emplacement weathering/supergene alteration, which was likely related to the development of the unconformity and deposition of the overlying carbonate rocks (West, 2016). Based on this knowledge, it was concluded that iron oxides and hematite are insufficient sources of Fe to provide changes in the fO_2 of the liquid.

Hydrogen can be derived through wall-rock alteration reactions, resulting in the formation of a hydrous mineral phase (e.g., Salvi & Williams-Jones, 1997). A key wall-rock alteration observed in the Albany graphite deposit is the replacement of Fe-rich annite by Fe-rich chlorite (chamosite) with titanite and as associated by-products (Fig. 4.6).

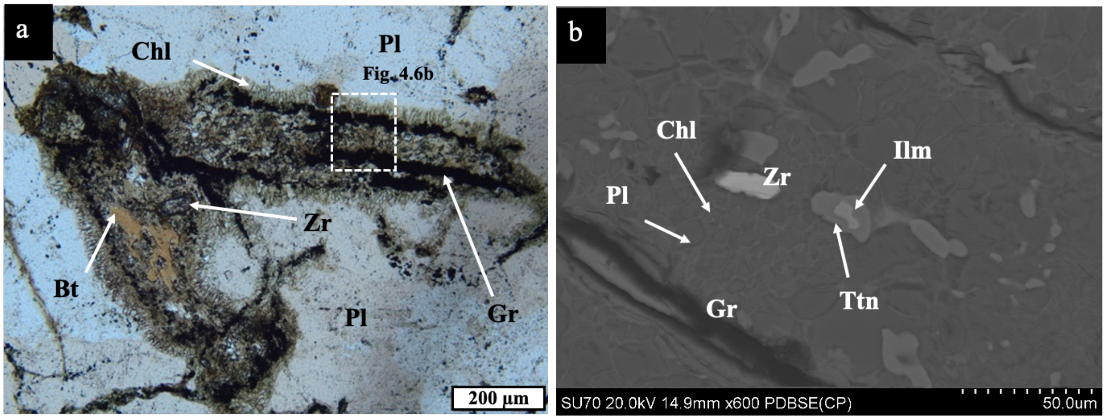

Figure 4.6 Representative image of chloritization of biotite. Plane-polarized (a) transmitted light shows the biotite is replaced by chlorite, which is co-precipitated with graphite. BSE (b) image showing the association of titanite rimming ilmenite during chloritization.

The process of mass transfer between the reactant and product minerals during the chloritization of annite is demonstrated. The reaction that results in annite and ilmenite being altered to chamosite with the co-precipitation of titanite, assuming Al is preserved, is presented as follows:

$$1.42\ \textbf{annite} + 1.02\ \textbf{ilmenite} + 0.33\ Mg^{2+} + 1.62\ Ca^{2+} + 0.56\ Si^{4+} + 6.36\ H_2O \rightarrow$$
$$\textbf{chamosite} + 1.5\ \textbf{titanite} + 0.48\ Fe^{2+} + 0.07\ Mn^{2+} + 2.59\ K^{+} + 2.40\ H^{+} + 0.11\ Cl^{-}$$

The above stoichiometry is based on the following based on average compositions of SEM-EDS-determined mineral compositions:

- Annite: [$K_{1.85}$ ($Fe_{3.01}$ $Mg_{2.42}$ $Ti_{0.32}$) ($Al_{2.40}$ $Si_{5.68}$ O_{20}) $(OH)_4$ ($Cl_{0.08}$)]
- Ilmenite: [($Fe_{0.88}$ $Ti_{0.95}$ $Mn_{0.07}$ $Ca_{0.05}$) ($Si_{0.03}$ $Al_{0.01}$ O_3)]
- Chamosite: [($Ca_{0.17}$ $K_{0.04}$)($Fe_{4.66}$ $Mg_{3.77}$)($Si_{7.16}$ $Al_{3.34}$ O_{20}) $(OH)_{16}$]
- Titanite: [($Fe_{0.02}$ $Al_{0.05}$) ($Ca_{1.0}$ $Ti_{0.95}$) ($Si_{1.00}$ O_5)]

This reaction equation, in which annite and ilmenite are the reactants and chlorite and titanite form the products, indicates that the reaction consumes Mg^{2+}, Ca^{2+}, Si^{4+}, H_2O, and H^+, and releases Fe^{2+}, K^+, Mn^{2+}, and Cl^- into the hydrothermal fluid with the later suggesting a drop in pH. Ti^{3+} released from biotite with the addition of Ca^{2+} precipitates as titanite (Morad et. al., 2011). Si can be liberated from any silicate alteration phase, while Ca is liberated from the alteration of plagioclase. Titanium released from annite, and ilmenite is assumed to re-precipitate as titanite. Fe is released from annite and ilmenite into the hydrothermal fluid. Liberated iron from the wall-rock alteration reaction can provide the H_2, through equation (5), which is required for the Fischer-Tropsch reaction (4) to occur.

Coeval with graphite deposition, the host rocks were variably hydrothermally altered to a propylitic assemblage, of chamosite and calcite. Graphite precipitation was probably triggered by hydration reactions (chloritization) and CO_2 (calcite precipitation). Luque et al. (2013), emphasize that most of the igneous-hosted graphite deposits occurred from fluids containing both CO_2 and CH_4 as carbon species. Calcite is observed to be altering the host-rock phases (plagioclase and potassium feldspar) and is directly associated with graphite in the Albany deposit (Figs. 3.15a and 3.16). According to Duke and Rumble's (1986) study on isotopic variations of graphite in the New Hampshire deposit, established co-precipitation of calcite and graphite will not directly affect the equilibrium value of $\Delta_{(graphite\text{-}fluid)}$ ($\Delta_{(graphite\text{-}fluid)} = \delta^{13}C_{graphite} - \delta^{13}C_{fluid}$). However, they noted that there is an indirect effect that could lead to changing $\delta^{13}C$ values in subsequently formed graphite, which is the reduction of CO_2.

Figure 4.7 illustrates that graphite can precipitate from the fluid at a constant temperature (400 C) from point 2 onwards. During this process, the composition of the fluid changes along the fayalite–magnetite–quartz buffer (FMQ) iso-fugacity line as indicated with the red arrow. Moving from points 2 to 3, the mole fraction of CO_2 decreases and, the mole fraction of H_2O increases in the fluid. The reduction in CO_2 leads to the crystallization of calcite. The CH_4:CO_2 ratio in the fluid will increase and lead to graphite precipitation. The reaction would be $CO_2 \rightarrow C+O_2$, as shown by trajectory 3 in Figure 4.6B. The reduction in CO_2 would continue until the iso-fugacity line curved towards the O–H binary. (e.g., Borrowdale; Ortega et al., 2010). Also, Duke and Rumble observed an increase in the $\delta^{13}C$ of graphite which was attributed to the reduction of CO_2 in the New Hampshire deposit. It was concluded that calcite may play a role, in determining the isotopic composition or speciation of fluids (Duke and Rumble, 1986). Consequently, the removal of CO_2 due to calcite precipitation could be a possible reaction leading to the crystallization of the graphite through the reaction $CO_2 \rightarrow C+ O_2$.

In addition to the chloritization of biotite, chlorite is observed rimming rock-forming silicate fragments and is in association with plagioclase. Petrographic observations and chemical results indicate that graphite and chamosite coexist (see Figs. 3.17, 3.18, and 3.19). According to the HR-TEM-EDS result, the presence of nano-scale chlorite in graphite (Fig. 4.2) provides evidence that chlorite, one of the dominant components of aqueous alteration, is co-precipitated with graphite. Precipitation of chlorite would deplete the fluid in H_2O, thereby enriching the remaining fluid in C and driving it to graphite saturation (Fig. 4.8), resulting in graphite precipitation (e.g., New Hampshire, USA and Borrowdale, UK; Duke and Rumble, 1986; Luque et al., 2009; Ortega et. al., 2010; Rumble, 2014). The composition of the residual fluid will move towards the saturation surface of graphite due to the reaction that is consuming H_2O, as shown by the red arrow in Figure 4.8. Continuing dehydration of the fluid drives the fluid along the saturation curve toward either higher or lower values of CO_2 and CH_4 (as depicted with blue and green contours in Figure 4.8) depending on the initial bulk composition (Duke and Rumble, 1986).

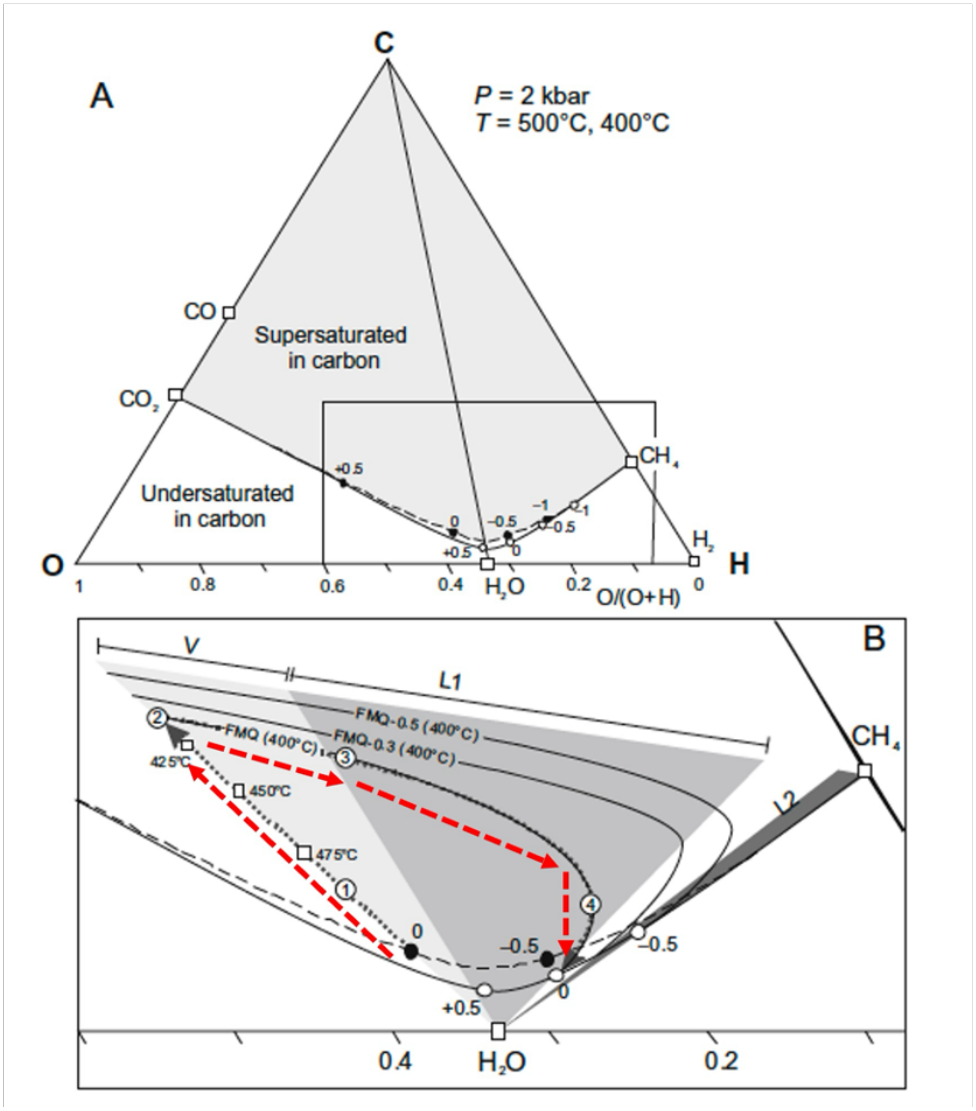

Figure 4.7 C–O–H fluid system displays the CO_2 reduction. (A) C–O–H fluid system displays the carbon saturated fluid compositions, as a function of the fluid fO_2, and this is known as the carbon saturation surface (P=2 kbar. Solid line indicates 500°C, while dashed line indicates 400°C). The circles represent the fluid fO_2 in log10 units relative to the FMQ. The open circles correspond to a temperature of 500°C, while the solid circles correspond to a temperature of 400°C. (B) is a magnification of the marked area in (A), and exhibits iso-oxygen fugacity lines that have been determined at a temperature of 400°C. The grey dashed arrows denote the fluid compositional variations during graphite precipitation. The shaded areas represent the compositional fields of the various inclusion types (V, L1, and L2) based on the mole fraction of #XCO_2. Trajectory 1 illustrates the removal of H_2O from the carbon-saturated fluid as a result of hydration reactions during cooling until it reaches point 2. Trajectory 3 represents the precipitation of graphite as a result of the reduction of CO_2 while maintaining a constant fO_2 level at FMQ. In the last phase of graphite precipitation (trajectory 4), the primary reaction responsible for graphite precipitation changes to the oxidation of CH_4 (Ortega et al., 2010).

Conly and Moore (2015) state that the initial graphite-bearing fluid in the Albany deposit was likely CO_2-rich rather than CH_4-rich. Consequently, if the fluid was CO_2 dominant with minor CH_4 after removing H_2O, a possible reaction for the graphite precipitation would be $CO_2 + CH_4 \rightarrow C + 2H_2O$.

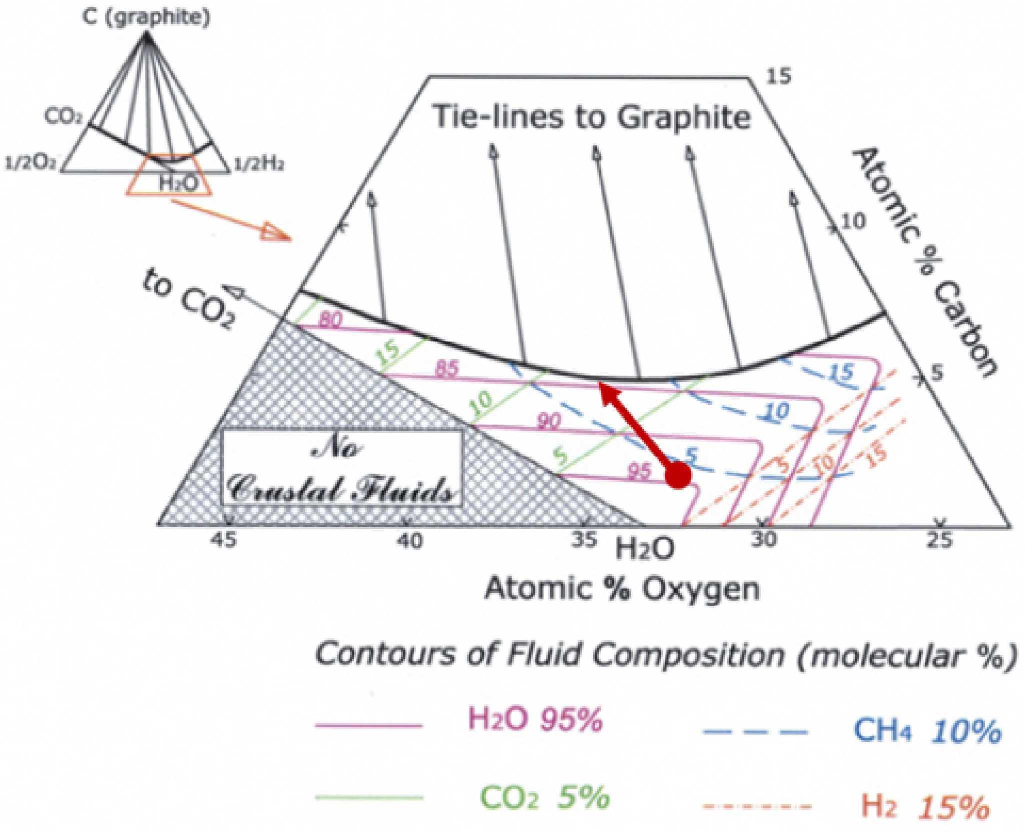

Figure 4.8 The C–O–H diagram illustrates the molecular percent of the fluid composition at 600 °C and 3.5 kbars) The saturation surface of graphite in equilibrium with C-O-H molecular fluid is represented by the heavy black line. The contours in different colours depict the molecular percentages of H_2O, CO_2, CH4, and H_2 compositions. The red arrow is denoting a pathway in which water is being removed from the fluid due to the formation of hydrous alteration phases. (after Rumble et al. 2014).

Based on petrographic observations, potassic alteration (annite) is pre-graphitization and graphite occurred coevally with a propylitic assemblage comprised of calcite and chlorite. Potassic alteration (annite) typically occurs at a temperature around 600°C (David and Vaccaro, 2012). Although the optimal temperature for graphite precipitation is typically between 400 and 500°C at 2 kb (Barrenechea et al., 1997; Simandl, 2015), graphitization temperatures can occur up to 800°C in Sri Lanka (Luque, et al., 2013). On the other hand, the temperature of propylitic alteration ranges from 160 to 350°C (Norman et al., 1991), while Deer et al. (2013) noted that chlorite can form at temperatures up to approximately 400°C. However, considering the stability of the propylitic assemblage, which is stated to be related to graphite mineralization, the temperature of graphite precipitation indicated is around 500°C in the Borrowdale deposit (Ortega et al., 2010). Conly and Moore (2015) used X-ray diffraction and Raman geothermometry to assess the crystallization temperature of the Albany graphite deposit. While X-ray diffraction results indicate an average crystallization temperature of 574°C (±20°C), Raman geothermometry yields a maximum crystallization temperature of 581°C (±50°C). Considering the error rates of graphite crystallization temperature of the Albany deposit (approximately 500–550°C), they are compatible with the temperatures of propylitic alteration, coevally with graphitization, stated in the literature (approximately 500°C) (e.g., Borrowdale; Ortega et al., 2010). In addition to the textural relationships of graphite and alteration assemblages, considering the temperature of potassic and propylitic alterations and the temperature to precipitate graphite, it is likely that graphitization might have occurred during propylitic alterations.

Chapter 5. CONCLUSION AND FUTURE WORK

Albany is characterized by microcrystalline graphite that can form aggregated masses that are <0.05 mm in width and range from 0.1 to 1.5 mm in length. Its distribution is controlled by the orientation of breccia fragments, crystal boundaries, and veins. Randomly oriented graphite crystals show intergranular and intragranular textures which they were observed both in the East and West pipes. Graphite is mainly distributed along grain boundaries in the clast (intragranular), whereas it shows intergranular texture in the matrix.

Clasts consist of both polymineralic and monomineralic lithic fragments that are > 1.5 mm. While the composition of individual clasts is highly variable, the bulk mineralogy of the clast component of the breccias consists of plagioclase (20-25%), potassium feldspar (15-20%), quartz (<15%), biotite (<15%), graphite (<10%), and minor amount amphibole, pyroxene, and chlorite, which is <5%, 3 to 5%, 3 to 5%, respectively. Additionally, the clasts contain trace to <2% carbonates, sulphides (pyrite and chalcopyrite), Fe-Ti-oxides (ilmenite and magnetite), and accessory minerals (apatite, titanite, and zircon). Matrix is defined as comprised of polymineralic and monomineralic lithic fragments and discrete mineral grains that are <1.5 mm and are dominantly anhedral in form. The most abundant minerals that comprise the matrix are plagioclase (20-25%), potassium feldspar (<20%), quartz (15-20%), graphite (<15%), biotite (<10), and calcite (<5%) with subordinate amounts of amphibole (<2%), pyroxene (<3%), sulphides (with pyrite being the most abundant). Fe-Ti-oxides (ilmenite and magnetite), and an array of accessory minerals (apatite, titanite, zircon, and chromite) that comprise <3% of the matrix. Notably, graphite is found to be more abundant in the matrix (<15%) compared to the clasts (<10%).

The formation of the Albany graphite deposit can be characterized by four distinct stages:

Stage 1: Host rock.

This stage represents the formation of the host rock, initial brecciation, and hydrothermal components that are not associated with graphitization. It is responsible for the formation of the primary rock-forming minerals (e.g., plagioclase, potassium feldspar, quartz, igneous annite, metamorphic annite, phlogopite, amphibole, and pyroxene). Graphite associated with these phases displays secondary textures, as it both penetrates grain boundaries within fragments and as well as riming the fragments.

Stage 2: Pre-graphitization alterations.

It is characterized by hydrothermal alteration assemblages such as sericite and hydrothermal annite. Potassium feldspar and plagioclase grains are observed to be intensely altered to sericite. Hydrothermal annite is often observed replacing the rim of plagioclase and potassium feldspar. In addition, occasionally it is seen completely altering amphibole. Graphite is observed at the boundaries of the sericitized feldspar grains and along the cleavage planes of annite, which indicates graphitization occurs after sericite and hydrothermal annite.

Stage 3: Graphitization.

It is defined by the formation of calcite and chlorite alterations. Non-weathering-related calcite alteration often occurs as overgrowths to rim replacements on plagioclase, while in some cases it results in a total replacement. Very fine-grained calcite is found to be associated with hydrothermal annite. This textural relationship indicates that calcite alteration occurs after hydrothermal annite alteration. Furthermore, calcite was observed with chlorite along the boundaries of fragments and graphite. Chlorite is observed replacing the plagioclase boundaries. Moreover, primary and secondary annite are partially and/or completely altered by chlorite. Alterations in this stage are often associated with pyrite, ilmenite, and titanite. Graphite, which occurs in high modal abundance, is in direct contact with chamosite and calcite (propylitic alteration) in the matrix. The textural relationship between calcite, chamosite, and graphite indicates that graphitization may be syngenetic with propylitic alteration.

Stage 4: Post-graphitization alterations.

The post-graphitization alteration stage consists of abundant calcite veins and rare dolomite veins. The assemblages of the clasts and matrix are cross-cut by both calcite and dolomite veins. Both calcite and dolomite veins are associated with pyrite. The calcite veins are below the weathering profile, while dolomitization may be related to the weathering-related alteration. Graphite is observed along the calcite vein walls, while dolomite veins are found cutting the graphite, which is situated along the boundaries of fragments.

Table 5.1 Characteristic of four stages: host rock, pre-graphitization alterations, graphitization, and late to post-graphitization alterations.

Stage	Minerals and Alterations	Relationship with graphite
Host Rock	Plagioclase, potassium feldspar, quartz, igneous annite, metamorphic annite, phlogopite, amphibole, and pyroxene	Graphite penetrates grain boundaries and rims fragments
Pre-Graphitization Alteration	Sericite and hydrothermal annite	Graphite rims the fragments and deposits parallel to the foliation of fragments
Graphitization	Calcite and chamosite	Graphite is directly in contact with alteration assemblages
Late to Post-Graphitization Alteration	Calcite and dolomite veining	Graphite deposited along the vein wall

Data from SEM-EDS analyses of biotite, calcite, and chlorite were used to further constrain mineral paragenesis and possible fluid-rock interactions. Biotite is significant due to its occurrence as both an alteration phase and rock-forming mineral present in igneous and metamorphic fragments. Data from the SEM-EDS analyses indicate the biotite in the Albany deposit was mainly annite, except for phlogopite contained in lamprophyre fragments that were observed in a single sample. Igneous and metamorphic annite (primary annite) are Fe- (average FeO of 23.07 and 19.66 wt.%, respectively) and Ti-rich (average $TiO_2$of 3.94 and 2.77 wt.%, respectively), while hydrothermal annite (secondary annite) are Mg-rich (average MgO of 15.67 wt.%) that indicates the alteration processes cause to either Fe loss or Mg enrichment in annite content. Furthermore, calcite and chamosite play an important role as they both comprise a propylitic alteration assemblage that is associated with graphite. Replacive calcite contains around 90% $CaCO_3$.

Replacive calcite contains minor but varying $FeCO_3$, $MnCO_3$, and $MgCO_3$. Data from SEM-EDS analyses indicate that chlorite is chamosite (Fe-rich chlorite).

In general, the most effective mechanism leading to graphite precipitation is increasing the pressure and/or decreasing the temperature. However, the effects of both are not considered to be effective mechanisms for the Albany graphite deposit. In addition to inconsistent results obtained from *in situ* Raman graphite geothermometry by Conly and Moore (2015), the fine-grained nature and random orientations of graphite indicate rather rapid nucleation with limited time for crystal growth. Moreover, the Albany deposit is a geological formation distinguished by a vent breccia/diapir-hosted system that extends to the paleosurface. Consequently, it would have been subject to rapid loss of pressure, leading to a situation of quenched graphite crystallization.

The role that the various hydrous alterations played in graphite precipitation was considered and evaluated. One way to precipitate graphite is via CO_2 reduction, which requires the addition of H_2 which could be provided through a Fischer-Tropsch reaction involving Fe-containing minerals. However, Fe-Ti-oxides within the deposit (ilmenite, magnetite) have relatively low abundances (<1 modal%), and Fe-oxide phases such as hematite, are associated with post-emplacement weathering/supergene alteration. Thus, it is unlikely that sufficient H_2 was generated from the crystallization of minerals to induce a reduction in CO_2. However, an alternative way to obtain H_2 is from wall-rock alteration reactions, resulting in the formation of hydrous minerals. The wall-rock alteration observed in the Albany graphite deposit is that the alteration of annite and ilmenite by chamosite also resulted in the crystallization of titanite. According to mass transfer between the reactant and product minerals during the chloritization of annite, Fe^{2+} is released into the hydrothermal fluid and this could be oxidized in the presence of H_2O through equation ($2\ Fe^{2+}_{(aq)} + 2H_2O \rightarrow 2Fe(OH)^{+} + H_2$) leading to the production of H_2. It supplies the necessary hydrogen (H_2) for the Fischer-Tropsch process ($CO_2 + 2H_2 \rightarrow C + 2H_2O$) to take place, which could lead to the precipitation of graphite.

Reactions that were determined to be important for graphite precipitation resulted in the development of a propylitic assemblage comprised of chlorite and calcite. Graphite is observed directly in contact with hydrothermal annite, calcite, and chlorite. Precipitation of calcite causes a reduction of CO_2 from fluid and increases the CH_4:CO_2 ratio. It leads to a possible reaction for the graphite precipitation will be ($CO_2 \rightarrow C + O_2$). Additionally, readily observed is the replacement of Fe-rich annite replaced by Fe-rich chlorite. These petrographic observations are also supported by HR-TEM results, where chlorite occurs as nano-inclusions distributed along the basal plane of graphite. To form chlorite, H_2O would be depleted in the fluid, thus leading to an enrichment in C in the remaining fluid. This process would in turn lead to the precipitation of graphite Although it is not known exactly, Conly and Moore, (2015) stated that the initial graphite-bearing fluid in the Albany deposit was most likely enriched in CO_2 instead of CH_4. In the case where the fluid contains both CO_2 and CH_4, a possible reaction to precipitate graphite is $CO_2 + CH_4 \rightarrow C + 2H_2O$.

Based on the literature the temperature range for graphite precipitation is noted between 200°C and can reach up to 800°C (e.g., Sri Lanka). Moreover, the typical temperature of propylitic alteration and to form chlorite is up to approximately 400°C. The host rocks were variably hydrothermally altered to a propylitic assemblage, which includes chlorite and calcite. However, considering the stability of the propylitic community, which is stated to be associated with graphite mineralization, Ortega et al., (2010) established that the temperature of graphite crystallization in the Borrowdale deposit is around 500°C. The graphite crystallization temperature of the Albany deposit is approximately 550–600°C, considering the error rates established by Conly and Moore, (2015). These findings align with the temperatures associated with propylitic alteration, which occurs coevally with graphitization, as mentioned in the literature (Ortega et al.,2010). Calcite and chlorite are observed coevally with graphite along grain boundaries of brecciated host rocks, which are pathways of fluid flow. Taking into consideration of estimation of temperature ranges and textural relationships of propylitic assemblage and graphite indicated that graphite precipitation was probably triggered by the hydration reactions.

Future research on the Albany graphite deposit could benefit from advanced techniques like fluid inclusion and *in-situ* carbon isotope analysis. Comprehensive carbon isotope analysis helps to identify the origin of carbon. Not only ^{13}C of the graphite but also ^{13}C of calcite alteration, which is co-precipitate, help to determine the isotopic composition or speciation of fluids in the samples. If suitable fluid inclusions can be identified, the specific carbon-bearing species of the fluids can be determined using micro-Raman analysis. Coupling this with data from fluid inclusion microthermometry, a more precise understanding of the physico-chemical nature of the various fluids could be established. This could elucidate the origin of carbon and the nature of carbon-bearing species of the fluids, and aid in further constraining the possible graphite-forming reactions.

REFERENCES

Al-Ani, T., Ahtola, T., Cutts, K., & Torppa, A. (2022). Metamorphic evolution of graphite in the Paleoproterozoic Savo Schist Belt (SSB), Central Finland: Constraints from geothermetric modeling. *Ore Geology Reviews*, *141*, 104-672.

Aminroayaei Yamini, M., Tutti, F., Aminoroayaei Yamini, M. R., Ahmadian, J., & Wan, B. (2017). Examination of chloritization of biotite as a tool for reconstructing the physicochemical parameters of mineralization and associated alteration in the Zafarghand porphyry copper system, Ardestan, Central Iran: mineral-chemistry and stable isotope analyses. *Mineralogy and Petrology*, *111*, 747-759.

Balan, A., Kumar, R., Boukhicha, M., Beyssac, O., Bouillard, J. C., Taverna, D., Sacks, W., Marangolo, M., Lacaze, E., Gohler, R., Escoffier, W., Poumirol J.M., Shukla, A. (2010). Anodic bonded graphene. *Journal of Physics D: Applied Physics*, *43*(37), 374013.

Barrenechea, J. F., Luque, F. J., Millward, D., Ortega, L., Beyssac, O., & Rodas, M. (2009). Graphite morphologies from the Borrowdale deposit (NW England, UK): Raman and SIMS data. *Contributions to Mineralogy and Petrology*, *158*, 37-51.

Barrenechea, J. F., Luque, F. J., Rodas, M., & Pasteris, J. D. (1997). Vein-Type Graphite in Jurassic Volcanic Rocks of the External Zone of the Betic Cordillera, Southern Spain. *The Canadian Mineralogist*, *35*(6), 1379–1390.

Beyssac, O., Rumble, D., & Editors, G. (2014). A Ubiquitous, Diverse, and Useful Geomaterial from Organic Matter to Graphite Hydrothermal Graphitic Carbon Graphitic Carbons and Biosignatures Presolar Graphitic Carbon Spherules Carbon-Based Nanoscience Graphitic Carbon. www.asi-pl.com.au

Brown, T J, Idoine, N E, Raycraft, E R, Hobbs, S F, Shaw, R A, Everett, P, Kresse, C, Deady, E A, and Bide, T. (2019). World Mineral Production 2013–2017. British Geological Survey, Keyworth, Nottingham.

Card, K. D., & Ciesielski, A. (1986). Subdivisions of the Superior province of the Canadian Shield. *Geoscience Canada*, *13*(1), 5-13.

Conly, A. G., & Moore, L. C. (2015). Geology, ore characteristics, and origin of the Albany graphite deposit. *British Columbia Ministry of Energy and Mines, British Columbia Geological Survey Paper*, *2015*, 173-185.

Crossley P (2000) Graphite: High-tech supply sharpens up. Industrial Minerals 398, 31–47

Davis, D. W., Pezzutto, F., & Ojakangas, R. W. (1990). The age and provenance of metasedimentary rocks in the Quetico Subprovince, Ontario, from single zircon analyses: implications for Archean sedimentation and tectonics in the Superior Province. *Earth and Planetary Science Letters*, *99*(3), 195-205.

Davis, D. W., & Jackson, M. C. (1988). Geochronology of the Lumby Lake greenstone belt: a 3 Ga complex within the Wabigoon Subprovince, northwest Ontario. *Geological Society of America Bulletin*, *100*(6), 818-824.

Deer, W. A., Howie, R. A., & Zussman, J. (2013). *An introduction to the rock-forming minerals*. Mineralogical Society of Great Britain and Ireland. p.220.

Deer, W. A., Howie, R. A., & Zussman, J. (1992). An introduction to the rock-forming minerals. *Longman Group Ltd, New York, p 698Defant MJ, Drummond MS (1990) Derivation of some modern arc magmas by melting of young subducted lithosphere. Nature*, *347*, 662665Della.

Drever, C., Kinney, C., & Yakymchuk, C. (2023). Petrogenesis of extra-large flake graphite at the Bissett Creek deposit, Canada. *Mineralium Deposita*, *58*(4), 731-750.

Duke, E. F., & Rumble, D. (1986). Textural and isotopic variations in graphite from plutonic rocks, South-Central New Hampshire. *Contributions to Mineralogy and Petrology*, *93*, 409-419.

European Commission (2020). Critical raw materials resilience: charting a path towards greater security and sustainability. COM/2020/474 final.

Frank, M. R., & Vaccaro, D. M. (2012). An experimental study of high temperature potassic alteration. *Geochimica et cosmochimica acta*, *83*, 195-204.

Ferry, J. M., & Baumgartner, L. (1987). Thermodynamic models of molecular fluids at the elevated pressures and temperatures of crustal metamorphism. *Reviews in Mineralogy and Geochemistry*, *17*(1), 323-365.

French, B. M. (1966). Some geological implications of equilibrium between graphite and a C-H-O gas phase at high temperatures and pressures. *Reviews of Geophysics*, *4*(2), 223-253.

Frost, B. R. (1979). Mineral Equilibria Involving Mixed-Volatiles in a C-O-H Fluid Phase: the Stabilities of Graphite and Siderite. In *American Journal of Science*, 279(9), 1033–1059.

Gower, C. F., & Clifford, P. M. (1981). The structural geometry and geological history of Archean rocks at Kenora, north-western Ontario—a proposed type area for the Kenoran Orogeny. *Canadian Journal of Earth Sciences*, *18*(6), 1075-1091.

Hahn-Weinheimer, P., & Hirner, A. (1981). Isotopic evidence for the origin of graphite. *Geochemical Journal*, *15*(1), 9-15.

Heaman, L.M., (1988). A precise U-Pb zircon age for a Hearst dike. In Program with Abstracts, Annual Meeting Geological Association of Canada-Mineralogical Association of Canada, 13, A53.

Hollister, V. F., (1980), Origin of graphite in the Duluth Complex: Economic Geology, 75, 764-766.

Holloway, J. R., (1984). Graphite-CH_4-H_2O-CO_2 equilibria at low grade metamorphic conditions. *Geology, 12*, 455-458.

Huizenga, J. M. (2011). Thermodynamic modelling of a cooling C–O–H fluid–graphite system: implications for hydrothermal graphite precipitation. *Mineralium Deposita*, *46*(1), 23-33.

Huizenga, J. M., & Touret, J. L. (2012). Granulites, CO2 and graphite. *Gondwana Research*, *22*(3-4), 799-809.

Jagodits, F.L., Paterson, N.R. (1964). Report on the Interpretation of an Airborne Magnetic Survey over an Area in the Vicinity of the Nagagami River, Ontario; unpublished report prepared by Hunting Survey Corp. Ltd. for Algoma Ore Properties Ltd., 14p.

Johnson, M.D, Armstong, D.K., Sandord, B.V., Telford, P.G. and Rutka, M.A., (1991). Paleozoic and Mesozoic Geology of Ontario. *In Geology of Ontario, Ontario Geological Survey*, 4(1), 383-403.

Lamb, W., & Valley, J. W. (1984). Metamorphism of reduced granulites in low-CO2 vapour-free environment. *Nature*, *312*(5989), 56-58.

Landis, C. A. (1971). Graphitization of dispersed carbonaceous material in metamorphic rocks. *Contributions to mineralogy and petrology*, *30*(1), 34-45.

Legault, J.M., Lymburner, J., Ralph, K., Wood, P., Orta, M. and Prikhodko, A., (2015). The Albany graphite discovery airborne and ground time-domain EM. KEGS Geophysics Symposium, Society of Economic Geophysicists Technical Program Expanded Abstracts 2015, 2056-2060.

Li, Z. Q., Lu, C. J., Xia, Z. P., Zhou, Y., & Luo, Z. (2007). X-ray diffraction patterns of graphite and turbostratic carbon. *Carbon*, *45*(8), 1686-1695.

Luque, F. J., Crespo-Feo, E., Barrenechea, J. F., & Ortega, L. (2012). Carbon isotopes of graphite: Implications on fluid history. *Geoscience Frontiers*, *3*(2), 197-207.

Luque, F. J., Huizenga, J. M., Crespo-Feo, E., Wada, H., Ortega, L., & Barrenechea, J. F. (2013). Vein graphite deposits: geological settings, origin, and economic significance. *Mineralium Deposita*, *49*(2), 261-277.

Luque, F. J., Ortega, L., Barrenechea, J. F., Millward, D., Beyssac, O., & Huizenga, J. M. (2009). Deposition of highly crystalline graphite from moderate-temperature fluids. *Geology*, *37*(3), 275-278.

Luque del Villar, F. J., Pasteris, J. D., Wopenka, B., Rodas, M., & Fernández Barrenechea, J. M. (1998). Natural fluid-deposited graphite: mineralogical characteristics and mechanisms of formation. *American Journal of Science*, 298, 471-498.

Mitchell, C. J. (1993). Industrial minerals laboratory manual: flake graphite. British Geological Survey Technical Report WG/92/30, 31 pp.

Morad, S., Sirat, M., El-Ghali, M. A. K., & Mansurbeg, H. (2011). Chloritization in Proterozoic granite from the Äspö Laboratory, southeastern Sweden: record of hydrothermal alterations and implications for nuclear waste storage. Clay minerals, 46(3), 495-513.

Morgan, G. B., Chou, I. M., & Pasteris, J. D. (1992). Speciation in experimental COH fluids produced by the thermal dissociation of oxalic acid dihydrate. *Geochimica et Cosmochimica Acta*, *56*(1), 281-294.

Ohmoto, H. (1977). Devolatilization equilibria in graphitic systems. *American Journal of Science*, *277*(8), 1013-1044.

Olson DW (2011) Graphite. In: U.S. Geological Survey Minerals Yearbook-2009. U.S. Geological Survey, Reston, Virginia, 32.1-32.10

Ortega, L., Luque, F. J., Barrenechea, J. F., Rodas, M., Millward, D., Beyssac, O., ... & Adshead, N. (2009). Assimilation, hydrothermal alteration and graphite mineralization in the Borrowdale deposit (UK). *Smart Science for Exploration and Mining*, *1*, 257-259.

Ortega, L., Millward, D., Luque, F. J., Barrenechea, J. F., Beyssac, O., Huizenga, J. M., Rodas, M., Clarke, S. M. (2010). The graphite deposit at Borrowdale (UK): a catastrophic mineralizing event associated with Ordovician magmatism. *Geochimica et Cosmochimica Acta*, *74*(8), 2429-2449.

Pan, Y., Fleet, M. E., & Heaman, L. (1998). Thermo-tectonic evolution of an Archean accretionary complex: U–Pb geochronological constraints on granulites from the Quetico Subprovince, Ontario, Canada. *Precambrian Research*, *92*(2), 117-128.

Pan, Y., Fleet, M. E., & Williams, H. R. (1994). Granulite-facies metamorphism in the Quetico Subprovince, north of Manitouwadge, Ontario. *Canadian Journal of Earth Sciences*, *31*(9), 1427-1439.

Parnell, J., Brolly, C., & Boyce, A. J. (2021). Mixed metamorphic and fluid graphite deposition in Palaeoproterozoic supracrustal rocks of the Lewisian Complex, NW Scotland. *Terra Nova*, *33*(6), 541-550.

Parsapoor, A., Khalili, M., Tepley, F., & Maghami, M. (2015). Mineral chemistry and isotopic composition of magmatic, re-equilibrated and hydrothermal biotites from Darreh-Zar porphyry copper deposit, Kerman (Southeast of Iran). *Ore Geology Reviews*, *66*, 200-218.

Pasteris, J. D., & Chou, I. M. (1998). Fluid-deposited graphitic inclusions in quartz: Comparison between KTB (German Continental Deep-Drilling) core samples and artificially reequilibrated natural inclusions. *Geochimica et Cosmochimica Acta*, *62*(1), 109-122.

Pasteris, J. D., Harris, T. N., & Sassani, D. C. (1995). Interactions of mixed volatile-brine fluids in rocks of the southwestern footwall of the Duluth Complex, Minnesota; evidence from aqueous fluid inclusions. *American Journal of Science*, *295*(2), 125-172.

Pasteris, J. D., (1989), Methane-nitrogen fluid inclusions in igneous rocks from the Duluth Complex, Minnesota: Pan-American Conference on Fluid Inclusions Research, 2nd, Program and Abstracts, 51.

Percival, J.A., Skulski, T., Sanborn-Barrie, M., Stott, G.M., Leclair, A.D., Corkery, M.T., and Boily, M. (2012). Geology and tectonic evolution of the Superior Province, Canada. Chapter 6 In Tectonic Styles in Canada: The LITHOPROBE Perspective. Edited by J.A. Percival, F.A. Cook, and R.M. Clowes. *Geological Association of Canada*, Special Paper 49, 321–378.

Percival, J. A. (2007). Geology and metallogeny of the Superior Province, Canada. *Mineral deposits of Canada: A synthesis of major deposit-types, district metallogeny, the evolution* *of geological provinces, and exploration methods: Geological Association of Canada, Mineral Deposits Division, Special Publication*, *5*, 903-928.

Percival, J. A. (2004). Orogenic framework for the Superior Province : Dissection of the " Kenoran Orogeny ." *The Lithoprobe Celebratory Conference: From Parameters to Processes - Revealing the Evolution of a Continent*, 12–15.

Percival, J. A., & Williams, H. R. (1989). Late Archean Quetico accretionary complex, Superior Province, Canada. *Geology*, *17*(1), 23-25.

Phinney, W.C., and Morrison, D.A., (1988). Constraints on the environment of Matachewan dike intrusion. Abstract IGCP-257, International Symposium on Mafic Dikes and Related Magmatism, University of Lund, Sweden

Popova, A. N. (2017). Crystallographic analysis of graphite by X-Ray diffraction. *Coke and Chemistry*, *60*(9), 361–365.

Qing, J., Richards, V. L., & Van Aken, D. C. (2017). Growth stages and hexagonal-rhombohedral structural arrangements in spheroidal graphite observed in ductile iron. *Carbon*, *116*, 456-469.

RPA Inc., (2014). Technical Report on the Albany Graphite Deposit, Northern Ontario, Canada, prepared for Zenyatta Ventures Ltd., filed at www.sedar.com

RPA Inc., (2015). Technical Report on the Preliminary economic assessment of the Albany graphite project, northern Ontario, Canada, prepared for Zenyatta Ventures Ltd., filed at www.sedar.com

Robinson, G. R., Hammarstrom, J. M., & Olson, D. W. (2017). Graphite. U.S. Geological Survey Professional Paper 1802-J. *U.S. Geological Survey*, *1*, 797.

Rosing-Schow, N., Bagas, L., Kolb, J., Balić-Žunić, T., Korte, C., & Fiorentini, M. L. (2017). Hydrothermal flake graphite mineralisation in Paleoproterozoic rocks of south-east Greenland. *Mineralium Deposita*, *52*(5), 769–789.

Rumble, D. (2014). Hydrothermal graphitic carbon. *Elements*, *10*(6), 427-433.

Rumble III., D., & Hoering, T. C. (1986). Carbon isotope geochemistry of graphite vein deposits from New Hampshire, U.S.A. *Geochimica et Cosmochimica Acta*, *50*(6), 1239–1247.

Rumble III., D., Ferry, J. M., Hoering, T. C., & Boucot, A. J. (1982). Fluid flow during metamorphism at the Beaver Brook fossil locality, New Hampshire. *American Journal of Science*, *282*(6), 886-919.

Sage, R. P. (1988). Geology of carbonatite-alkalic rock complexes in Ontario: Cargill Township carbonatite complex, district of Cochrane (No. 36). Ontario Ministry of Northern Development and Mines.

Simandl, G. J., Paradis, S., & Akam, C. (2015). Graphite deposit types, their origin, and economic significance. *British Columbia Ministry of Energy and Mines & British Columbia Geological Survey*, *3*, 163-171.

Spence, H.S. (1920) Graphite. Department of Mines, Canada, Publication No. 511, 250.

Sun, X., Ren, Y., Li, J., Huang, M., Sun, Z., Li, Z. (2022). Magma Evolution and Constraints on the Graphite Mineralization Hosted by the Huangyangshan Alkaline Granite Suite in the East Junggar of Xinjiang Province: Evidence from In Situ Analyses of Silicate Minerals. *Minerals*, *12*(11), 1458.

Stone, D., Tomlinson, K.Y., Davis, D.W., Fralick, P., Hall., J., Percival, J.A., Pufahl, P. (2002). Geology and tectonostratigraphic assemblages, South–central Wabigoon Subprovince. Ontario Geological Survey, Preliminary Map P.3448 (also Geological Survey of Canada, Open File 4284), scale: 1:250 000.

Stott, G.M., (2008). Precambrian geology of the Hudson Bay and James Bay lowlands region interpreted from aeromagnetic data – south sheet. Ontario Geological Survey, Preliminary Map P.3599, scale 1:500,000.

Stott, G.M., (2011). A revised terrane subdivision of the Superior Province in Ontario; Ontario Geological Survey, Miscellaneous Release—Data 278.

Taner, M. F., Drever, C., Yakymchuk, C., & Longstaffe, F. J. (2017). Origin of graphite in the southwestern Grenville Province. *The Canadian Mineralogist*, *55*(6), 1041-1055.

Touret, J. L., Huizenga, J. M., Kehelpannala, K. W., & Piccoli, F. (2019). Vein-type graphite deposits in Sri Lanka: The ultimate fate of granulite fluids. *Chemical geology*, *508*, 167-181.

Weis, P. L., Friedman, I., & Gleason, J. P. (1981). The origin of epigenetic graphite: evidence from isotopes. *Geochimica et Cosmochimica Acta*, *45*(12), 2325-2332.

West S. M., (2016). Supergene Alteration of the Albany Graphite Deposit [Bachelor dissertation, LakeheadUniversity] https://www.lakeheadu.ca/programs/departments/geology/about/msc-theses/summaries/ node/31934

Whitney, D. L., & Evans, B. W. (2010). Abbreviations for names of rock-forming minerals. *American mineralogist*, *95*(1), 185-187.

Yaya, A., Agyei-Tuffour, B., Dodoo-Arhin, D., Nyankson, E., Annan, E., Konadu, D. S., Sinayobye, E., Baryeh, E. A., & Ewels, C. P. (2012). Layered Nanomaterials-A Review. *Global Journal of Engineering, Design & Technology, 1* (2), 32-41.

Zaleski, E., van Breemen, O., & Peterson, V. L. (1999). Geological evolution of the Manitouwadge greenstone belt and Wawa-Quetico subprovince boundary, Superior Province, Ontario, constrained by U-Pb zircon dates of supracrustal and plutonic rocks. *Canadian Journal of Earth Sciences*, *36*(6), 945-966.

APPENDICES

1. Feldspars

		Zen 2-GP-32	Zen 2-GP-32	Zen 2-GP-32	Zen 2-GP-32	Zen 10-GP-107	Zen 10-GP-107	Zen 10-GP-107
Wt.%								
	SiO_2	64.58	64.11	62.46	62.77	64.26	63.42	64.26
	TiO_2	-	-	-	-	-	-	-
	Al_2O_3	18.64	18.66	18.62	18.66	18.87	18.34	18.5
	FeO	0.30	-	-	-	-	0.72	-
	MgO	-	-	-	-	-	-	-
	BaO	0.88	0.56	-	-	-	-	-
	CaO	-	-	-	-	-	-	-
	Na_2O	0.74	1.60	1.26	1.03	-	0.49	-
	K_2O	15.3	14.54	15.75	15.78	16.77	16.03	16.62
	Total	**100.44**	**99.47**	**98.09**	**98.24**	**99.90**	**99.00**	**99.38**
Structural formulae calculated on the basis of 32 oxygens								
a.p.f.u.								
	Si	11.93	11.91	11.82	11.84	11.92	11.90	11.97
	Ti	-	-	-	-	-	-	-
	Al	4.06	4.09	4.15	4.15	4.12	4.06	4.06
	Fe	0.05	-	-	-	-	0.11	-
	Mg	-	-	-	-	-	-	-
	Ba	0.06	0.04	-	-	-	-	-
	Ca	-	-	-	-	-	-	-
	Na	0.27	0.58	0.46	0.38	-	0.18	-
	K	3.61	3.45	3.80	3.80	3.97	3.84	3.95
	Total	**19.97**	**20.06**	**20.24**	**20.17**	**20.01**	**20.08**	**19.98**
Dash (-) - indicates values are b.d. limits								

		Zen 10-GP-107	Zen 10-GP-107	Zen 10-GP-107	Zen 10-GP-107	Zen 10-GP-107	Zen 10-GP-107	Zen 10-GP-107
Wt.%								
	SiO_2	61.81	63.15	65.09	64.23	64.12	65.06	66.04
	TiO_2	-	-	-	-	-	-	-
	Al_2O_3	22.07	19.12	18.65	18.96	19.36	18.45	18.96
	FeO	2.26	-	-	-	-	0.54	-
	MgO	-	-	-	-	-	0.42	-
	BaO	-	1.15	-	-	-	-	-
	CaO	-	-	-	-	-	-	-
	Na_2O	0.68	0.38	-	0.35	-	0.54	-
	K_2O	12.14	16	17.15	16.58	16.86	16.58	16.36
	Total	**98.96**	**99.8**	**100.89**	**100.12**	**100.34**	**101.59**	**101.36**
Structural formulae calculated on the basis of 32 oxygens								
a.p.f.u.								
	Si	11.44	11.81	11.96	11.89	11.85	11.90	12.01
	Ti	-	-	-	-	-	-	-
	Al	4.81	4.21	4.04	4.14	4.21	3.98	4.06
	Fe	0.35	-	-	-	-	0.08	-
	Mg	-	-	-	-	-	0.11	-
	Ba	-	0.08	-	-	-	-	-
	Ca	-	-	-	-	-	-	-
	Na	0.24	0.14	-	0.13	-	0.19	-
	K	2.87	3.82	4.02	3.91	3.97	3.87	3.79
	Total	**19.71**	**20.06**	**20.03**	**20.06**	**20.03**	**20.14**	**19.86**
Dash (-) - indicates values are b.d. limits								

		Zen 2-GP-21	**Zen 2-GP-21**	**Zen 2-GP-21**	**Zen 2-GP-21**	**Zen 2-GP-21**	**Zen 2-GP-21**	**Zen 2-GP-21**
Wt.%								
	SiO_2	63.16	63.91	63.54	64.07	66.32	64.16	65.24
	TiO_2	-	-	-	-	-	-	-
	Al_2O_3	17.79	17.86	17.70	17.86	18.43	17.76	18.38
	FeO	-	-	-	1.05	-	0.91	-
	MgO	-	-	-	0.87	-	-	-
	BaO	-	0.63	-	-	-	-	-
	CaO	-	-	-	-	-	-	-
	Na_2O	0.88	0.57	0.65	0.39	-	1.01	1.18
	K_2O	15.26	15.36	15.83	14.76	15.86	15.30	15.03
	Total	**97.09**	**98.33**	**97.72**	**99.00**	**100.61**	**99.14**	**99.83**
Structural formulae calculated on the basis of 32 oxygens								
a.p.f.u.								
	Si	12.01	12.03	12.02	11.94	12.10	11.99	12.02
	Ti	-	-	-	-	-	-	-
	Al	3.99	3.96	3.95	3.92	3.96	3.91	3.99
	Fe	-	-	-	0.16	-	0.14	-
	Mg	-	-	-	0.24	-	-	-
	Ba	-	0.05	-	-	-	-	-
	Ca	-	-	-	-	-	-	-
	Na	0.32	0.21	0.24	0.14	-	0.37	0.42
	K	3.70	3.69	3.82	3.51	3.69	3.65	3.53
	Total	**20.01**	**19.94**	**20.03**	**19.92**	**19.76**	**20.06**	**19.96**
Dash (-) - indicates values are b.d. limits								

		Zen 2-GP-21	Zen 2-GP-21	Zen 2-GP-21	Zen 26-GP-09	Zen 26-GP-09	Zen 26-GP-09	Zen 26-GP-09
Wt.%								
	SiO_2	64.34	64.34	64.71	64.79	62.96	65.31	63.45
	TiO_2	-	-	-	-	-	-	-
	Al_2O_3	18.22	18.33	17.71	18.18	17.86	18.03	19.04
	FeO	-	-	-	-	1.92	-	0.73
	MgO	-	-	-	-	0.6	-	1.41
	BaO	1.07	0.78	-	-	-	-	-
	CaO	-	-	-	-	-	-	-
	Na_2O	1.38	3.05	0.65	-	0.66	1.01	-
	K_2O	14.79	11.84	15.63	16.9	14.51	15.38	15.08
	Total	**99.80**	**98.34**	**98.70**	**99.87**	**98.51**	**99.73**	**99.71**
Structural formulae calculated on the basis of 32 oxygens								
a.p.f.u.								
	Si	11.96	11.98	12.09	12.02	11.86	12.06	11.74
	Ti	-	-	-	-	-	-	-
	Al	3.99	4.02	3.90	3.97	3.96	3.92	4.15
	Fe	-	-	-	-	0.30	-	0.11
	Mg	-	-	-	-	0.17	-	0.39
	Ba	0.08	0.06	-	-	-	-	-
	Ca	-	-	-	-	-	-	-
	Na	0.50	1.10	0.24	-	0.24	0.36	-
	K	3.51	2.81	3.72	4.00	3.49	3.62	3.56
	Total	**20.04**	**19.97**	**19.94**	**19.99**	**20.02**	**19.97**	**19.96**
Dash (-) - indicates values are b.d. limits								

		Zen 26-GP-09	Zen 26-GP-09	Zen 26-GP-09	Zen 26-GP-09	Zen 26-GP-09	Zen 26-GP-09	Zen 26-GP-09
Wt.%								
	SiO_2	63.01	64.96	63.43	65.44	62.8	63.54	63.39
	TiO_2	-	-	-	-	-	-	-
	Al_2O_3	19.15	18.43	18.87	18.19	19.37	19.13	18.98
	FeO	-	-	0.42	-	0.37	-	-
	MgO	-	-	-	-	-	-	-
	BaO	-	-	-	-	-	-	-
	CaO	-	-	-	-	-	-	-
	Na_2O	0.86	0.73	-	0.81	-	0.72	-
	K_2O	16.11	15.45	16.98	15.38	17.20	16.45	17.59
	Total	**99.13**	**99.57**	**99.70**	**99.82**	**99.74**	**99.84**	**99.96**
Structural formulae calculated on the basis of 32 oxygens								
a.p.f.u.								
	Si	11.79	12.01	11.84	12.06	11.74	11.82	11.82
	Ti	-	-	-	-	-	-	-
	Al	4.22	4.02	4.15	3.95	4.27	4.19	4.17
	Fe	-	-	0.07	-	0.06	-	-
	Mg	-	-	-	-	-	-	-
	Ba	-	-	-	-	-	-	-
	Ca	-	-	-	-	-	-	-
	Na	0.31	0.26	-	0.29	-	0.26	-
	K	3.85	3.64	4.04	3.62	4.10	3.90	4.19
	Total	**20.17**	**19.93**	**20.10**	**19.92**	**20.17**	**20.17**	**20.18**

Dash (-) - indicates values are b.d. limits

		Zen 26-GP-09	Zen 26-GP-09	Zen 26-GP-09	Zen 26-GP-09	Zen 27-GP-63	Zen 27-GP-63	Zen 27-GP-63
Wt.%								
	SiO_2	64.39	65	66.21	65.66	62.22	62.24	62.99
	TiO_2	-	-	-	-	-	-	-
	Al_2O_3	18.52	18.13	17.55	17.7	18.61	18.22	18.95
	FeO	-	-	-	-	-	-	-
	MgO	-	-	-	-	-	-	-
	BaO	-	-	-	-	-	0.50	0.60
	CaO	-	-	-	-	-	-	-
	Na_2O	-	-	-	-	2.54	0.92	1.07
	K_2O	17.34	17.06	16.66	16.57	12.72	15.45	15.85
	Total	**100.25**	**100.19**	**100.42**	**99.93**	**96.09**	**97.33**	**99.46**
Structural formulae calculated on the basis of 32 oxygens								
a.p.f.u.								
	Si	11.94	12.03	12.17	12.13	11.86	11.88	11.80
	Ti	-	-	-	-	-	-	-
	Al	4.05	3.95	3.80	3.85	4.18	4.10	4.18
	Fe	-	-	-	-	-	-	-
	Mg	-	-	-	-	-	-	-
	Ba	-	-	-	-	-	0.04	0.04
	Ca	-	-	-	-	-	-	-
	Na	-	-	-	-	0.94	0.34	0.39
	K	4.10	4.03	3.91	3.91	3.09	3.76	3.79
	Total	**20.09**	**20.01**	**19.88**	**19.89**	**20.07**	**20.12**	**20.20**

Dash (-) - indicates values are b.d. limits

		Zen 27-GP-63	Zen 27-GP-63	Zen 27-GP-63	Zen 27-GP-63	Zen 27-GP-63	Zen 27-GP-63	Zen 27-GP-63
Wt.%								
	SiO_2	64.67	65.77	62.81	63.19	63.66	62.66	63.60
	TiO_2	-	-	-	-	-	-	-
	Al_2O_3	18.45	17.96	19.29	19.22	19.16	19.15	19.68
	FeO	-	-	-	-	-	-	-
	MgO	-	-	-	-	-	-	-
	BaO	1.00	0.50	0.83	1.05	-	-	0.65
	CaO	-	-	-	-	-	-	-
	Na_2O	1.04	0.94	0.94	0.31	0.76	1.10	1.11
	K_2O	15.09	15.24	15.97	16.89	16.53	16.15	15.78
	Total	**100.25**	**100.41**	**99.84**	**100.66**	**100.11**	**99.06**	**100.82**
Structural formulae calculated on the basis of 32 oxygens								
a.p.f.u.								
	Si	11.96	12.09	11.74	11.77	11.81	11.76	11.74
	Ti	-	-	-	-	-	-	-
	Al	4.02	3.89	4.25	4.22	4.19	4.23	4.28
	Fe	-	-	-	-	-	-	-
	Mg	-	-	-	-	-	-	-
	Ba	0.07	0.04	0.06	0.08	-	-	0.05
	Ca	-	-	-	-	-	-	-
	Na	0.37	0.33	0.34	0.11	0.27	0.40	0.40
	K	3.56	3.57	3.81	4.01	3.91	3.87	3.71
	Total	**19.99**	**19.92**	**20.21**	**20.19**	**20.19**	**20.26**	**20.18**
Dash (-) - indicates values are b.d. limits								

		Zen 29-GP-32	Zen 29-GP-32	Zen 10-GP-116	Zen 10-GP-116	Zen 10-GP-116	Zen 10-GP-116
Wt.%							
	SiO_2	65.28	63.85	64.9	64.36	64.18	64.19
	TiO_2	-	-	-	-	-	-
	Al_2O_3	19.09	17.85	17.63	18.14	17.9	18.49
	FeO	-	-	-	-	-	-
	MgO	-	-	-	-	-	-
	BaO	-	-	-	-	-	-
	CaO	-	-	-	-	-	-
	Na_2O	0.54	1.16	-	-	-	-
	K_2O	15.77	14.84	17.22	17.37	17.44	17.3
	Total	**100.68**	**97.7**	**99.75**	**99.87**	**99.52**	**99.98**
Structural formulae calculated on the basis of 32 oxygens							
a.p.f.u.							
	Si	11.94	12.03	12.08	11.98	12.00	11.94
	Ti	-	-	-	-	-	-
	Al	4.12	3.96	3.87	3.98	3.94	4.05
	Fe	-	-	-	-	-	-
	Mg	-	-	-	-	-	-
	Ba	-	-	-	-	-	-
	Ca	-	-	-	-	-	-
	Na	0.19	0.42	-	-	-	-
	K	3.68	3.57	4.09	4.13	4.16	4.10
	Total	**19.93**	**19.98**	**20.03**	**20.09**	**20.11**	**20.09**

Dash (-) - indicates values are b.d. limits

		Zen 2-GP-32	**Zen 2-GP-32**	**Zen 2-GP-32**	**Zen 2-GP-32**	**Zen 10-GP-107**	**Zen 10-GP-107**	**Zen 10-GP-107**
Wt.%								
	SiO_2	67.93	65.81	62.87	62.70	66.13	60.95	67.82
	TiO_2	-	-	-	-	-	-	-
	Al_2O_3	20.57	21.90	21.29	22.94	20.10	24.00	19.76
	FeO	0.38	-	-	-	-	-	-
	MgO	-	-	-	-	-	-	-
	BaO	-	-	-	-	-	-	-
	CaO	0.93	2.41	1.97	5.22	1.20	5.36	0.54
	Na_2O	11.11	10.25	9.98	8.73	9.86	8.46	11.31
	K_2O	0.16	0.16	-	0.42	0.21	0.19	-
	Total	**101.08**	**100.53**	**96.11**	**100.01**	**97.50**	**98.96**	**99.43**
Structural formulae calculated on the basis of 32 oxygens								
a.p.f.u.								
	Si	11.79	11.51	11.49	11.13	11.84	10.93	11.92
	Ti	-	-	-	-	-	-	-
	Al	4.21	4.51	4.58	4.80	4.24	5.07	4.09
	Fe	0.06	-	-	-	-	-	-
	Mg	-	-	-	-	-	-	-
	Ba	-	-	-	-	-	-	-
	Ca	0.17	0.45	0.39	0.99	0.23	1.03	0.10
	Na	3.74	3.48	3.53	3.00	3.42	2.94	3.85
	K	0.04	0.04	-	0.10	0.05	0.04	-
	Total	**20.00**	**19.99**	**19.99**	**20.02**	**19.78**	**20.02**	**19.96**

Dash (-) - indicates values are b.d. limits

		Zen 10-GP-107	Zen 10-GP-107	Zen 2-GP-21	Zen 2-GP-21	Zen 2-GP-21	Zen 2-GP-21	Zen 2-GP-21
Wt.%								
	SiO_2	68.8	63.35	62.85	62.95	64.02	59.51	64.02
	TiO_2	-	-	-	-	-	-	-
	Al_2O_3	20.06	23.24	21.89	21.68	22.4	23.25	21.61
	FeO	-	-	-	-	-	-	-
	MgO	-	-	-	-	-	-	-
	BaO	-	-	-	-	-	-	-
	CaO	0.28	9.13	3.87	3.39	3.9	5.96	3.27
	Na_2O	11.32	0.71	9.58	9.67	9.88	8.14	9.92
	K_2O	-	3.49	0.16	0.18	-	-	-
	Total	**100.46**	**99.92**	**98.35**	**97.87**	**100.2**	**96.86**	**98.82**
Structural formulae calculated on the basis of 32 oxygens								
a.p.f.u.								
	Si	11.94	11.23	11.30	11.36	11.29	10.92	11.42
	Ti	-	-	-	-	-	-	-
	Al	4.10	4.86	4.64	4.61	4.66	5.03	4.54
	Fe	-	-	-	-	-	-	-
	Mg	-	-	-	-	-	-	-
	Ba	-	-	-	-	-	-	-
	Ca	0.05	1.73	0.75	0.66	0.74	1.17	0.63
	Na	3.81	0.24	3.34	3.38	3.38	2.90	3.43
	K	-	0.79	0.04	0.04	-	-	-
	Total	**19.91**	**18.86**	**20.07**	**20.05**	**20.07**	**20.01**	**20.02**
Dash (-) - indicates values are b.d. limits								

		Zen 2-GP-21	Zen 2-GP-21	Zen 2-GP-21	Zen 2-GP-21	Zen 26-GP-09	Zen 26-GP-09	Zen 26-GP-09
Wt.%								
	SiO_2	65.17	62.70	64.30	60.94	58.00	60.68	61.90
	TiO_2	-	-	-	-	-	-	-
	Al_2O_3	21.94	22.56	21.23	24.66	26.36	24.47	23.53
	FeO	-	-	0.39	0.40	-	-	0.28
	MgO	-	-	-	-	-	-	-
	BaO	-	-	-	-	-	-	-
	CaO	3.35	4.42	2.74	5.42	8.18	5.10	4.03
	Na_2O	9.80	9.05	10.14	8.26	7.16	8.72	8.95
	K_2O	-	-	-	0.24	0.16	-	0.27
	Total	**100.26**	**98.73**	**98.80**	**99.92**	**99.86**	**98.97**	**98.96**
Structural formulae calculated on the basis of 32 oxygens								
a.p.f.u.								
	Si	11.45	11.22	11.48	10.85	10.40	10.88	11.08
	Ti	-	-	-	-	-	-	-
	Al	4.54	4.76	4.47	5.17	5.57	5.17	4.96
	Fe	-	-	0.06	0.06	-	-	0.04
	Mg	-	-	-	-	-	-	-
	Ba	-	-	-	-	-	-	-
	Ca	0.63	0.85	0.52	1.03	1.57	0.98	0.77
	Na	3.34	3.14	3.51	2.85	2.49	3.03	3.11
	K	-	-	-	0.05	0.04	-	0.06
	Total	**19.95**	**19.97**	**20.04**	**20.02**	**20.07**	**20.05**	**20.02**

Dash (-) - indicates values are b.d. limits

		Zen 26-GP-09	Zen 26-GP-09	Zen 26-GP-09	Zen 26-GP-09	Zen 26-GP-09	Zen 27-GP-63	Zen 27-GP-63
Wt.%								
	SiO_2	59.18	66.20	64.58	67.07	66.65	66.54	65.16
	TiO_2	-	-	-	-	-	-	-
	Al_2O_3	26.07	20.37	21.56	20.74	20.6	20.07	21.27
	FeO	-	-	-	-	-	-	-
	MgO	-	-	-	-	-	-	-
	BaO	-	-	-	-	-	-	-
	CaO	6.41	0.25	2.03	0.45	1.69	1.06	1.54
	Na_2O	7.76	11.25	9.63	10.73	10.76	10.78	10.23
	K_2O	0.60	0.42	0.24	0.27	-	0.19	-
	Total	**100.02**	**98.49**	**98.04**	**99.26**	**99.70**	**98.64**	**98.20**
Structural formulae calculated on the basis of 32 oxygens								
a.p.f.u.								
	Si	10.57	11.78	11.55	11.80	11.72	11.81	11.62
	Ti	-	-	-	-	-	-	-
	Al	5.49	4.27	4.54	4.30	4.27	4.20	4.47
	Fe	-	-	-	-	-	-	-
	Mg	-	-	-	-	-	-	-
	Ba	-	-	-	-	-	-	-
	Ca	1.23	0.05	0.39	0.08	0.32	0.20	0.29
	Na	2.69	3.88	3.34	3.66	3.67	3.71	3.54
	K	0.14	0.10	0.05	0.06	-	0.04	-
	Total	**20.10**	**20.07**	**19.88**	**19.91**	**19.98**	**19.97**	**19.92**

Dash (-) - indicates values are b.d. limits

		Zen 27-GP-63	**Zen 27-GP-63**	**Zen 27-GP-63**	**Zen 27-GP-63**	**Zen 27-GP-63**	**Zen 27-GP-63**	**Zen 27-GP-63**
Wt.%								
	SiO_2	64.43	67.71	63.10	62.64	66.42	68.33	67.72
	TiO_2	-	-	-	-	-	-	-
	Al_2O_3	19.28	20.58	16.68	21.31	20.98	20.64	20.27
	FeO	-	-	1.38	1.61	-	-	0.26
	MgO	-	-	0.65	0.93	-	-	-
	BaO	-	-	-	-	-	-	-
	CaO	0.98	0.88	3.40	3.63	0.73	0.98	0.19
	Na_2O	9.57	10.53	9.03	8.88	10.71	10.78	11.41
	K_2O	-	0.28	2.82	0.90	0.21	0.23	0.43
	Total	**94.26**	**99.98**	**97.06**	**99.90**	**99.05**	**100.96**	**100.28**
Structural formulae calculated on the basis of 32 oxygens								
a.p.f.u.								
	Si	11.90	11.83	11.74	11.21	11.73	11.83	11.84
	Ti	-	-	-	-	-	-	-
	Al	4.20	4.24	3.66	4.50	4.37	4.21	4.18
	Fe	-	-	0.21	0.24	-	-	0.04
	Mg	-	-	0.18	0.25	-	-	-
	Ba	-	-	-	-	-	-	-
	Ca	0.19	0.16	0.68	0.70	0.14	0.18	0.04
	Na	3.43	3.57	3.26	3.08	3.67	3.62	3.87
	K	-	0.06	0.67	0.21	0.05	0.05	0.10
	Total	**19.72**	**19.86**	**20.40**	**20.18**	**19.95**	**19.90**	**20.05**
Dash (-) - indicates values are b.d. limits								

		Zen 27-GP-63	Zen 27-GP-63	Zen 27-GP-63	Zen 29-GP-32	Zen 10-GP-116	Zen 10-GP-116	Zen 10-GP-116
Wt.%								
	SiO_2	66.12	66.90	68.43	61.24	65.61	67.80	65.65
	TiO_2	-	-	-	-	-	-	-
	Al_2O_3	20.26	20.93	18.43	21.49	20.63	20.45	19.77
	FeO	-	-	-	-	-	0.28	-
	MgO	-	-	-	-	-	-	-
	BaO	-	-	-	-	-	-	-
	CaO	1.44	0.85	1.37	3.72	0.61	-	-
	Na_2O	10.97	10.79	9.65	8.68	11.2	11.53	11.10
	K_2O	0.19	0.23	0.57	0.30	0.17	0.16	-
	Total	**98.98**	**99.70**	**98.45**	**95.43**	**98.22**	**100.22**	**96.52**
Structural formulae calculated on the basis of 32 oxygens								
a.p.f.u.								
	Si	11.73	11.74	12.12	11.32	11.71	11.84	11.87
	Ti	-	-	-	-	-	-	-
	Al	4.24	4.33	3.85	4.68	4.34	4.21	4.21
	Fe	-	-	-	-	-	0.04	-
	Mg	-	-	-	-	-	-	-
	Ba	-	-	-	-	-	-	-
	Ca	0.27	0.16	0.26	0.74	0.12	-	-
	Na	3.77	3.67	3.31	3.11	3.88	3.90	3.89
	K	0.04	0.05	0.13	0.07	0.04	0.04	-
	Total	**20.06**	**19.95**	**19.67**	**19.93**	**20.08**	**20.03**	**19.97**

Dash (-) - indicates values are b.d. limits

		Zen 10-GP-116	Zen 26-GP-105	Zen 26-GP-105	Zen 26-GP-105	Zen 26-GP-105	Zen 26-GP-105	Zen 26-GP-105
Wt.%								
	SiO_2	67.91	60.35	60.09	60.05	54.75	57.69	60.78
	TiO_2	-	-	-	-	-	-	-
	Al_2O_3	19.63	25.11	24.98	25.02	25.26	23.85	24.98
	FeO	-	-	-	-	-	0.34	-
	MgO	-	-	-	-	-	-	-
	BaO	-	-	-	-	-	-	-
	CaO	-	5.61	5.57	5.72	10.06	6.75	5.54
	Na_2O	10.89	8.29	8.55	8.31	8.27	10.28	8.49
	K_2O	-	-	0.27	0.24	0.84	0.96	-
	Total	**98.43**	**99.36**	**99.46**	**99.34**	**99.18**	**99.87**	**99.79**
Structural formulae calculated on the basis of 32 oxygens								
a.p.f.u.								
	Si	12.00	10.78	10.76	10.76	10.10	10.51	10.81
	Ti	-	-	-	-	-	-	-
	Al	4.09	5.29	5.27	5.28	5.49	5.12	5.24
	Fe	-	-	-	-	-	0.05	-
	Mg	-	-	-	-	-	-	-
	Ba	-	-	-	-	-	-	-
	Ca	-	1.07	1.07	1.10	1.99	1.32	1.06
	Na	3.73	2.87	2.97	2.89	2.96	3.63	2.93
	K	-	-	0.06	0.05	0.20	0.22	-
	Total	**19.82**	**20.01**	**20.12**	**20.07**	**20.73**	**20.86**	**20.03**

Dash (-) - indicates values are b.d. limits

		Zen 26-GP-105	**Zen 26-GP-105**	**Zen 26-GP-105**	**Zen 26-GP-105**	**Zen 26-GP-105**	**Zen 26-GP-105**	**Zen 26-GP-105**
Wt.%								
	SiO_2	55.99	53.29	60.68	55.61	61.79	60.18	61.88
	TiO_2	-	-	-	-	-	-	-
	Al_2O_3	22.87	22.7	25.17	22.77	24.08	24.75	23.87
	FeO	1.42	6.02	-	-	0.32	-	-
	MgO	1.48	2.01	-	-	-	-	-
	BaO	-	-	-	-	-	-	-
	CaO	8.38	6.76	5.49	5.99	4.54	5.61	5.48
	Na_2O	8.80	8.45	8.32	9.91	8.95	8.46	8.7
	K_2O	0.78	0.64	0.17	1.08	0.15	0.16	0.26
	Total	**99.72**	**99.87**	**99.83**	**95.36**	**99.83**	**99.16**	**100.19**
Structural formulae calculated on the basis of 32 oxygens								
a.p.f.u.								
	Si	10.31	10.00	10.79	10.58	10.98	10.79	10.97
	Ti	-	-	-	-	-	-	-
	Al	4.96	5.02	5.28	5.11	5.04	5.23	4.99
	Fe	0.22	0.94	-	-	0.05	-	-
	Mg	0.41	0.56	-	-	-	-	-
	Ba	-	-	-	-	-	-	-
	Ca	1.65	1.36	1.05	1.22	0.86	1.08	1.04
	Na	3.14	3.07	2.87	3.66	3.08	2.94	2.99
	K	0.18	0.15	0.04	0.26	0.03	0.04	0.06
	Total	**20.87**	**21.11**	**20.02**	**20.83**	**20.06**	**20.08**	**20.06**
Dash (-) - indicates values are b.d. limits								

		Zen 26-GP-105	Zen 26-GP-105	Zen 26-GP-105	Zen 26-GP-105	Zen 2-GP-21	Zen 26-GP-09
Wt.%							
	SiO_2	62.37	61.31	68.33	63.00	55.92	60.54
	TiO_2	-	-	-	-	-	-
	Al_2O_3	23.71	23.06	19.32	17.76	20.87	20.24
	FeO	-	-	0.35	2.72	0.49	-
	MgO	-	-	-	1.64	1.30	-
	BaO	-	-	-	-	11.64	4.68
	CaO	5.56	5.22	0.59	1.32	-	-
	Na_2O	8.58	8.65	11.66	9.23	0.47	0.96
	K_2O	0.22	0.21	0.21	0.96	10.79	14.26
	Total	**100.44**	**98.45**	**100.46**	**96.63**	**101.48**	**100.68**
Structural formulae calculated on the basis of 32 oxygens							
a.p.f.u.							
	Si	11.02	11.05	11.94	11.65	10.98	13.28
	Ti	-	-	-	-	-	-
	Al	4.94	4.90	3.98	3.87	4.83	5.23
	Fe	-	-	0.05	0.42	0.08	-
	Mg	-	-	-	0.45	0.38	-
	Ba	-	-	-	-	0.90	0.40
	Ca	1.05	1.01	0.11	0.26	-	-
	Na	2.94	3.02	3.95	3.31	0.18	0.41
	K	0.05	0.05	0.05	0.23	2.70	3.99
	Total	**20.00**	**20.03**	**20.07**	**20.19**	**20.05**	**23.31**
Dash (-) - indicates values are b.d. limits							

2. Carbonates

		Zen 2-GP-32	Zen 2-GP-32	Zen 2-GP-32	Zen 2-GP-32	Zen 2-GP-32	Zen 2-GP-32	Zen 2-GP-32
Wt.%								
	$FeCO_3$	0.97	1.10	1.48	1.26	1.40	2.13	3.81
	$MnCO_3$	1.02	0.79	0.99	0.62	-	0.97	2.50
	$MgCO_3$	-	-	-	-	-	-	-
	$CaCO_3$	94.44	94.67	82.73	87.14	88.44	85.68	90.19
	$SrCO_3$	-	-	-	-	-	-	-
	$BaCO_3$	-	-	-	-	-	-	-
	Total	**96.43**	**96.56**	**85.21**	**89.02**	**89.85**	**88.78**	**96.49**
Structural formulae calculated on the basis of 6 oxygens								
a.p.f.u.								
	Fe	0.05	0.06	0.09	0.07	0.08	0.12	0.21
	Mn	0.06	0.04	0.06	0.04	-	0.06	0.14
	Mg	-	-	-	-	-	-	-
	Ca	5.89	5.90	5.85	5.89	5.92	5.82	5.66
	Sr	-	-	-	-	-	-	-
	Ba	-	-	-	-	-	-	-
	Total	**6.00**	**6.00**	**6.00**	**6.00**	**6.00**	**6.00**	**6.00**

Dash (-) - indicates values are b.d. limits

		Zen 2-GP-32	**Zen 2-GP-32**	**Zen 2-GP-32**	**Zen 2-GP-32**	**Zen 2-GP-32**	**Zen 2-GP-32**	**Zen 2-GP-32**
Wt.%								
	$FeCO_3$	3.97	0.98	1.77	3.05	7.18	1.08	2.24
	$MnCO_3$	2.48	0.75	0.68	-	-	0.66	-
	$MgCO_3$	-	-	0.92	0.92	3.85	-	3.51
	$CaCO_3$	89.69	94.96	91.75	92.51	81.98	94.46	90.16
	$SrCO_3$	-	-	-	-	-	-	-
	$BaCO_3$	-	-	-	-	-	-	-
	Total	**96.14**	**96.69**	**95.12**	**96.48**	**93.01**	**96.20**	**95.91**
Structural formulae calculated on the basis of 6 oxygens								
a.p.f.u.								
	Fe	0.22	0.05	0.10	0.16	0.40	0.06	0.12
	Mn	0.14	0.04	0.04	-	-	0.04	-
	Mg	-	-	0.07	0.07	0.30	-	0.26
	Ca	5.65	5.91	5.80	5.77	5.30	5.91	5.62
	Sr	-	-	-	-	-	-	-
	Ba	-	-	-	-	-	-	-
	Total	**6.00**	**6.00**	**6.00**	**6.00**	**6.00**	**6.00**	**6.00**
Dash (-) - indicates values are b.d. limits								

		Zen 2-GP-32	Zen 2-GP-32	Zen 2-GP-32	Zen 2-GP-32	Zen 10-GP-107	Zen 10-GP-107	Zen 10-GP-107
Wt.%								
	$FeCO_3$	1.13	1.13	1.66	1.85	1.95	1.16	1.73
	$MnCO_3$	-	-	-	-	0.81	0.92	2.61
	$MgCO_3$	1.51	2.78	3.72	3.89	0.71	0.59	2.53
	$CaCO_3$	94.24	94.03	89.87	90.51	89.75	94.60	91.76
	$SrCO_3$	-	-	-	-	-	-	-
	$BaCO_3$	-	-	-	-	-	-	-
	Total	**96.88**	**97.94**	**95.26**	**96.26**	**93.22**	**97.27**	**98.63**
Structural formulae calculated on the basis of 6 oxygens								
a.p.f.u.								
	Fe	0.06	0.06	0.09	0.10	0.11	0.06	0.09
	Mn	-	-	-	-	0.05	0.05	0.14
	Mg	0.11	0.20	0.28	0.29	0.05	0.04	0.18
	Ca	5.83	5.74	5.63	5.61	5.79	5.85	5.59
	Sr	-	-	-	-	-	-	-
	Ba	-	-	-	-	-	-	-
	Total	**6.00**	**6.00**	**6.00**	**6.00**	**6.00**	**6.00**	**6.00**

Dash (-) - indicates values are b.d. limits

		Zen 10-GP-107	Zen 10-GP-107	Zen 2-GP-21	Zen 2-GP-21	Zen 2-GP-21	Zen 2-GP-21	Zen 2-GP-21
Wt.%								
	$FeCO_3$	1.10	2.00	-	-	-	-	0.64
	$MnCO_3$	2.07	4.02	2.85	2.77	1.31	2.04	1.25
	$MgCO_3$	0.86	2.15	-	-	-	-	-
	$CaCO_3$	92.21	91.67	92.76	91.59	94.49	93.73	95.17
	$SrCO_3$	-	-	-	-	-	-	-
	$BaCO_3$	-	-	-	-	-	-	-
	Total	**96.24**	**99.85**	**95.61**	**94.36**	**95.81**	**95.77**	**97.06**
Structural formulae calculated on the basis of 6 oxygens								
a.p.f.u.								
	Fe	0.06	0.10	-	-	-	-	0.03
	Mn	0.11	0.21	0.16	0.15	0.07	0.11	0.07
	Mg	0.06	0.15	-	-	-	-	-
	Ca	5.76	5.53	5.84	5.85	5.93	5.89	5.90
	Sr	-	-	-	-	-	-	-
	Ba	-	-	-	-	-	-	-
	Total	**6.00**	**6.00**	**6.00**	**6.00**	**6.00**	**6.00**	**6.00**

Dash (-) - indicates values are b.d. limits

		Zen 2-GP-21	Zen 10-GP-116	Zen 10-GP-116	Zen 10-GP-116	Zen 26-GP-105	Zen 26-GP-105	Zen 26-GP-105
Wt.%								
	$FeCO_3$	0.71	-	-	-	2.35	2.26	1.68
	$MnCO_3$	1.62	1.25	0.53	1.57	4.83	5.53	4.97
	$MgCO_3$	-	-	-	-	1.67	2.38	1.11
	$CaCO_3$	93.74	95.42	95.08	94.16	79.25	78.00	84.41
	$SrCO_3$	-	-	-	-	-	-	-
	$BaCO_3$	-	-	-	-	-	-	-
	Total	**96.07**	**96.67**	**95.62**	**95.73**	**88.11**	**88.17**	**92.17**
Structural formulae calculated on the basis of 6 oxygens								
a.p.f.u.								
	Fe	0.04	-	-	-	0.14	0.13	0.09
	Mn	0.09	0.07	0.03	0.09	0.29	0.33	0.28
	Mg	-	-	-	-	0.14	0.19	0.09
	Ca	5.87	5.93	5.97	5.91	5.44	5.34	5.53
	Sr	-	-	-	-	-	-	-
	Ba	-	-	-	-	-	-	-
	Total	**6.00**	**6.00**	**6.00**	**6.00**	**6.00**	**6.00**	**6.00**
Dash (-) - indicates values are b.d. limits								

		Zen 26-GP-105	Zen 26-GP-105	Zen 26-GP-105	Zen 26-GP-105	Zen 27-GP-63	Zen 27-GP-63
Wt.%							
	$FeCO_3$	1.53	1.58	1.95	1.39	0.92	0.84
	$MnCO_3$	9.19	5.46	6.06	6.56	1.12	0.79
	$MgCO_3$	0.90	2.03	1.69	1.26	-	-
	$CaCO_3$	78.86	81.27	82.38	87.96	95.48	96.26
	$SrCO_3$	-	-	-	-	-	-
	$BaCO_3$	-	-	-	-	-	-
	Total	**90.48**	**90.34**	**92.08**	**97.17**	**97.51**	**97.89**
Structural formulae calculated on the basis of 6 oxygens							
a.p.f.u.							
	Fe	0.09	0.09	0.11	0.07	0.05	0.04
	Mn	0.54	0.32	0.35	0.36	0.06	0.04
	Mg	0.07	0.16	0.13	0.09	-	-
	Ca	5.30	5.43	5.41	5.48	5.89	5.91
	Sr	-	-	-	-	-	-
	Ba	-	-	-	-	-	-
	Total	**6.00**	**6.00**	**6.00**	**6.00**	**6.00**	**6.00**

Dash (-) - indicates values are b.d. limits

		Zen 29-GP-32	**Zen 29-GP-32**	**Zen 29-GP-32**	**Zen 29-GP-32**	**Zen 29-GP-32**	**Zen 29-GP-32**	**Zen 29-GP-32**
Wt.%								
	$FeCO_3$	11.51	10.71	12.11	10.13	8.67	8.71	10.11
	$MnCO_3$	1.85	1.67	3.92	2.01	2.59	1.72	3.05
	$MgCO_3$	32.80	33.33	27.36	31.95	32.57	33.87	31.00
	$CaCO_3$	52.06	50.34	50.15	52.09	51.65	51.50	50.88
	$SrCO_3$	-	-	-	-	-	-	-
	$BaCO_3$	-	-	-	-	-	-	-
	Total	**98.22**	**96.04**	**93.54**	**96.17**	**95.49**	**95.80**	**95.04**
Structural formulae calculated on the basis of 6 oxygens								
a.p.f.u.								
	Fe	0.58	0.55	0.65	0.52	0.45	0.45	0.53
	Mn	0.09	0.09	0.21	0.10	0.14	0.09	0.16
	Mg	2.28	2.36	2.02	2.26	2.32	2.39	2.23
	Ca	3.05	3.00	3.12	3.11	3.10	3.07	3.08
	Sr	-	-	-	-	-	-	-
	Ba	-	-	-	-	-	-	-
	Total	**6.00**	**6.00**	**6.00**	**6.00**	**6.00**	**6.00**	**6.00**
Dash (-) - indicates values are b.d. limits								

		Zen 29-GP-32	Zen 29-GP-32	Zen 29-GP-32	Zen 29-GP-32	Zen 29-GP-32	Zen 29-GP-32
Wt.%							
	$FeCO_3$	10.16	9.90	10.09	10.21	9.40	10.13
	$MnCO_3$	2.46	2.30	2.54	2.67	2.35	2.30
	$MgCO_3$	33.70	33.77	32.59	31.69	32.43	32.28
	$CaCO_3$	54.43	52.65	51.15	51.45	52.86	51.57
	$SrCO_3$	-	-	-	-	-	-
	$BaCO_3$	-	-	-	-	-	-
	Total	**100.75**	**98.61**	**96.38**	**96.02**	**97.04**	**96.28**
Structural formulae calculated on the basis of 6 oxygens							
a.p.f.u.							
	Fe	0.50	0.50	0.52	0.53	0.48	0.52
	Mn	0.12	0.12	0.13	0.14	0.12	0.12
	Mg	2.28	2.33	2.30	2.25	2.27	2.28
	Ca	3.10	3.06	3.05	3.08	3.12	3.07
	Sr	-	-	-	-	-	-
	Ba	-	-	-	-	-	-
	Total	**6.00**	**6.00**	**6.00**	**6.00**	**6.00**	**6.00**

Dash (-) - indicates values are b.d. limits

3. Biotite

		Zen 2-GP-32	Zen 2-GP-32	Zen 2-GP-32	Zen 2-GP-32	Zen 2-GP-32	Zen 2-GP-32	Zen 2-GP-32
Wt.%								
	SiO_2	42.29	40.57	38.97	37.42	41.14	39.45	41.52
	TiO_2	0.34	-	0.93	2.91	2.32	2.88	-
	Al_2O_3	11.87	11.93	11.77	11.53	12.31	11.71	12.13
	FeO	17.75	17.9	17.96	19.51	20.38	20.36	20.02
	MnO	-	-	-	-	-	-	-
	MgO	16.59	15.32	15.65	12.93	13.89	12.99	16.21
	CaO	-	-	-	-	-	-	-
	Li_2O	-	-	-	-	-	-	-
	Na_2O	-	-	-	-	-	-	-
	K_2O	9.88	9.6	10.03	10.08	10.34	10.08	9.97
	F	2.88	2.32	2.17	-	-	-	-
	Cl	0.37	0.43	0.40	0.31	-	-	-
		101.97	**98.07**	**97.88**	**94.69**	**100.38**	**97.47**	**99.85**
	-O≡F	1.21	0.98	0.91	-	-	-	-
	-O≡Cl	0.08	0.10	0.09	0.07	-	-	-
	Total	**100.67**	**97.00**	**96.88**	**94.62**	**100.38**	**97.47**	**99.85**
Structural formulae calculated on the basis of 22 oxygens								
a.p.f.u.								
	Si	5.93	5.94	5.77	5.80	5.96	5.91	6.02
	Ti	0.04	-	0.10	0.34	0.25	0.32	-
	Al	1.96	2.06	2.05	2.11	2.10	2.07	2.07
	Fe	2.08	2.19	2.22	2.53	2.47	2.55	2.43
	Mn	-	-	-	-	-	-	-
	Mg	3.47	3.35	3.45	2.99	3.00	2.90	3.50
	Ca	-	-	-	-	-	-	-
	Li	-	-	-	-	-	-	-
	Na	-	-	-	-	-	-	-
	K	1.77	1.79	1.89	1.99	1.91	1.93	1.84
	F	1.28	0.98	0.91	-	-	-	-
	Cl	0.09	0.10	0.09	0.07	-	-	-
	OH	2.63	2.93	3.00	3.93	4.00	4.00	4.00
	Total	**19.25**	**19.33**	**19.49**	**19.76**	**19.69**	**19.69**	**19.87**

Dash (-) - indicates values are b.d. limits

		Zen 2-GP-32	Zen 2-GP-32	Zen 2-GP-32	Zen 2-GP-32	Zen 2-GP-32	Zen 2-GP-32	Zen 2-GP-32
Wt.%								
	SiO_2	41.16	41.09	37.90	37.51	38.61	38.65	36.44
	TiO_2	-	1.24	2.48	1.63	1.85	1.54	3.25
	Al_2O_3	11.73	11.93	11.48	11.4	11.54	11.38	11.32
	FeO	18.54	17.42	19.65	19.46	17.70	17.77	19.49
	MnO	-	-	-	-	-	-	-
	MgO	16.15	16.30	13.52	13.66	14.86	14.95	12.59
	CaO	-	-	-	-	-	-	-
	Li_2O	-	-	-	-	-	-	-
	Na_2O	-	-	-	-	-	-	-
	K_2O	9.95	10.17	10.04	9.96	10.01	10.17	9.78
	F	-	-	-	-	-	2.12	-
	Cl	-	-	0.51	0.57	0.30	0.31	0.41
		97.53	**98.15**	**95.58**	**94.19**	**94.87**	**96.89**	**93.28**
	-O≡F	-	-	-	-	-	0.89	-
	-O≡Cl	-	-	0.12	0.13	0.07	0.07	0.19
	Total	**97.53**	**98.15**	**95.46**	**94.06**	**94.80**	**95.93**	**93.09**
Structural formulae calculated on the basis of 22 oxygens								
a.p.f.u.								
	Si	6.08	6.01	5.82	5.85	5.90	5.79	5.75
	Ti	-	0.14	0.29	0.19	0.21	0.17	0.39
	Al	2.04	2.06	2.08	2.09	2.08	2.01	2.10
	Fe	2.29	2.13	2.52	2.54	2.26	2.22	2.57
	Mn	-	-	-	-	-	-	-
	Mg	3.56	3.55	3.10	3.18	3.38	3.34	2.96
	Ca	-	-	-	-	-	-	-
	Li	-	-	-	-	-	-	-
	Na	-	-	-	-	-	-	-
	K	1.87	1.90	1.97	1.98	1.95	1.94	1.97
	F	-	-	-	-	-	0.89	-
	Cl	-	-	0.12	0.13	0.07	0.07	0.19
	OH	4.00	4.00	3.88	3.87	3.93	3.04	3.81
	Total	**19.84**	**19.78**	**19.77**	**19.83**	**19.79**	**19.47**	**19.74**

Dash (-) - indicates values are b.d. limits

		Zen 2-GP-32	Zen 2-GP-32	Zen 2-GP-32	Zen 2-GP-32	Zen 2-GP-32	Zen 2-GP-32	Zen 2-GP-32
Wt.%								
	SiO_2	37.45	39.14	38.96	38.69	38.56	39.46	39.52
	TiO_2	3.08	2.74	2.41	2.71	2.80	1.67	1.81
	Al_2O_3	11.38	11.49	11.52	11.22	11.20	11.64	11.70
	FeO	20.25	19.95	19.88	20.22	20.30	19.52	19.97
	MnO	-	-	-	0.35	-	-	-
	MgO	12.60	13.02	13.28	13.04	13.03	14.09	13.84
	CaO	-	-	-	-	-	-	-
	Li_2O	-	-	-	-	-	-	-
	Na_2O	-	-	-	-	-	-	-
	K_2O	10.00	9.88	10.03	9.91	10.13	9.88	9.99
	F	-	2.00	2.04	-	-	-	-
	Cl	0.52	0.39	0.33	0.46	0.48	0.45	0.48
		95.28	**98.61**	**98.45**	**96.60**	**96.50**	**96.71**	**97.31**
	-O≡F	-	0.84	0.86	-	-	-	-
	-O≡Cl	0.23	0.18	0.15	0.21	0.22	0.20	0.22
	Total	**95.05**	**97.59**	**97.44**	**96.39**	**96.28**	**96.51**	**97.09**
Structural formulae calculated on the basis of 22 oxygens								
a.p.f.u.								
	Si	5.79	5.79	5.78	5.88	5.87	5.95	5.93
	Ti	0.36	0.31	0.27	0.31	0.32	0.19	0.20
	Al	2.08	2.00	2.01	2.01	2.01	2.07	2.07
	Fe	2.62	2.47	2.47	2.57	2.59	2.46	2.51
	Mn	-	-	-	-	-	-	-
	Mg	2.91	2.87	2.94	2.96	2.96	3.16	3.10
	Ca	-	-	-	-	-	-	-
	Li	-	-	-	-	-	-	-
	Na	-	-	-	-	-	-	-
	K	1.97	1.87	1.90	1.92	1.97	1.90	1.91
	F	-	0.84	0.86	-	-	-	-
	Cl	0.23	0.18	0.15	0.21	0.22	0.20	0.22
	OH	3.77	2.98	2.99	3.79	3.78	3.80	3.78
	Total	**19.73**	**19.31**	**19.37**	**19.70**	**19.72**	**19.72**	**19.72**

Dash (-) - indicates values are b.d. limits

		Zen 2-GP-32	**Zen 2-GP-32**	**Zen 2-GP-32**	**Zen 2-GP-32**	**Zen 2-GP-32**	**Zen 2-GP-32**	**Zen 2-GP-32**
Wt.%								
	SiO_2	38.92	39.29	38.93	39.18	39.95	39.11	38.95
	TiO_2	3.06	2.60	2.85	2.91	2.68	2.25	2.71
	Al_2O_3	11.51	11.29	11.17	11.42	11.48	11.53	11.56
	FeO	20.03	19.65	20.26	19.89	20.06	20.65	21.05
	MnO	-	-	-	-	-	-	-
	MgO	13.48	13.36	12.99	13.22	12.88	13.21	13.09
	CaO	-	-	-	-	-	-	-
	Li_2O	-	-	-	-	-	-	-
	Na_2O	-	-	-	-	-	-	-
	K_2O	9.94	9.99	10.27	10.22	10.06	10.33	10.03
	F	-	-	-	-	-	2.04	-
	Cl	0.24	0.36	0.37	0.24	0.41	0.44	0.49
		97.18	**96.54**	**96.84**	**97.08**	**97.52**	**99.56**	**97.88**
	-O≡F	-	-	-	-	-	0.86	-
	-O≡Cl	0.11	0.16	0.17	0.11	0.19	0.20	0.22
	Total	**97.07**	**96.38**	**96.67**	**96.97**	**97.33**	**98.50**	**97.66**
Structural formulae calculated on the basis of 22 oxygens								
a.p.f.u.								
	Si	5.86	5.94	5.90	5.90	5.98	5.77	5.86
	Ti	0.35	0.30	0.33	0.33	0.30	0.25	0.31
	Al	2.04	2.01	2.00	2.03	2.03	2.00	2.05
	Fe	2.52	2.48	2.57	2.51	2.51	2.55	2.65
	Mn	-	-	-	-	-	-	-
	Mg	3.02	3.01	2.94	2.97	2.87	2.91	2.93
	Ca	-	-	-	-	-	-	-
	Li	-	-	-	-	-	-	-
	Na	-	-	-	-	-	-	-
	K	1.91	1.93	1.99	1.96	1.92	1.94	1.92
	F	-	-	-	-	-	0.86	-
	Cl	0.11	0.16	0.17	0.11	0.19	0.20	0.22
	OH	3.89	3.84	3.83	3.89	3.81	2.94	3.78
	Total	**19.70**	**19.67**	**19.72**	**19.70**	**19.61**	**19.42**	**19.71**

Dash (-) - indicates values are b.d. limits

		Zen 2-GP-32	Zen 10-GP-107	Zen 10-GP-107	Zen 10-GP-107	Zen 10-GP-107	Zen 10-GP-107	Zen 10-GP-107
Wt.%								
	SiO_2	39.36	39.65	40.17	36.1	39.71	36.78	35.75
	TiO_2	2.37	0.79	1.37	1.70	1.84	1.91	1.28
	Al_2O_3	11.53	12.01	11.87	12.95	13.01	13.72	14.93
	FeO	20.51	17.94	19.38	21.13	17.33	18.86	17.15
	MnO	-	-	0.56	0.67	0.60	0.66	0.62
	MgO	13.66	14.87	13.71	11.16	14.86	12.74	13.11
	CaO	-	-	-	-	-	-	-
	Li_2O	-	-	-	-	-	-	-
	Na_2O	-	-	-	-	-	-	-
	K_2O	10.04	10.11	10.01	9.76	10.21	9.99	9.97
	F	-	-	2.17	-	-	-	-
	Cl	0.50	0.18	0.69	0.60	0.64	0.69	0.48
		97.97	**95.55**	**99.93**	**94.07**	**98.20**	**95.35**	**93.29**
	-O≡F	-	-	0.91	-	-	-	-
	-O≡Cl	0.23	0.08	0.31	0.27	0.29	0.31	0.22
	Total	**97.74**	**95.47**	**98.70**	**93.80**	**97.91**	**95.04**	**93.07**
Structural formulae calculated on the basis of 22 oxygens								
a.p.f.u.								
	Si	5.89	6.00	5.86	5.70	5.85	5.66	5.58
	Ti	0.27	0.09	0.15	0.20	0.20	0.22	0.15
	Al	2.03	2.14	2.04	2.41	2.26	2.49	2.75
	Fe	2.57	2.27	2.36	2.79	2.13	2.43	2.24
	Mn	-	-	0.07	0.09	0.07	0.09	0.08
	Mg	3.05	3.35	2.98	2.63	3.26	2.92	3.05
	Ca	-	-	-	-	-	-	-
	Li	-	-	-	-	-	-	-
	Na	-	-	-	-	-	-	-
	K	1.92	1.95	1.86	1.97	1.92	1.96	1.98
	F	-	-	0.91	-	-	-	-
	Cl	0.23	0.08	0.31	0.27	0.29	0.31	0.22
	OH	3.77	3.92	2.77	3.73	3.71	3.69	3.78
	Total	**19.72**	**19.80**	**19.32**	**19.79**	**19.70**	**19.77**	**19.83**

Dash (-) - indicates values are b.d. limits

		Zen 10-GP-107	**Zen 10-GP-107**	**Zen 2-GP-21**	**Zen 2-GP-21**	**Zen 2-GP-21**	**Zen 2-GP-21**	**Zen 2-GP-21**
Wt.%								
	SiO_2	40.10	39.60	36.67	37.46	34.73	34.71	34.13
	TiO_2	1.68	1.46	4.06	3.77	4.21	4.10	4.09
	Al_2O_3	12.55	12.13	12.62	11.58	14.37	14.48	14.42
	FeO	21.35	20.69	23.74	24.33	24.4	24.25	24.95
	MnO	0.48	0.51	0.95	0.70	0.87	0.72	0.62
	MgO	12.71	13.49	8.56	10.02	8.32	8.60	8.16
	CaO	-	-	-	-	-	-	-
	Li_2O	-	-	-	-	-	-	-
	Na_2O	-	-	-	-	-	-	-
	K_2O	10.40	9.38	9.69	9.49	9.54	9.42	9.51
	F	2.55	2.73	-	-	-	-	-
	Cl	0.59	0.53	0.42	0.33	0.26	0.37	0.35
		102.41	**100.52**	**96.71**	**97.68**	**96.7**	**96.65**	**96.23**
	-O≡F	1.07	1.15	-	-	-	-	-
	-O≡Cl	0.27	0.24	0.19	0.15	0.12	0.17	0.16
	Total	**101.07**	**99.13**	**96.52**	**97.53**	**96.58**	**96.48**	**96.07**
Structural formulae calculated on the basis of 22 oxygens								
a.p.f.u.								
	Si	5.76	5.75	5.69	5.75	5.42	5.41	5.37
	Ti	0.18	0.16	0.47	0.44	0.49	0.48	0.48
	Al	2.12	2.08	2.31	2.10	2.64	2.66	2.67
	Fe	2.56	2.51	3.08	3.12	3.18	3.16	3.28
	Mn	0.06	0.06	0.12	0.09	0.11	0.09	0.08
	Mg	2.72	2.92	1.98	2.29	1.93	2.00	1.91
	Ca	-	-	-	-	-	-	-
	Li	-	-	-	-	-	-	-
	Na	-	-	-	-	-	-	-
	K	1.90	1.74	1.92	1.86	1.90	1.87	1.91
	F	1.07	1.15	-	-	-	-	-
	Cl	0.27	0.24	0.19	0.15	0.12	0.17	0.16
	OH	2.66	2.61	3.81	3.85	3.88	3.83	3.84
	Total	**19.30**	**19.23**	**19.58**	**19.65**	**19.68**	**19.67**	**19.72**

Dash (-) - indicates values are b.d. limits

		Zen 2-GP-21	Zen 2-GP-21	Zen 2-GP-21	Zen 26-GP-09	Zen 26-GP-09	Zen 26-GP-09	Zen 26-GP-09
Wt.%								
	SiO_2	38.29	37.91	36.93	41.16	44.66	37.86	37.45
	TiO_2	3.56	3.66	4.11	0.64	0.57	3.42	3.21
	Al_2O_3	11.56	12.79	13.71	11.80	11.36	12.92	12.46
	FeO	20.69	21.27	21.20	17.85	16.44	21.23	22.04
	MnO	-	0.47	0.58	-	-	-	-
	MgO	11.45	11.47	10.68	15.47	14.19	12.47	11.34
	CaO	-	-	-	-	-	-	-
	Li_2O	-	-	-	-	-	-	-
	Na_2O	-	-	-	-	-	-	-
	K_2O	9.63	9.42	9.84	10.23	9.40	10.05	10.00
	F	-	-	-	3.43	3.03	-	-
	Cl	0.39	0.33	0.31	0.37	0.32	0.34	0.53
		95.57	**97.32**	**97.36**	**100.95**	**99.97**	**98.29**	**97.03**
	-O≡F	-	-	-	1.44	1.28	-	-
	-O≡Cl	0.18	0.15	0.14	0.17	0.14	0.15	0.24
	Total	**95.39**	**97.17**	**97.22**	**99.34**	**98.55**	**98.14**	**96.79**
Structural formulae calculated on the basis of 22 oxygens								
a.p.f.u.								
	Si	5.88	5.73	5.60	5.87	6.29	5.68	5.72
	Ti	0.41	0.42	0.47	0.07	0.06	0.39	0.37
	Al	2.09	2.28	2.45	1.98	1.89	2.28	2.24
	Fe	2.66	2.69	2.69	2.13	1.94	2.66	2.82
	Mn	-	0.06	0.07	-	-	-	-
	Mg	2.62	2.59	2.42	3.29	2.98	2.79	2.58
	Ca	-	-	-	-	-	-	-
	Li	-	-	-	-	-	-	-
	Na	-	-	-	-	-	-	-
	K	1.89	1.82	1.90	1.86	1.69	1.92	1.95
	F	-	-	-	1.44	1.28	-	-
	Cl	0.18	0.15	0.14	0.17	0.14	0.15	0.24
	OH	3.82	3.85	3.86	2.39	2.58	3.85	3.76
	Total	**19.55**	**19.58**	**19.61**	**19.19**	**18.84**	**19.71**	**19.69**

Dash (-) - indicates values are b.d. limits

		Zen 26-GP-09	Zen 26-GP-09	Zen 26-GP-09	Zen 26-GP-09	Zen 26-GP-09	Zen 26-GP-09	Zen 26-GP-09
Wt.%								
	SiO_2	38.25	37.88	38.94	38.43	39.33	38.69	38.77
	TiO_2	3.28	4.11	3.25	3.69	3.15	3.57	3.66
	Al_2O_3	12.74	12.55	12.23	11.92	11.31	12.21	13.06
	FeO	19.95	21.97	21.61	21.59	20.49	20.51	21.98
	MnO	-	-	-	-	-	-	-
	MgO	12.52	11.18	12.22	11.91	13.05	12.33	12.24
	CaO	-	-	-	-	-	-	-
	Li_2O	-	-	-	-	-	-	-
	Na_2O	-	-	-	-	-	-	-
	K_2O	10.2	10.22	10.15	10.10	10.24	10.11	10.15
	F	1.97	-	-	-	2.43	2.38	-
	Cl	0.48	0.39	0.39	0.37	-	0.42	0.47
		99.39	**98.3**	**98.79**	**98.01**	**100**	**100.22**	**100.33**
	-O≡F	0.83	-	-	-	1.02	1.00	-
	-O≡Cl	0.22	0.18	0.18	0.17	-	0.19	0.21
	Total	**98.34**	**98.12**	**98.61**	**97.84**	**98.98**	**99.03**	**100.12**
Structural formulae calculated on the basis of 22 oxygens								
a.p.f.u.								
	Si	5.64	5.71	5.81	5.79	5.75	5.66	5.70
	Ti	0.36	0.47	0.36	0.42	0.35	0.39	0.40
	Al	2.21	2.23	2.15	2.12	1.95	2.10	2.26
	Fe	2.46	2.77	2.70	2.72	2.51	2.51	2.70
	Mn	-	-	-	-	-	-	-
	Mg	2.75	2.51	2.72	2.67	2.85	2.69	2.68
	Ca	-	-	-	-	-	-	-
	Li	-	-	-	-	-	-	-
	Na	-	-	-	-	-	-	-
	K	1.92	1.96	1.93	1.94	1.91	1.89	1.90
	F	0.83	-	-	-	1.02	1.00	-
	Cl	0.22	0.18	0.18	0.17	-	0.19	0.21
	OH	2.95	3.82	3.82	3.83	2.98	2.81	3.79
	Total	**19.33**	**19.64**	**19.67**	**19.66**	**19.32**	**19.24**	**19.66**
Dash (-) - indicates values are b.d. limits								

		Zen 26-GP-09	**Zen 26-GP-09**	**Zen 26-GP-09**	**Zen 26-GP-09**	**Zen 26-GP-09**	**Zen 26-GP-09**	**Zen 26-GP-09**
Wt.%								
	SiO_2	37.41	41.40	52.20	55.78	52.27	52.70	54.04
	TiO_2	3.26	2.29	-	-	-	-	-
	Al_2O_3	13.12	11.45	10.33	9.78	9.54	11.02	12.19
	FeO	19.61	17.95	15.65	17.81	16.01	14.45	12.24
	MnO	-	-	-	-	-	-	-
	MgO	12.1	13.39	5.04	5.37	5.22	5.22	5.66
	CaO	-	-	-	-	-	-	-
	Li_2O	-	-	-	-	-	-	-
	Na_2O	-	-	-	-	-	-	-
	K_2O	10.05	9.74	7.39	7.46	7.60	7.45	7.62
	F	-	2.57	-	-	-	-	-
	Cl	0.37	0.45	-	-	-	-	-
		95.92	**99.24**	**90.61**	**96.20**	**90.64**	**90.84**	**91.75**
	-O≡F	-	1.08	-	-	-	-	-
	-O≡Cl	0.17	0.20	-	-	-	-	-
	Total	**95.75**	**97.95**	**90.61**	**96.20**	**90.64**	**90.84**	**91.75**
Structural formulae calculated on the basis of 22 oxygens								
a.p.f.u.								
	Si	5.71	5.99	7.76	7.84	7.80	7.76	7.76
	Ti	0.37	0.25	-	-	-	-	-
	Al	2.36	1.95	1.81	1.62	1.68	1.91	2.06
	Fe	2.50	2.17	1.95	2.09	2.00	1.78	1.47
	Mn	-	-	-	-	-	-	-
	Mg	2.75	2.89	1.12	1.13	1.16	1.15	1.21
	Ca	-	-	-	-	-	-	-
	Li	-	-	-	-	-	-	-
	Na	-	-	-	-	-	-	-
	K	1.96	1.80	1.40	1.34	1.45	1.40	1.40
	F	-	1.08	-	-	-	-	-
	Cl	0.17	0.20	-	-	-	-	-
	OH	3.83	2.71	4.00	4.00	4.00	4.00	4.00
	Total	**19.66**	**19.04**	**18.03**	**18.02**	**18.08**	**17.99**	**17.90**

Dash (-) - indicates values are b.d. limits

		Zen 26-GP-09	Zen 26-GP-09	Zen 26-GP-09	Zen 26-GP-09	Zen 26-GP-09	Zen 26-GP-09
Wt.%							
	SiO_2	54.91	54.74	57.02	54.94	55.3	55.99
	TiO_2	-	-	-	-	-	-
	Al_2O_3	11.93	11.16	10.96	11.36	13.54	11.09
	FeO	14.96	14.41	14.84	13.85	11.07	14.78
	MnO	-	-	-	-	-	-
	MgO	5.4	5.50	5.90	5.73	5.72	5.70
	CaO	-	-	-	-	-	-
	Li_2O	-	-	-	-	-	-
	Na_2O	-	-	-	-	-	-
	K_2O	7.7	7.70	7.96	7.77	7.75	7.69
	F	-	-	-	-	-	-
	Cl	-	-	-	-	-	-
		94.9	**93.51**	**96.68**	**93.65**	**93.38**	**95.25**
	-O≡F	-	-	-	-	-	-
	-O≡Cl	-	-	-	-	-	-
	Total	**94.90**	**93.51**	**96.68**	**93.65**	**93.38**	**95.25**
Structural formulae calculated on the basis of 22 oxygens							
a.p.f.u.							
	Si	7.72	7.80	7.86	7.80	7.74	7.83
	Ti	-	-	-	-	-	-
	Al	1.98	1.87	1.78	1.90	2.23	1.83
	Fe	1.76	1.72	1.71	1.64	1.29	1.73
	Mn	-	-	-	-	-	-
	Mg	1.13	1.17	1.21	1.21	1.19	1.19
	Ca	-	-	-	-	-	-
	Li	-	-	-	-	-	-
	Na	-	-	-	-	-	-
	K	1.38	1.40	1.40	1.41	1.38	1.37
	F	-	-	-	-	-	-
	Cl	-	-	-	-	-	-
	OH	4.00	4.00	4.00	4.00	4.00	4.00
	Total	**17.98**	**17.96**	**17.95**	**17.96**	**17.84**	**17.94**

Dash (-) - indicates values are b.d. limits

		Zen 26-GP-105	Zen 26-GP-105
Wt.%			
	SiO_2	36.73	38.02
	TiO_2	3.88	1.80
	Al_2O_3	14.31	12.54
	FeO	22.77	24.63
	MnO	-	-
	MgO	10.52	10.87
	CaO	-	-
	Li_2O	-	-
	Na_2O	-	-
	K_2O	10.00	9.14
	F	-	-
	Cl	-	0.37
		98.21	**97.37**
	-O≡F	-	-
	-O≡Cl	-	0.17
	Total	**98.21**	**97.20**
Structural formulae calculated on the basis of 22 oxygens			
a.p.f.u.			
	Si	5.55	5.81
	Ti	0.44	0.21
	Al	2.55	2.26
	Fe	2.88	3.15
	Mn	-	-
	Mg	2.37	2.48
	Ca	-	-
	Li	-	-
	Na	-	-
	K	1.93	1.78
	F	-	-
	Cl	-	0.17
	OH	4.00	3.83
	Total	**19.70**	**19.69**
Dash (-) - indicates values are b.d. limits			

		Zen 26-GP-105	**Zen 26-GP-105**	**Zen 26-GP-105**	**Zen 26-GP-105**	**Zen 26-GP-105**	**Zen 26-GP-105**	**Zen 26-GP-105**
Wt.%								
	SiO_2	41.78	45.66	42.21	44.61	44.24	43.74	42.78
	TiO_2	0.77	-	1.49	0.52	1.10	1.12	0.96
	Al_2O_3	11.22	11.62	12.07	11.52	12.01	12.56	12.86
	FeO	7.85	5.24	6.75	5.17	5.56	5.90	5.12
	MnO	-	-	-	-	-	-	-
	MgO	22.76	26.78	24.21	25.51	26.16	25.41	26.09
	CaO	-	-	-	-	-	-	-
	Li_2O	-	-	-	-	-	-	-
	Na_2O	-	-	-	-	-	-	-
	K_2O	10.43	10.63	10.76	10.10	10.65	11.12	10.72
	F	2.36	-	2.57	3.60	3.28	2.48	2.96
	Cl	0.14	0.13	-	-	-	-	-
		97.31	**100.06**	**100.06**	**101.03**	**103.00**	**102.33**	**101.49**
	-O≡F	0.99	-	1.08	1.52	1.38	1.04	1.25
	-O≡Cl	0.06	0.06	-	-	-	-	-
	Total	**96.25**	**100.00**	**98.98**	**99.51**	**101.62**	**101.29**	**100.24**
Structural formulae calculated on the basis of 22 oxygens								
a.p.f.u.								
	Si	5.91	6.16	5.78	5.95	5.83	5.83	5.72
	Ti	0.08	-	0.15	0.05	0.11	0.11	0.10
	Al	1.87	1.85	1.95	1.81	1.86	1.97	2.03
	Fe	0.93	0.59	0.77	0.58	0.61	0.66	0.57
	Mn	-	-	-	-	-	-	-
	Mg	4.80	5.39	4.94	5.08	5.14	5.04	5.20
	Ca	-	-	-	-	-	-	-
	Li	-	-	-	-	-	-	-
	Na	-	-	-	-	-	-	-
	K	1.88	1.83	1.88	1.72	1.79	1.89	1.83
	F	0.99	-	1.08	1.52	1.38	1.04	1.25
	Cl	0.06	0.06	-	-	-	-	-
	OH	2.94	3.94	2.92	2.48	2.62	2.96	2.75
	Total	**19.47**	**19.82**	**19.48**	**19.19**	**19.34**	**19.50**	**19.45**

Dash (-) - indicates values are b.d. limits

		Zen 26-GP-105	Zen 26-GP-105	Zen 26-GP-105	Zen 26-GP-105	Zen 26-GP-105	Zen 26-GP-105	Zen 27-GP-63
Wt.%								
	SiO_2	43.80	42.45	42.72	43.15	41.64	42.36	41.33
	TiO_2	1.46	1.52	0.93	1.29	1.33	1.23	0.96
	Al_2O_3	12.46	12.52	11.94	12.48	12.93	12.31	11.1
	FeO	5.13	6.75	6.31	6.71	7.49	6.61	20.43
	MnO	-	-	-	-	-	-	0.61
	MgO	25.88	24.71	24.84	25.00	24.86	24.29	14.44
	CaO	-	-	-	-	-	0.32	-
	Li_2O	-	-	-	-	-	0.81	-
	Na_2O	-	-	-	-	-	-	-
	K_2O	11.02	10.91	10.71	10.79	11.04	10.56	10.18
	F	2.58	2.92	2.93	3.24	2.63	-	3.12
	Cl	-	-	-	-	-	-	0.26
		102.33	**101.78**	**100.38**	**102.66**	**101.92**	**98.49**	**102.43**
	-O≡F	1.09	1.23	1.23	1.36	1.11	-	1.31
	-O≡Cl	-	-	-	-	-	-	0.12
	Total	**101.24**	**100.55**	**99.15**	**101.30**	**100.81**	**98.49**	**101.00**
Structural formulae calculated on the basis of 22 oxygens								
a.p.f.u.								
	Si	5.81	5.72	5.81	5.75	5.63	5.87	5.89
	Ti	0.15	0.15	0.10	0.13	0.14	0.13	0.10
	Al	1.95	1.99	1.91	1.96	2.06	2.01	1.86
	Fe	0.57	0.76	0.72	0.75	0.85	0.77	2.43
	Mn	-	-	-	-	-	-	0.07
	Mg	5.12	4.96	5.04	4.96	5.01	5.02	3.07
	Ca	-	-	-	-	-	0.05	-
	Li	-	-	-	-	-	0.45	-
	Na	-	-	-	-	-	-	-
	K	1.87	1.87	1.86	1.83	1.90	1.87	1.85
	F	1.09	1.23	1.23	1.36	1.11	-	1.31
	Cl	-	-	-	-	-	-	0.12
	OH	2.91	2.77	2.77	2.64	2.89	4.00	2.57
	Total	**19.46**	**19.45**	**19.44**	**19.38**	**19.59**	**20.16**	**19.27**

Dash (-) - indicates values are b.d. limits

		Zen 27-GP-63	Zen 27-GP-63	Zen 27-GP-63	Zen 26-GP-105	Zen 26-GP-105	Zen 26-GP-105	Zen 26-GP-105
Wt.%								
	SiO_2	40.26	40.74	41.64	39.5	39.94	40.39	40.23
	TiO_2	0.85	1.10	0.96	1.98	1.66	1.48	1.57
	Al_2O_3	11.04	10.71	11.29	13.01	13.06	12.76	12.07
	FeO	20.90	19.8	21.23	9.10	9.10	9.34	8.97
	MnO	-	0.47	-	-	-	-	-
	MgO	13.3	14.3	14.48	21.26	21.18	21.38	21.91
	CaO	-	-	-	-	-	-	-
	Li_2O	-	-	-	-	-	-	-
	Na_2O	-	-	-	-	-	-	-
	K_2O	10.17	10.48	10.55	10.64	10.55	10.72	10.58
	F	2.72	2.78	2.84	2.54	2.32	1.93	2.49
	Cl	0.37	0.23	0.37	0.14	0.12	-	-
		99.61	**100.61**	**103.36**	**98.17**	**97.93**	**98**	**97.82**
	-O≡F	1.15	1.17	1.20	1.07	0.98	0.81	1.05
	-O≡Cl	0.17	0.10	0.17	0.06	0.05	-	-
	Total	**98.30**	**99.34**	**102.00**	**97.04**	**96.90**	**97.19**	**96.77**
Structural formulae calculated on the basis of 22 oxygens								
a.p.f.u.								
	Si	5.92	5.91	5.89	5.60	5.66	5.73	5.71
	Ti	0.09	0.12	0.10	0.21	0.18	0.16	0.17
	Al	1.91	1.83	1.88	2.17	2.18	2.13	2.02
	Fe	2.57	2.40	2.51	1.08	1.08	1.11	1.06
	Mn	-	0.06	-	-	-	-	-
	Mg	2.91	3.09	3.05	4.49	4.48	4.52	4.64
	Ca	-	-	-	-	-	-	-
	Li	-	-	-	-	-	-	-
	Na	-	-	-	-	-	-	-
	K	1.91	1.94	1.90	1.92	1.91	1.94	1.92
	F	1.15	1.17	1.20	1.07	0.98	0.81	1.05
	Cl	0.17	0.10	0.17	0.06	0.05	-	-
	OH	2.69	2.73	2.64	2.87	2.97	3.19	2.95
	Total	**19.31**	**19.36**	**19.34**	**19.48**	**19.49**	**19.58**	**19.51**

Dash (-) - indicates values are b.d. limits

		Zen 26-GP-105	Zen 26-GP-105	Zen 26-GP-105	Zen 26-GP-105	Zen 26-GP-105	Zen 26-GP-105	Zen 26-GP-105
Wt.%								
	SiO_2	40.96	40.66	40.41	43.48	42.64	41.28	38.34
	TiO_2	1.12	1.47	1.39	0.68	0.71	0.78	1.78
	Al_2O_3	12.01	13.59	13.62	8.04	11.39	12.55	12.71
	FeO	8.99	6.07	6.38	7.58	5.53	5.28	7.92
	MnO	-	-	-	-	-	-	-
	MgO	21.84	24.3	23.92	23.25	24.61	25.24	22.37
	CaO	-	-	-	3.31	1.34	2.75	1.77
	K_2O	10.86	9.77	9.71	7.22	10.38	10.1	10.53
	SO_3	-	-	-	6.08	1.82	-	1.09
	BaO	-	2.85	4.03	-	-	0.59	-
	F	2.51	2.94	2.94	2.04	2.88	2.34	2.44
	Cl	-	0.16	0.16	-	0.16	-	0.12
	P_2O_5	-	-	-	-	1.13	1.01	1.73
	Cr_2O_3	-	-	-	-	0.29	0.66	0.59
		98.29	**101.81**	**102.56**	**101.68**	**102.88**	**102.58**	**101.39**
	-O≡F	1.06	1.24	1.24	0.86	1.21	0.99	1.03
	-O≡Cl	-	0.07	0.07	-	0.07	-	0.05
	Total	**97.23**	**100.50**	**101.25**	**100.82**	**101.60**	**101.59**	**100.31**
Structural formulae calculated on the basis of 22 oxygens								
a.p.f.u.								
	Si	5.78	5.73	5.71	5.80	5.77	5.66	5.36
	Ti	0.12	0.16	0.15	0.07	0.07	0.08	0.19
	Al	2.00	2.26	2.27	1.26	1.82	2.03	2.10
	Fe	1.06	0.71	0.75	0.84	0.63	0.61	0.93
	Mn	-	-	-	-	-	-	-
	Mg	4.60	5.10	5.04	4.62	4.96	5.16	4.67
	Ca	-	-	-	0.47	0.19	0.40	0.27
	Na	-	-	-	-	-	-	-
	K	1.96	1.76	1.75	1.23	1.79	1.77	1.88
	S	-	-	-	0.61	0.18	-	0.11
	Ba	-	0.16	0.22	-	-	0.03	-
	P	-	-	-	-	0.13	0.12	0.20
	Cr	-	-	-	-	0.03	0.07	0.07
	F	1.06	1.31	1.31	0.86	1.23	1.01	1.08
	Cl	-	0.32	0.04	-	0.04	-	0.03
	OH	2.94	2.37	2.65	3.14	2.73	2.99	2.89
	Total	**19.52**	**19.87**	**19.89**	**18.90**	**19.57**	**19.92**	**19.77**

Dash (-) - indicates values are b.d. limits

4. Chlorite

		Zen 26-GP-09	Zen 29-GP-32	Zen 29-GP-32	Zen 10-GP-116	Zen 26-GP-105	Zen 26-GP-105	Zen 26-GP-105
Wt.%								
	SiO_2	26.78	32.67	32.46	29.84	39.05	33.93	34.65
	TiO_2	-	-	-	-	-	-	-
	Al_2O_3	15.97	14.34	13.92	15.11	16.49	13.62	13.89
	Cr_2O_3	-	-	-	-	-	-	-
	FeO	30.19	21.58	18.96	30.87	25.78	29.19	27.63
	MnO	-	-	-	-	-	-	-
	NiO	-	-	-	-	-	-	-
	ZnO	-	-	-	-	-	-	-
	MgO	14.94	15.47	17.58	12.26	10.79	12.94	13.1
	CaO	0.34	0.68	0.49	0.39	1.16	0.54	0.85
	Na_2O	-	-	-	-	1.30	-	-
	K_2O	0.32	-	-	-	0.31	-	0.15
	SO_3	-	-	-	-	-	-	-
	Total	**88.54**	**84.74**	**83.41**	**88.47**	**94.88**	**90.22**	**90.27**
Structural formulae calculated on the basis of 28 oxygens								
a.p.f.u.								
	Si	5.77	6.90	6.88	6.38	7.41	6.97	7.06
	Ti	-	-	-	-	-	-	-
	Al	4.06	3.57	3.48	3.81	3.69	3.30	3.33
	Cr	-	-	-	-	-	-	-
	Fe^{2+}	5.44	3.81	3.36	5.52	4.09	5.02	4.70
	Mn	-	-	-	-	-	-	-
	Ni	-	-	-	-	-	-	-
	Zn	-	-	-	-	-	-	-
	Mg	4.80	4.87	5.55	3.91	3.05	3.97	3.98
	Ca	0.08	0.15	0.11	0.09	0.24	0.12	0.19
	Na	-	-	-	-	0.48	-	-
	K	0.09	-	-	-	0.08	-	0.04
	S	-	-	-	-	-	-	-
	Total	**20.24**	**19.31**	**19.38**	**19.71**	**19.03**	**19.38**	**19.30**

Dash (-) - indicates values are b.d. limits

		Zen 26-GP-105	**Zen 2-GP-32**	**Zen 2-GP-32**	**Zen 2-GP-32**	**Zen 2-GP-32**	**Zen 2-GP-32**	**Zen 2-GP-32**
Wt.%								
	SiO_2	34.50	38.14	36.38	36.41	33.71	35.00	30.85
	TiO_2	-	-	-	-	-	-	-
	Al_2O_3	12.40	6.61	6.41	6.62	8.20	6.83	10.91
	Cr_2O_3	-	-	-	-	-	-	-
	FeO	27.59	34.56	36.03	36.59	36.19	35.61	40.18
	MnO	-	0.53	0.61	-	-	-	-
	NiO	-	-	-	-	-	-	-
	ZnO	-	-	-	-	-	-	-
	MgO	13.08	2.07	2.24	1.75	2.35	2.34	2.37
	CaO	0.63	3.04	3.02	2.44	2.52	3.04	1.69
	Na_2O	-	-	-	-	-	-	-
	K_2O	0.16	0.36	0.45	0.39	0.77	0.45	0.24
	SO_3	-	-	0.55	0.52	0.86	0.50	0.54
	Total	**88.36**	**85.31**	**85.69**	**84.72**	**84.60**	**83.77**	**86.78**
Structural formulae calculated on the basis of 28 oxygens								
a.p.f.u.								
	Si	7.19	8.62	8.29	8.37	7.81	8.17	7.12
	Ti	-	-	-	-	-	-	-
	Al	3.05	1.76	1.72	1.79	2.24	1.88	2.97
	Cr	-	-	-	-	-	-	-
	Fe^{2+}	4.81	6.53	6.87	7.04	7.01	6.95	7.76
	Mn	-	0.10	0.12	-	-	-	-
	Ni	-	-	-	-	-	-	-
	Zn	-	-	-	-	-	-	-
	Mg	4.07	0.70	0.76	0.60	0.81	0.81	0.82
	Ca	0.14	0.74	0.74	0.60	0.63	0.76	0.42
	Na	-	-	-	-	-	-	-
	K	0.04	0.10	0.13	0.11	0.23	0.13	0.07
	S	-	-	0.09	0.09	0.15	0.09	0.09
	Total	**19.30**	**18.55**	**18.72**	**18.61**	**18.88**	**18.79**	**19.24**

Dash (-) - indicates values are b.d. limits

		Zen 2-GP-32	**Zen 26-GP-105**	**Zen 26-GP-105**	**Zen 26-GP-105**	**Zen 26-GP-105**	**Zen 26-GP-105**
Wt.%							
	SiO_2	30.50	53.71	46.48	46.50	46.02	48.89
	TiO_2	-	-	-	-	-	-
	Al_2O_3	7.76	6.89	5.81	5.59	7.39	7.91
	Cr_2O_3	-	-	-	-	-	-
	FeO	33.83	13.83	14.33	14.77	14.58	14.73
	MnO	-	-	-	-	-	-
	NiO	-	-	-	-	-	-
	ZnO	-	-	-	-	-	-
	MgO	2.07	11.87	10.13	9.53	12.65	13.63
	CaO	2.63	1.48	1.37	6.09	2.06	2.19
	Na_2O	-	-	-			
	K_2O	0.60	2.27	3.01	3.32	1.61	1.80
	SO_3	0.62	-	-	-	-	-
	Total	**78.01**	**90.05**	**81.13**	**85.80**	**84.31**	**89.15**
Structural formulae calculated on the basis of 28 oxygens							
a.p.f.u.							
	Si	7.72	9.90	9.73	9.43	9.24	9.26
	Ti	-	-	-	-	-	-
	Al	2.31	1.50	1.43	1.34	1.75	1.76
	Cr	-	-		-	-	-
	Fe^{2+}	7.16	2.13	2.51	2.50	2.45	2.33
	Mn	-	-	-	-	-	-
	Ni	-	-	-	-	-	-
	Zn	-	-	-	-	-	-
	Mg	0.78	3.26	3.16	2.88	3.79	3.85
	Ca	0.71	0.29	0.31	1.32	0.44	0.43
	Na	-	-	-	-	-	-
	K	0.19	0.53	0.80	0.86	0.41	0.43
	S	0.12	-	-	-	-	-
	Total	**18.99**	**17.62**	**17.95**	**18.33**	**18.09**	**18.08**

Dash (-) - indicates values are b.d. limits

5. Amphiboles

		Zen 2-GP-32	**Zen 2-GP-32**	**Zen 2-GP-21**	**Zen 2-GP-21**	**Zen 2-GP-21**	**Zen 2-GP-21**	**Zen 2-GP-21**
Wt.%								
	SiO_2	51.62	55.75	48.92	50.05	49.97	50.00	50.26
	TiO_2	-	-	0.87	0.56	0.54	0.65	0.69
	Al_2O_3	2.28	0.81	3.65	3.22	3.2	3.07	4.10
	FeO	19.24	15.49	17.92	17.59	17.54	17.64	15.23
	MnO	0.65	0.52	0.61	0.85	0.68	0.70	0.78
	MgO	12.24	14.52	12.35	12.69	12.85	12.72	14.07
	CaO	11.79	12.68	11.84	11.12	11.83	11.28	11.9
	Na_2O	0.86	-	1.08	1.49	1.11	1.34	1.45
	K_2O	0.40	-	0.65	0.58	0.62	0.61	0.33
	F	-	-	-	-	-	-	-
	Cl	-	-	-	0.15	-	-	-
		99.08	**99.77**	**97.89**	**98.3**	**98.34**	**98.01**	**98.81**
	-O≡F	-	-	-	-	-	-	-
	-O≡Cl	-	-	-	0.03	-	-	-
	Total	**99.08**	**99.77**	**97.89**	**98.27**	**98.34**	**98.01**	**98.81**
Structural formulae calculated on the basis of 23 oxygens								
a.p.f.u.								
	Si	7.62	7.94	7.32	7.43	7.42	7.44	7.34
	Ti	-	-	0.10	0.06	0.06	0.07	0.08
	Al	0.40	0.14	0.64	0.56	0.56	0.54	0.71
	Fe	2.37	1.84	2.24	2.18	2.18	2.20	1.86
	Mn	0.08	0.06	0.08	0.11	0.09	0.09	0.10
	Mg	2.69	3.08	2.76	2.81	2.84	2.82	3.06
	Ca	1.86	1.93	1.90	1.77	1.88	1.80	1.86
	Na	0.12	-	0.16	0.21	0.16	0.19	0.21
	K	0.04	-	0.06	0.05	0.06	0.06	0.03
	F	-	-	-	-	-	-	-
	Cl	-	-	-	0.04	-	-	-
	Total	**15.19**	**15.00**	**15.26**	**15.24**	**15.24**	**15.21**	**15.23**

Dash (-) - indicates values are b.d. limits

		Zen 2-GP-21	Zen 27-GP-63	Zen 27-GP-63	Zen 27-GP-63	Zen 27-GP-63	Zen 27-GP-63	Zen 27-GP-63
Wt.%								
	SiO_2	50.92	47.8	47.56	48.85	48.92	54.14	50.94
	TiO_2	0.50	-	-	0.58	-	-	-
	Al_2O_3	2.56	3.98	3.92	3.96	4.05	0.55	2.81
	FeO	17.18	18.24	18.47	17.87	19.78	21.64	21.48
	MnO	0.67	0.51	0.62	0.48	0.57	0.85	0.99
	MgO	13.04	10.97	10.78	12.00	11.79	10.6	9.82
	CaO	11.93	11.71	11.98	12.48	12.47	12.69	13.14
	Na_2O	1.08	1.55	1.11	1.37	1.28	-	0.71
	K_2O	0.48	0.77	0.84	0.97	0.90	-	-
	F	-	-	-	-	-	-	-
	Cl	-	0.15	0.17	-	0.15	-	-
		98.36	**95.68**	**95.45**	**98.56**	**99.91**	**100.47**	**99.89**
	-O≡F	-	-	-	-	-	-	-
	-O≡Cl	-	0.03	0.04	-	0.03	-	-
	Total	**98.36**	**95.65**	**95.41**	**98.56**	**99.88**	**100.47**	**99.89**
Structural formulae calculated on the basis of 23 oxygens								
a.p.f.u.								
	Si	7.53	7.36	7.36	7.29	7.26	7.91	7.56
	Ti	0.06	-	-	0.07	-	-	-
	Al	0.45	0.72	0.71	0.70	0.71	0.09	0.49
	Fe	2.12	2.35	2.39	2.23	2.46	2.64	2.66
	Mn	0.08	0.07	0.08	0.06	0.07	0.11	0.12
	Mg	2.87	2.52	2.49	2.67	2.61	2.31	2.17
	Ca	1.89	1.93	1.99	2.00	1.98	1.99	2.09
	Na	0.15	0.23	0.17	0.20	0.18	-	0.10
	K	0.05	0.08	0.08	0.09	0.09	-	-
	F	-	-	-	-	-	-	-
	Cl	-	0.04	0.04	-	0.04	-	-
	Total	**15.20**	**15.30**	**15.31**	**15.30**	**15.40**	**15.04**	**15.20**

Dash (-) - indicates values are b.d. limits

		Zen 27-GP-63	Zen 27-GP-63	Zen 27-GP-63	Zen 27-GP-63	Zen 27-GP-63	Zen 27-GP-63	Zen 27-GP-63
Wt.%								
	SiO_2	51.77	52.42	53.20	53.53	51.85	53.38	47.48
	TiO_2	-	-	-	-	-	-	0.68
	Al_2O_3	1.30	0.81	0.72	0.54	2.73	2.05	4.14
	FeO	22.39	21.38	21.26	20.16	16.92	16.83	18.84
	MnO	0.88	1.00	0.80	0.86	0.49	0.88	0.69
	MgO	10.01	11.14	11.13	11.01	13.17	12.99	11.69
	CaO	13.13	12.54	12.88	13.66	12.5	12.49	12.28
	Na_2O	0.40	-	-	-	1.15	1.05	1.48
	K_2O	-	0.30	-	0.34	0.67	0.61	0.94
	F	-	-	-	-	-	-	-
	Cl	-	-	-	-	-	-	-
		99.88	**99.59**	**99.99**	**100.10**	**99.48**	**100.28**	**98.22**
	-O≡F	-	-	-	-	-	-	-
	-O≡Cl	-	-	-	-	-	-	-
	Total	**99.88**	**99.59**	**99.99**	**100.10**	**99.48**	**100.28**	**98.22**
Structural formulae calculated on the basis of 23 oxygens								
a.p.f.u.								
	Si	7.70	7.77	7.82	7.85	7.56	7.70	7.17
	Ti	-	-	-	-	-	-	0.08
	Al	0.23	0.14	0.12	0.09	0.47	0.35	0.74
	Fe	2.78	2.65	2.61	2.47	2.06	2.03	2.38
	Mn	0.11	0.13	0.10	0.11	0.06	0.11	0.09
	Mg	2.22	2.46	2.44	2.41	2.86	2.80	2.63
	Ca	2.09	1.99	2.03	2.15	1.95	1.93	1.99
	Na	0.06	-	-	-	0.16	0.15	0.22
	K	-	0.03	-	0.03	0.06	0.06	0.09
	F	-	-	-	-	-	-	-
	Cl	-	-	-	-	-	-	-
	Total	**15.19**	**15.16**	**15.12**	**15.10**	**15.20**	**15.12**	**15.38**

Dash (-) - indicates values are b.d. limits

		Zen 26-GP-105	Zen 26-GP-105	Zen 26-GP-105	Zen 26-GP-105	Zen 26-GP-105	Zen 26-GP-105	Zen 26-GP-105
Wt.%								
	SiO_2	57.36	57.42	59.01	58.39	58.44	57.97	56.66
	TiO_2	-	-	-	-	-	-	-
	Al_2O_3	-	-	0.91	-	0.34	-	0.65
	FeO	8.8	5.98	10.6	5.82	5.31	7.69	11.72
	MnO	0.32	0.27	-	-	-	0.44	-
	MgO	19.71	21.26	22.31	21.83	21.86	20.45	17.06
	CaO	13.04	13.30	7.28	13.37	13.63	13.32	12.95
	Na_2O	-	-	-	-	-	-	-
	K_2O	-	-	-	-	-	-	-
	F	-	-	-	-	-	-	-
	Cl	-	-	-	-	-	-	-
		99.23	**98.23**	**100.11**	**99.41**	**99.58**	**99.87**	**99.04**
	-O≡F	-	-	-	-	-	-	-
	-O≡Cl	-	-	-	-	-	-	-
	Total	**99.23**	**98.23**	**100.11**	**99.41**	**99.58**	**99.87**	**99.04**
Structural formulae calculated on the basis of 23 oxygens								
a.p.f.u.								
	Si	7.96	7.96	8.00	7.97	7.95	7.96	7.97
	Ti	-	-	-	-	-	-	-
	Al	-	-	0.15	-	0.05	-	0.11
	Fe	1.02	0.69	1.20	0.66	0.60	0.88	1.38
	Mn	0.04	0.03	-	-	-	0.05	-
	Mg	4.08	4.39	4.51	4.44	4.43	4.19	3.58
	Ca	1.94	1.97	1.06	1.95	1.99	1.96	1.95
	Na	-	-	-	-	-	-	-
	K	-	-	-	-	-	-	-
	F	-	-	-	-	-	-	-
	Cl	-	-	-	-	-	-	-
	Total	**15.04**	**15.04**	**14.92**	**15.03**	**15.02**	**15.04**	**14.98**
Dash (-) - indicates values are b.d. limits								

		Zen 26-GP-105
Wt.%		
	SiO_2	59.37
	TiO_2	-
	Al_2O_3	-
	FeO	4.78
	MnO	0.48
	MgO	22.99
	CaO	12.05
	Na_2O	-
	K_2O	-
	F	-
	Cl	-
		99.67
	-O≡F	-
	-O≡Cl	-
	Total	**99.67**
Structural formulae calculated on the basis of 23 oxygens		
a.p.f.u.		
	Si	8.02
	Ti	-
	Al	-
	Fe	0.54
	Mn	0.05
	Mg	4.63
	Ca	1.74
	Na	-
	K	-
	F	-
	Cl	-
	Total	**14.98**
Dash (-) - indicates values are b.d. limits		

6. Pyroxenes

		Zen 27-GP-63	Zen 27-GP-63	Zen 27-GP-63	Zen 27-GP-63	Zen 27-GP-63	Zen 27-GP-63	Zen 27-GP-63
Wt.%								
	SiO_2	50.57	51.02	51.39	50.21	50.06	49.99	50.26
	TiO_2	-	-	-	-	-	-	-
	Al_2O_3	-	0.45	-	-	0.53	-	-
	FeO	15.68	15.61	14.94	16.95	15.90	16.29	17.85
	MnO	0.82	0.70	0.74	0.87	0.84	0.85	0.73
	MgO	8.91	9.05	9.20	8.97	9.15	9.32	9.04
	CaO	22.26	22.31	22.78	22.00	23.27	22.74	21.40
	Li_2O	-	-	-	-	-	-	-
	Na_2O	0.39	0.59	0.49	0.64	0.39	0.55	0.79
	K_2O	-	-	-	-	-	-	-
	Cl	-	-	-	-	-	-	-
		98.63	**99.73**	**99.54**	**99.64**	**100.14**	**99.74**	**100.07**
	-O≡Cl	-	-	-	-	-	-	-
	Total	**98.63**	**99.73**	**99.54**	**99.64**	**100.14**	**99.74**	**100.07**
Structural formulae calculated on the basis of 6 oxygens								
a.p.f.u.								
	Si	1.99	1.98	2.00	1.97	1.95	1.96	1.97
	Ti	-	-	-	-	-	-	-
	Al	-	0.02	-	-	0.02	-	-
	Fe^{2+}	0.52	0.51	0.49	0.56	0.52	0.53	0.58
	Mn	0.03	0.02	0.02	0.03	0.03	0.03	0.02
	Mg	0.52	0.52	0.53	0.52	0.53	0.54	0.53
	Ca	0.94	0.93	0.95	0.92	0.97	0.95	0.90
	Li	-	-	-	-	-	-	-
	Na	0.03	0.04	0.04	0.05	0.03	0.04	0.06
	K	-	-	-	-	-	-	-
	Cl	-	-	-	-	-	-	-
	Total	**4.02**	**4.03**	**4.02**	**4.05**	**4.05**	**4.06**	**4.06**
Dash (-) - indicates values are b.d. limits								

		Zen 27-GP-63	**Zen 27-GP-63**	**Zen 27-GP-63**	**Zen 27-GP-63**	**Zen 27-GP-63**	**Zen 27-GP-63**	**Zen 27-GP-63**
Wt.%								
	SiO_2	51.02	50.61	49.95	50.98	50.46	50.89	51.27
	TiO_2	-	-	-	-	-	-	-
	Al_2O_3	0.41	-	-	-	-	-	-
	FeO	15.74	16.39	16.26	16.70	16.83	16.12	15.73
	MnO	0.66	0.87	0.94	0.82	0.81	0.68	0.65
	MgO	9.48	9.37	9.33	9.16	9.18	9.59	10.43
	CaO	23.03	22.79	22.43	21.84	22.87	23.34	22.69
	Li_2O	-	-	-	-	-	-	-
	Na_2O	0.46	0.59	0.60	0.83	0.64	0.33	-
	K_2O	-	-	-	-	-	-	-
	Cl	-	-	-	-	-	-	-
		100.80	**100.62**	**99.51**	**100.33**	**100.79**	**100.95**	**100.77**
	-O≡Cl	-	-	-	-	-	-	-
	Total	**100.80**	**100.62**	**99.51**	**100.33**	**100.79**	**100.95**	**100.77**
Structural formulae calculated on the basis of 6 oxygens								
a.p.f.u.								
	Si	1.97	1.96	1.96	1.98	1.96	1.96	1.97
	Ti	-	-	-	-	-	-	-
	Al	0.02	-	-	-	-	-	-
	Fe^{2+}	0.51	0.53	0.53	0.54	0.55	0.52	0.51
	Mn	0.02	0.03	0.03	0.03	0.03	0.02	0.02
	Mg	0.54	0.54	0.55	0.53	0.53	0.55	0.60
	Ca	0.95	0.95	0.94	0.91	0.95	0.97	0.93
	Li	-	-	-	-	-	-	-
	Na	0.03	0.04	0.05	0.06	0.05	0.02	-
	K	-	-	-	-	-	-	-
	Cl	-	-	-	-	-	-	-
	Total	**4.04**	**4.06**	**4.06**	**4.05**	**4.06**	**4.05**	**4.03**
Dash (-) - indicates values are b.d. limits								

		Zen 27-GP-63	Zen 27-GP-63	Zen 26-GP-105
Wt.%				
	SiO_2	50.77	51.46	52.06
	TiO_2	-	-	-
	Al_2O_3	-	0.33	-
	FeO	15.58	15.61	8.01
	MnO	0.78	0.73	0.69
	MgO	9.95	10.12	14.39
	CaO	23.57	22.92	23.70
	Li_2O	-	-	-
	Na_2O	-	0.45	0.29
	K_2O	-	-	-
	Cl	-	-	-
		100.65	**101.62**	**99.14**
	-O≡Cl	-	-	-
	Total	**100.65**	**101.62**	**99.14**
Structural formulae calculated on the basis of 6 oxygens				
a.p.f.u.				
	Si	1.96	1.96	1.97
	Ti	-	-	-
	Al	-	0.01	-
	Fe^{2+}	0.50	0.50	0.25
	Mn	0.03	0.02	0.02
	Mg	0.57	0.58	0.81
	Ca	0.98	0.94	0.96
	Li	-	-	-
	Na	-	0.03	0.02
	K	-	-	-
	Cl	-	-	-
	Total	**4.04**	**4.05**	**4.04**

Dash (-) - indicates values are b.d. limits

7. Fe-Ti Oxides

Ilmenite

	Zen 2-GP-21	Zen 2-GP-21	Zen 2-GP-21	Zen 2-GP-21	Zen 26-GP-105	Zen 26-GP-105	Zen 26-GP-105
Wt.%							
TiO_2	51.47	52.03	51.80	50.47	51.12	50.88	52.28
SiO_2	-	-	0.48	0.61	1.36	0.39	-
Fe_2O_3	1.53	1.63	1.44	2.27	0.97	2.48	1.38
Cr_2O_3	-	-	-	-	-	-	-
Al_2O_3	-	-	-	0.39	0.36	-	-
V_2O_3	-	-	-	-	-	-	-
FeO	43.79	44.40	41.46	42.57	41.52	42.96	43.11
MnO	2.49	2.01	5.64	3.02	3.49	3.25	3.87
MgO	-	-	-	-	-	-	-
CaO	-	0.29	-	-	2.00	-	-
K_2O	-	-	-	0.17	-	-	-
Total	**99.28**	**100.36**	**100.82**	**99.50**	**100.82**	**99.96**	**100.64**
Structural formulae calculated on the basis of 3 oxygens							
a.p.f.u.							
Ti	0.99	0.99	0.98	0.97	0.95	0.97	0.99
Si	-	-	0.01	0.02	0.03	0.01	-
Fe^{3+}	0.03	0.03	0.03	0.04	0.02	0.05	0.03
Cr	-	-	-	-	-	-	-
Al	-	-	-	0.01	0.01	-	-
V	-	-	-	-	-	-	-
Fe^{2+}	0.94	0.94	0.87	0.91	0.86	0.91	0.91
Mg	-	-	-	-	-	-	-
Mn	0.05	0.04	0.12	0.07	0.07	0.07	0.08
Ca	-	0.01	-	-	0.05	-	-
K	-	-	-	0.01	-	-	-
Total	**2.01**	**2.01**	**2.01**	**2.02**	**2.00**	**2.01**	**2.01**

Dash (-) - indicates values are b.d. limits

		Zen 26-GP-105	Zen 26-GP-105
Wt.%			
	TiO_2	53.64	51.75
	SiO_2	-	-
	Fe_2O_3	2.19	2.31
	Cr_2O_3	-	-
	Al_2O_3	-	-
	V_2O_3	-	-
	FeO	42.39	44.25
	MnO	5.80	2.29
	MgO	-	-
	CaO	-	-
	K_2O	-	-
	Total	**104.02**	**100.60**
Structural formulae calculated on the basis of 3 oxygens			
a.p.f.u.			
	Ti	0.99	0.99
	Si	-	-
	Fe^{3+}	0.04	0.04
	Cr	-	-
	Al	-	-
	V	-	-
	Fe^{2+}	0.87	0.94
	Mg	-	-
	Mn	0.12	0.05
	Ca	-	-
	K	-	-
	Total	**2.02**	**2.02**

Dash (-) - indicates values are b.d. limits

Magnetite

		Zen 29-GP-32	**Zen 29-GP-32**	**Zen 26-GP-105**	**Zen 26-GP-105**	**Zen 26-GP-105**
Wt.%						
	SiO_2	1.02	0.58	5.37	16.61	6.27
	TiO_2	-	-	-	-	-
	Al_2O_3	0.52	3.61	1.45	0.78	1.41
	Fe_2O_3	41.73	9.62	45.90	27.29	44.46
	FeO	40.46	60.60	40.88	48.70	41.43
	MnO	-	-	-	-	-
	MgO	-	-	2.79	3.32	2.94
	CaO	0.19	0.26	-	0.43	-
	K_2O	-	-	1.06	0.40	0.89
	SO_3	0.62	11.62	-	-	-
	Total	**84.54**	**86.29**	**97.45**	**97.52**	**97.40**
Structural formulae calculated on the basis of 4 oxygens						
a.p.f.u.						
	Si	0.06	0.03	0.25	0.65	0.28
	Ti	-	-	-	-	-
	Al	0.04	0.19	0.08	0.04	0.08
	Fe^{3+}	1.80	0.32	1.59	0.81	1.52
	Fe^{2+}	1.94	2.21	1.57	1.60	1.57
	Mn	-	-	-	-	-
	Mg	-	-	0.19	0.20	0.20
	Ca	0.01	0.01	-	0.02	-
	K	-	-	0.06	0.02	0.05
	S	0.03	0.38	-	-	-
	Total	**3.87**	**3.12**	**3.74**	**3.34**	**3.70**

Dash (-) - indicates values are b.d. limits

8. Accessory Minerals

Chromite

		Zen 26-GP-105	Zen 26-GP-105
Wt.%			
	SiO_2	-	0.43
	TiO_2	1.04	0.68
	Al_2O_3	7.74	5.22
	Cr_2O_3	42.39	52.02
	FeO	37.32	34.60
	MnO	2.27	-
	ZnO	5.03	4.51
	CaO	0.27	0.27
	K_2O	0.18	0.21
	V_2O_5	3.80	2.41
	SO_3	0.71	-
	Total	**100.75**	**100.35**
Structural formulae calculated on the basis of 4 oxygens			
a.p.f.u.			
	Si	-	1.05
	Ti	0.03	0.01
	Al	0.33	0.11
	Cr	1.21	0.72
	Fe	1.13	0.51
	Mn	0.07	-
	Zn	0.13	0.06
	Ca	0.01	0.01
	K	0.01	-
	V	0.09	0.03
	S	0.02	-
	Total	**3.03**	**2.49**

Dash (-) - indicates values are b.d. limits

Apatite

		Zen 2-GP-32	**Zen 2-GP-32**	**Zen 2-GP-32**	**Zen 2-GP-32**	**Zen 2-GP-32**	**Zen 2-GP-21**	**Zen 2-GP-21**
Wt.%								
	SiO_2	-	0.52	-	-	-	-	-
	FeO	0.75	-	-	-	-	-	-
	MnO	-	-	-	-	-	-	-
	MgO	-	-	-	-	-	-	-
	CaO	55.86	56.48	57.31	57.45	57.31	56.93	56.50
	SrO	-	-	-	-	-	-	-
	Na_2O	-	-	-	-	-	-	-
	K_2O	-	-	-	-	-	-	-
	P_2O_5	41.55	42.88	42.40	42.45	42.67	42.83	42.73
	F	4.59	4.13	4.60	4.24	5.03	4.07	4.28
	Cl	-	0.15	-	-	-	-	-
		98.16	**99.73**	**99.71**	**99.90**	**99.98**	**99.76**	**99.23**
	-O≡F	1.93	1.74	1.94	1.79	2.12	1.71	1.80
	-O≡Cl	-	0.03	-	-	-	-	-
	Total	**96.23**	**97.96**	**97.77**	**98.11**	**97.86**	**98.05**	**97.43**
Structural formulae calculated on the basis of 26 oxygens								
a.p.f.u.								
	Si	-	0.09	-	-	-	-	-
	Fe	0.10	-	-	-	-	-	-
	Mn	-	-	-	-	-	-	-
	Mg	-	-	-	-	-	-	-
	Ca	10.00	9.90	10.08	10.12	10.00	10.03	9.98
	Sr	-	-	-	-	-	-	-
	Na	-	-	-	-	-	-	-
	K	-	-	-	-	-	-	-
	P	5.88	5.94	5.89	5.91	5.88	5.96	5.96
	F	2.42	2.14	2.39	2.20	2.59	2.12	2.23
	Cl	-	0.04	-	-	-	-	-
	Total	**18.40**	**18.10**	**18.36**	**18.24**	**18.47**	**18.11**	**18.17**

Dash (-) - indicates values are b.d. limits

	Zen 26-GP-09	**Zen 26-GP-09**	**Zen 27-GP-63**	**Zen 27-GP-63**	**Zen 27-GP-63**	**Zen 27-GP-63**	**Zen 10-GP-116**
Wt.%							
SiO_2	-	-	-	-	0.76	-	-
FeO	-	-	-	-	-	-	-
MnO	-	-	-	-	-	-	-
MgO	-	-	-	-	-	-	-
CaO	57.08	57.45	55.45	57.03	57.08	57.89	53.02
SrO	-	-	-	-	-	-	-
Na_2O	-	-	-	-	-	-	0.47
K_2O	-	-	-	-	-	-	-
P_2O_5	34.56	42.55	41.26	42.27	43.06	44.00	40.39
F	8.92	-	3.89	4.68	3.82	4.09	3.89
Cl	-	-	-	-	-	-	-
	91.64	**100.00**	**96.71**	**99.30**	**100.90**	**101.89**	**93.88**
-O≡F	3.76	-	1.64	1.97	1.61	1.72	1.64
-O≡Cl	-	-	-	-	-	-	-
Total	**87.88**	**100.00**	**95.07**	**97.33**	**99.29**	**100.17**	**92.24**
Structural formulae calculated on the basis of 26 oxygens							
a.p.f.u.							
Si	-	-	-	-	0.12	-	-
Fe	-	-	-	-	-	-	-
Mn	-	-	-	-	-	-	-
Mg	-	-	-	-	-	-	-
Ca	10.71	10.56	10.10	10.06	9.95	9.98	9.92
Sr	-	-	-	-	-	-	-
Na	-	-	-	-	-	-	0.16
K	-	-	-	-	-	-	-
P	5.13	6.18	5.94	5.89	5.93	5.99	5.97
F	4.94	-	2.09	2.44	1.96	2.08	2.15
Cl	-	-	-	-	-	-	-
Total	**20.78**	**16.73**	**18.14**	**18.38**	**17.96**	**18.05**	**18.20**

Dash (-) - indicates values are b.d. limits

		Zen 26-GP-105	Zen 26-GP-105	Zen 26-GP-105	Zen 26-GP-105	Zen 26-GP-105	Zen 26-GP-105	Zen 26-GP-105
Wt.%								
	SiO_2	0.67	-	-	1.49	1.08	-	1.12
	FeO	0.47	-	-	0.92	1.11	0.71	0.44
	MnO	-	-	-	-	-	-	-
	MgO	-	-	-	0.36	-	-	-
	CaO	57.19	57.40	58.10	56.40	56.62	57.25	57.49
	SrO	-	-	-	-	-	-	-
	Na_2O	-	-	-	-	-	-	-
	K_2O	-	-	-	-	-	-	-
	P_2O_5	42.66	43.06	42.82	40.89	42.44	42.28	41.65
	F	-	-	3.35	3.77	4.06	3.84	4.03
	Cl	-	-	-	-	0.16	-	-
		100.99	**100.46**	**100.92**	**100.06**	**101.09**	**100.24**	**100.70**
	-O≡F	-	-	1.41	1.59	1.71	1.62	1.70
	-O≡Cl	-	-	-	-	0.04	-	-
	Total	**100.99**	**100.46**	**99.51**	**98.47**	**99.34**	**98.62**	**99.00**
Structural formulae calculated on the basis of 26 oxygens								
a.p.f.u.								
	Si	0.11	-	-	0.25	0.18	-	0.18
	Fe	0.07	-	-	0.13	0.15	0.10	0.06
	Mn	-	-	-	-	-	-	-
	Mg	-	-	-	0.04	-	-	-
	Ca	10.39	10.48	10.23	10.01	9.85	10.13	10.09
	Sr	-	-	-	-	-	-	-
	Na	-	-	-	-	-	-	-
	K	-	-	-	-	-	-	-
	P	6.13	6.21	5.96	5.74	5.83	5.91	5.78
	F	-	-	1.74	1.98	2.08	2.00	2.09
	Cl	-	-	-	-	0.04	-	-
	Total	**16.70**	**16.69**	**17.93**	**18.14**	**18.14**	**18.14**	**18.20**

Dash (-) - indicates values are b.d. limits

		Zen 26-GP-105	Zen 26-GP-105	Zen 26-GP-105
Wt.%				
	SiO_2	-	0.66	-
	FeO	-	0.61	0.43
	MnO	-	-	-
	MgO	-	-	-
	CaO	58.01	57.98	57.58
	SrO	-	-	-
	Na_2O	-	-	-
	K_2O	-	-	-
	P_2O_5	42.31	42.63	41.07
	F	4.46	5.24	4.53
	Cl	-	-	-
		100.32	**101.88**	**99.08**
	-O≡F	1.88	2.21	1.91
	-O≡Cl	-	-	-
	Total	**98.44**	**99.67**	**97.17**
Structural formulae calculated on the basis of 26 oxygens				
a.p.f.u.				
	Si	-	0.11	-
	Fe	-	0.08	0.06
	Mn	-	-	-
	Mg	-	-	-
	Ca	10.18	9.94	10.27
	Sr	-	-	-
	Na	-	-	-
	K	-	-	-
	P	5.87	5.78	5.79
	F	2.31	2.65	2.39
	Cl	-	-	-
	Total	**18.36**	**18.56**	**18.51**
Dash (-) - indicates values are b.d. limits				

Titanite

		Zen26-GP-105	Zen 27-GP-63	Zen 27-GP-63	Zen 27-GP-63	Zen 27-GP-63	Zen 27-GP-63
Wt.%							
	SiO_2	30.27	30.56	29.82	29.11	29.47	29.44
	TiO_2	38.21	35.64	37.59	37.58	39.07	40.16
	Al_2O_3	1.43	-	1.30	1.85	0.29	-
	FeO	0.77	1.26	1.34	0.89	1.04	1.08
	MnO	-	-	-	-	-	-
	MgO	-	-	-	-	-	-
	CaO	29.01	28.27	27.50	28.24	28.22	29.21
	Nb_2O_5	-	4.12	1.38	1.46	4.26	-
	Na_2O	-	0.62	-	-	0.53	-
	K_2O	-	-	-	-	-	-
	F	-	-	-	-	-	0.82
	Cl	-	-	-	-	-	-
		99.69	100.47	98.93	99.13	102.88	100.71
	-O≡F	-	-	-	-	-	0.35
	-O≡Cl	-	-	-	-	-	-
	Total	**99.69**	**100.47**	**98.93**	**99.13**	**102.88**	**100.36**
Structural formulae calculated on the basis of 5 oxygens							
a.p.f.u.							
	Si	0.99	1.01	0.99	0.97	0.95	0.96
	Ti	0.94	0.89	0.94	0.94	0.95	0.99
	Al	0.06	-	0.05	0.07	0.01	-
	Fe^{2+}	0.02	0.03	0.04	0.02	0.03	0.03
	Mn	-	-	-	-	-	-
	Mg	-	-	-	-	-	-
	Ca	1.02	1.00	0.98	1.00	0.98	1.02
	Nb	-	0.06	0.02	0.02	0.06	-
	Na	-	0.04	-	-	0.03	-
	K	-	-	-	-	-	-
	F	-	-	-	-	-	0.08
	Cl	-	-	-	-	-	-
	Total	**3.03**	**3.03**	**3.02**	**3.03**	**3.01**	**3.09**

Dash (-) - indicates values are b.d. limits

		Zen2-GP-32	Zen2-GP-32	Zen2-GP-32	Zen10-GP-116	Zen26-GP-105	Zen26-GP-105
Wt.%							
	SiO_2	30.06	29.51	28.35	0.82	31.73	29.39
	TiO_2	36.63	36.71	37.71	90.02	37.14	40.51
	Al_2O_3	1.83	1.75	1.76	-	1.39	1.29
	FeO	0.95	0.91	0.93	2.73	0.99	0.74
	MnO	-	-	-	-	-	-
	MgO	-	-	-	-	-	-
	CaO	27.45	27.43	27.45	0.74	28.55	28.29
	Nb_2O_5	-	-	0.65	10.53	-	-
	Na_2O	-	-	-	-	-	-
	K_2O	-	-	-	-	-	-
	F	-	0.89	-	-	-	-
	Cl	-	-	-	-	-	-
		96.92	**97.20**	**96.85**	**104.84**	**99.80**	**100.22**
	-O≡F	-	0.37	-	-	-	-
	-O≡Cl	-	-	-	-	-	-
	Total	**96.92**	**96.83**	**96.85**	**104.84**	**99.80**	**100.22**
Structural formulae calculated on the basis of 5 oxygens							
a.p.f.u.							
	Si	1.01	0.99	0.96	0.03	1.04	0.96
	Ti	0.93	0.93	0.96	2.23	0.91	1.00
	Al	0.07	0.07	0.07	-	0.05	0.05
	Fe^{2+}	0.03	0.03	0.03	0.08	0.03	0.02
	Mn	-	-	-	-	-	-
	Mg	-	-	-	-	-	-
	Ca	0.99	0.99	1.00	0.03	1.00	0.99
	Nb	-	-	0.01	0.16	-	-
	Na	-	-	-	-	-	-
	K	-	-	-	-	-	-
	F	-	0.09	-	-	-	-
	Cl	-	-	-	-	-	-
	Total	**3.03**	**3.09**	**3.03**	**2.51**	**3.03**	**3.02**

Dash (-) - indicates values are b.d. limits

Zircon

		Zen 2-GP-32	Zen 2-GP-32	Zen 2-GP-32	Zen 2-GP-32	Zen 26-GP-09	Zen 26-GP-105	Zen 26-GP-105
Wt.%								
	SiO_2	33.25	32.74	32.50	29.93	31.20	31.15	31.64
	ZrO_2	65.72	65.51	67.20	67.60	67.07	68.45	65.90
	HfO_2	1.65	0.74	-	-	-	-	1.78
	Al_2O_3	-	-	-	-	-	-	-
	FeO	-	0.50	0.40	-	-	-	0.45
	MgO	-	-	-	-	-	-	-
	CaO	-	-	-	3.18	-	-	0.23
	Na_2O	-	-	-	-	-	-	-
	Total	**100.62**	**99.49**	**100.10**	**100.71**	**98.27**	**99.60**	**100.00**
Structural formulae calculated on the basis of 16 oxygens								
a.p.f.u.								
	Si	4.04	4.02	3.97	3.71	3.91	3.86	3.92
	Zr	3.90	3.93	4.01	4.08	4.09	4.14	3.98
	Hf	0.06	0.03	-	-	-	-	0.06
	Al	-	-	-	-	-	-	-
	Fe	-	0.05	0.04	-	-	-	0.05
	Mg	-	-	-	-	-	-	-
	Ca	-	-	-	0.42	-	-	0.03
	Na	-	-	-	-	-	-	-
	Total	**8.00**	**8.03**	**8.02**	**8.21**	**8.00**	**8.00**	**8.04**
Dash (-) - indicates values are b.d. limits								

		Zen 26-GP-105	**Zen 26-GP-105**	**Zen 26-GP-105**	**Zen 26-GP-105**	**Zen 26-GP-105**	**Zen 26-GP-105**	**Zen 26-GP-105**
Wt.%								
	SiO_2	27.36	28.16	31.72	32.80	31.71	29.25	28.11
	ZrO_2	52.72	54.89	63.09	67.43	67.57	57.12	54.16
	HfO_2	2.79	2.58	1.48	-	1.44	1.24	1.36
	Al_2O_3	-	-	-	-	-	-	-
	FeO	0.95	0.91	0.47	0.34	-	0.48	0.99
	MgO	-	-	-	-	-	-	-
	CaO	1.86	2.11	0.79	-	-	-	1.90
	Na_2O	0.62	-	-	-	-	0.92	0.50
	Total	**86.3**	**88.65**	**97.55**	**100.57**	**100.72**	**89.01**	**87.02**
Structural formulae calculated on the basis of 16 oxygens								
a.p.f.u.								
	Si	3.94	3.94	3.99	3.99	3.90	4.03	3.97
	Zr	3.70	3.75	3.87	4.00	4.05	3.83	3.73
	Hf	0.11	0.10	0.05	-	0.05	0.05	0.05
	Al	-	-	-	-	-	-	-
	Fe	0.11	0.11	0.05	0.03	-	0.06	0.12
	Mg	-	-	-	-	-	-	-
	Ca	0.29	0.32	0.11	-	-	-	0.29
	Na	0.17	-	-	-	-	0.25	0.14
	Total	**8.33**	**8.21**	**8.08**	**8.02**	**8.00**	**8.21**	**8.31**

Dash (-) - indicates values are b.d. limits

		Zen 26-GP-105	**Zen 26-GP-105**	**Zen 26-GP-105**
Wt.%				
	SiO_2	32.62	30.84	31.99
	ZrO_2	65.88	62.87	64.74
	HfO_2	1.52	1.39	1.25
	Al_2O_3	-	-	0.80
	FeO	0.40	0.63	1.21
	MgO	-	-	-
	CaO	-	0.69	0.43
	Na_2O	-	0.71	-
	Total	**100.42**	**97.13**	**100.42**
Structural formulae calculated on the basis of 16 oxygens				
a.p.f.u.				
	Si	3.99	3.92	3.92
	Zr	3.93	3.90	3.86
	Hf	0.05	0.05	0.04
	Al	-	-	0.12
	Fe	0.04	0.07	0.12
	Mg	-	-	-
	Ca	-	0.09	0.06
	Na	-	0.18	-
	Total	**8.02**	**8.21**	**8.12**
Dash (-) - indicates values are b.d. limits				